SISSA

Scuola Internazionale Superiore di Studi Avanzati

The impact of stellar envelopes on the formation of merging compact-object binaries

Supervisor(s):

Mario Spera and ,

Alessandro Bressan

Candidate:

Natalia Nazarova

Astrophysics and Cosmology

2021–2022

Contents

Abstract

The common envelope (CE) phase play a key role in the formation of many astrophysical systems, including merging compact-object binaries. In a tight binary system, the CE phase happens when one star overfills its Roche lobe and initiates a process of dynamically unstable mass transfer. In this scenario, the mass transfer rate increases with time, the secondary star cannot accrete all the incoming material, and the latter surrounds the entire binary. The gas surrounding the binary star is known as CE.

During the CE phase, the binary system rotates at a different rate than the CE. The orbital energy decreases due to the friction between the binary system and the CE. Due to orbital energy loss, the core of the donor and the companion star spiral toward one another within the CE (spiral-in phase). The orbital semi-major axis of binary systems can shrink by orders of magnitude during the spiral-in phase. The lost fraction of orbital energy is transferred to the envelope, which heats up and expands. The CE phase can end with two different outcomes. In the first scenario, the envelope is ejected, leaving the binary system with quite small semi-major axes. In the other scenario, during the spiral-in phase, the two stars merge and become an (evolved) massive star.

Self-consistent hydrodynamical simulations of CE are very complex and computationally expensive. In fast population-synthesis studies, the CE phase is simulated via the (α,λ)-formalism, where α parameterizes the fraction of orbital energy transferred to the envelope, and λ is the envelope's binding-energy parameter.

The time required for a binary system to merge is highly dependent on the α and λ

parameters, so their values have a crucial impact on the interpretation of many astrophysical systems, including merging compact-object binaries. While constraining the α parameter is challenging, we can calculate the λ values and consider λ as a physical quantity instead of a parameter. In this thesis, we present new results on self-consistent calculations of the binding energy parameter for a large set of hydrogen and helium stars, using the up-to-date tracks from the PARSEC stellar evolution code. We demonstrate how the definition of the core-envelope boundary, the nature of the energy sources, metallicity, stellar mass, and evolutionary stage influence the value of λ parameters. We show that the new λ values are up to one order of magnitude lower than those obtained in previous studies and we discuss the associated implication for the formation of merging compact-object binaries. We present fitting formulas for the new binding energy parameters for hydrogen and helium stars obtained in this work, and we evaluate their accuracy with respect to self-consistent data.

The SEVN population-synthesis code is the ground for implementing the new binding-energy prescriptions obtained in this thesis and for an up-to-date astrophysical interpretation of present and forthcoming gravitational-wave sources. Since the SEVN code is based on the star tracks of the PARSEC stellar evolution code, it will be self-consistent to test our new CE prescriptions and study their impact on the evolutionary pathways of binary systems. In this thesis, we focus mainly on introducing several technical improvements in the SEVN code (e.g., adaptive data loading, single and multi-node parallelization), which is the preparatory work that will be crucial to perform efficient simulations of large populations of binary stars and testing the new binding-energy prescriptions.

Chapter 1

Introduction

1.1 Gravitational waves - theoretical background

Albert Einstein predicted gravitational waves (GWs) [1, 2] on the basis of his theory of general relativity (GR) [3, 4]. In Einstein's theory, GWs are wave solutions of linearized weak-field equations. More precisely, GWs were defined as transverse waves of spatial strain that travel at the speed of light, generated by time variations of the mass quadrupole moment of a source. It was an exotic suggestion that many viewed with doubt [5, 6], even Einstein himself was skeptical about the possibility of direct detection of a GW and even about the latter's existence [7, 8].

GWs are caused by an accelerated mass whose motion is neither spherically nor rotationally symmetric. Therefore, they can be produced by the non-spherically symmetric contraction or expansion of a sphere or by a spinning disk or sphere. For instance, binary systems composed of either two black holes (BHs), two Neutron Stars (NSs), or an NS and a BH, are supposed to be loud sources of GWs. Similar to electromagnetic waves, GWs carry away energy and angular momentum from the source, thus the orbit of binary system tends to shrink through GW emission and the two members get closer and closer to each other.

While this thesis focuses on such kind of GW sources, there are many other astrophysical

systems that emit GWs. For example, rapidly rotating NSs [9, 10, 11, 12, 13, 14, 15, 16, 17], core-collapse supernovae (SNe) [18, 19, 20, 21, 22, 23, 24, 25, 26, 27, 28, 29, 30, 31, 32, 33], in the early universe during (p)reheating [34, 35, 36, 37, 38, 39, 40, 41], phase transitions [42, 43, 44, 45, 46, 47], cosmic defects [48, 38, 49, 50], or even the merging of primordial BHs [51, 52, 53, 54, 55, 56].

As a GW passes through an observer, the latter will find spacetime distorted by the effects of strain. Thorne [57] estimated the strain h of a GW as

$$h = \frac{2G}{c^4} \frac{\epsilon E_{\text{kin}}}{r}$$

(1.1)

where r is the distance between the observer and the source, G is the universal gravitational constant and c is the speed of light, ϵE_{kin} is the fraction of kinetic energy associated with the non-spherical motion of the source with $\epsilon \in [0, 1]$.

Because of the nature of gravitational interaction, massive compact objects that move at relativistic speeds can emit GWs with a large strain. If we use the definition of the Schwarzschild radius [58, 59] of a BH with mass M

$$R_{\text{S}} = \frac{2GM}{c^2}$$

(1.2)

and insert it into equation 1.1 and write the kinetic energy [60, 61] as

$$E_{\text{kin}} = \frac{M v^2}{2}$$

(1.3)

we get the following expression for the strain

$$h = \frac{\epsilon}{2} \frac{R_{\text{S}}}{r} \frac{v^2}{c^2}$$

(1.4)

where v^2/c^2 is basically a measurement of the absolute strength of gravity. Strain approaches

3

unity ($h \to 1$) in the proximity of a BH that moves at the speed of light. The further away the GW is from its source, the less spacetime distortion it will cause (the $1/r$ term in formula 1.4 for h). Thus, even waves from extreme systems like merging binary black holes (BBHs) die out to very small strains by the time they reach Earth. Some GWs passing the Earth may have a strain as large as $h \sim 10^{-20}$, but the latter is generally smaller [62].

While emitting GWs, binary systems evolve through two main phases: the inspiral and the ring-down phase. During the inspiral phase, the members of the binary continue to orbit each other and they get closer and closer to each other because of GW emission. In contrast, during the merger phase, the two objects coalesce into a single entity. During the final phase (ring down), the newly born compact object settles down. As we mentioned, during the inspiral phase, the binary star's orbit decays. P_{GW} is the power emitted via GWs or the rate at which orbital energy is carried away by GWS during the in-spiral. P_{GW} can be expressed [63] as

$$P_{\mathrm{GW}} = -\frac{dE}{dt} = -G\,\frac{M_1\,M_2}{2a}\,\frac{da}{dt} \tag{1.5}$$

where M_1 is the mass of the most massive object in the binary and M_2 is the other binary member. The rate at which the semi-major axis a of a binary system decreases because of GW emission can be written as

$$\dot{a} = -\frac{64\,G^3}{5\,c^5}\,\frac{M_1\,M_2\,(M_1 + M_2)}{a\,(1-e)^{7/2}} \tag{1.6}$$

which is a first-order approximation valid for small eccentricity e [64].

The time required for a system to merge is proportional to the total integrated GW luminosity during the coalescence phase:

$$\tau_{GW} = \frac{1}{4}\,\frac{a}{|\dot{a}|} = \frac{5}{256}\,\frac{c^5}{G^3}\,\frac{a^4}{M_1\,M_2\,(M_1 + M_2)}\,(1 - e^2)^{7/2} \tag{1.7}$$

Equation 1.7 demonstrates that the time required for a binary system to reach coalescence
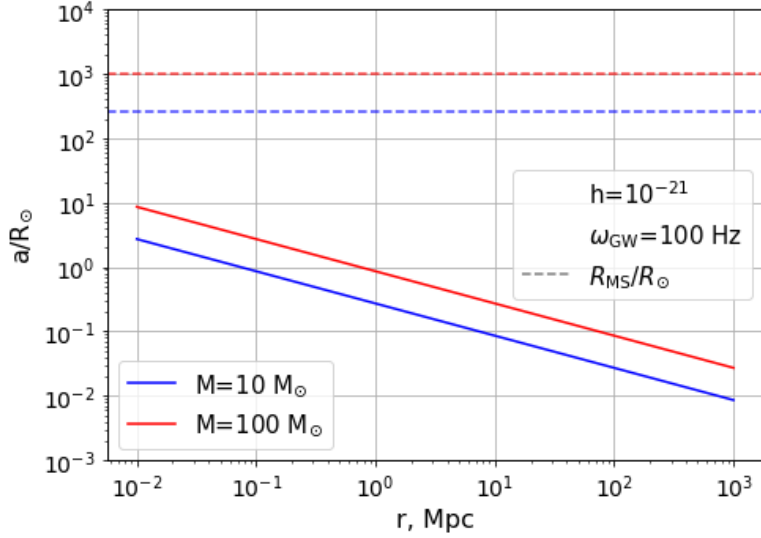
Figure 1.1: Maximum semi-major axis (a) of a binary detectable through GWs by the LIGO-Virgo interferometers at 100 Hz as a function of the cosmic distance of the binary system, with assumed minimum detectable strain $h = 10^{-21}$. Blue (red) solid line: binary members with mass $M_1 = M_2 = 10\, M_\odot$ ($M_1 = M_2 = 100\, M_\odot$). Dashed blue (red) line is the typical $10\, M_\odot$ ($100\, M_\odot$)-star radius at the beginning of the Main Sequence (R_{MS}).

is highly dependent on the semi-major axis, the eccentricity of the orbit, and the masses of the two compact objects:

$$\tau_{GW} \sim a^4 M^{-3} \left(1 - e^2\right)^{7/2} \tag{1.8}$$

By replacing kinetic energy with orbital energy in equation 1.1

$$\epsilon\, E_{\mathrm{kin}} = E_{\mathrm{orb}} = \frac{M_1\, \omega_{\mathrm{orb}}^2\, M_2\, a^2}{M_1 + M_2} \tag{1.9}$$

and replacing the masses with the reduced one

$$\mu = \frac{M_1\, M_2}{M_1 + M_2} \tag{1.10}$$

we can find that strain depends on the orbital frequency of the system as

$$h = \frac{4\, G}{c^4} \frac{\mu\, \omega_{\mathrm{orb}}^2\, a^2}{r} \tag{1.11}$$

5

The LIGO-Virgo interferometers at the onset of the third observational run (O3) had, approximately, strain sensitivity down to $h \sim 10^{-23}$ at 100 Hz frequency [65]. Using formula 1.11, we can estimate the semi-major axes of various binary systems that create a GW that the LIGO-Virgo interferometers will be capable to register and separate from the detectors noise. To do this, we assume that binary systems will create a GW with a strain $h = 10^{-21}$ at a frequency of 100 Hz. Figure 1.1 shows the maximum binary semi-major axis for a LIGO-Virgo detection, in solar radii, as a function of the distance between the binary and observer for equal-mass systems with $M_1 = M_2 = 10 M_\odot$ and $M_1 = M_2 = 100 M_\odot$. From Fig. 1.1 it is apparent that the semi-major axes for all stellar-mass binaries must be, optimistically, less than $\sim 10 R_\odot$ to have the chance for a detection. The figure also show the radius of 10 and 100 $M_\odot$ stars at the beginning of the Main Sequence (R_{MS}). Radius R_{MS} is the minimum radius for a star before the SN explosion because, during the evolution, stars may expand by a few orders of magnitude. At the beginning of the Main Sequence, it is evident that the radius of a star with a mass of 10 $M_\odot$ is approximately 300 $R_\odot$, while a star with a mass of 100 $M_\odot$ has a radius of 10^3 $R_\odot$. The minimum radius of the stars exceeds the values of the maximum semi-major axes needed for a GW detection by more than an order of magnitude. Therefore, only compact objects such as NSs or BHs can be members of a close binary system capable of producing GWs detectable by the LIGO-Virgo interferometers at ~ 100 Hz.

According to formula 1.7, the time required for a binary system to merge depends on the orbit's eccentricity. Suppose that the binary's eccentricity equals zero, i.e., the binary has a circular orbit. In that case, we can estimate the merger time of binaries with different initial masses and the semi-major axis.

Figure 1.2 shows the time required for a binary system to merge via GW emission in units of the Hubble time (t_{H}) for different initial masses and semi-major axes, in the case of circular orbits ($e = 0$). From figure 1.2 it is apparent that, to merge in a Hubble time and produce detectable sources of GWs, compact objects must have quite small initial semi-
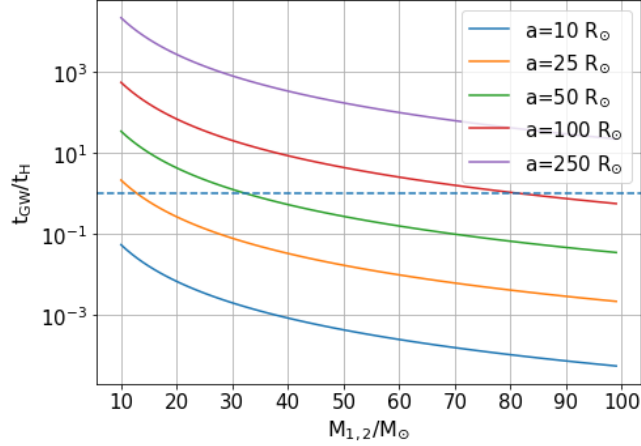
Figure 1.2: The time needed for a binary system to merge via GW emission as a function of a star's masses ($M_1 = M_2$). Time is shown in the units of Hubble time (t_H) for systems with different semi-major axes a. The time is calculated using formula 1.7 for binary systems with circular orbits ($e = 0$).

major axes. For example, two objects with mass 5 $M_\odot$ merge within t_H provided that the semi-major axis is below 10 $R_\odot$. Two objects with masses of 80 $M_\odot$ merge within the Hubble time if $a \lesssim 100 R_\odot$.

1.2 Gravitational waves - Instruments

From the observational point of view, current and next-generation GW interferometers promise to detect many GW sources over a wide range of frequencies, leading to significant breakthroughs in many branches of physics and astronomy. Similar to electromagnetic observations of the Universe, various classes of astrophysical sources emit GWs over a very wide range of possible frequencies, and different instruments are sensitive to different ranges of frequency.

1.2.1 Ground-based detectors

All ground-based interferometers measure the phase and amplitude of GWs using enhanced Michelson interferometry [66, 67, 68] with suspended mirrors. To detect audio-band GWs,

the isolation of the mirrors from local forces and disturbances must meet stringent requirements. Current ground-based interferometers examine the high-frequency portion of the GW spectrum between 10 Hz and 10 kHz. Stellar-mass compact sources like coalescing BBHs and binary neutron stars (BNSs), are loud sources of GWs at this range of frequencies. The two Advanced LIGO detectors [69] have arm lengths of 4 km, while the Advanced Virgo [70] and the Japanese-based KAGRA [71, 72] have arm lengths of 3 km.

A network of globally dispersed interferometers operating as a unified detector is crucial for an in-depth characterization of the detected GW signals. Starting in 2015, the Advanced LIGO and Advanced Virgo detectors have actively searched the GW sky in a highly coordinated campaign involving a series of observing runs. The KAGRA detector will join LIGO and Virgo in O4 (expected for March 2023) to form the LIGO-Virgo-KAGRA network. The LIGO-India [73] interferometer will join later in this decade, significantly enhancing the network's ability to detect and localize GW events [74].

The Einstein Telescope (ET, [75]) and Cosmic Explorer (CE, [76]) are the next generation of ground-based GW detectors slated for the 2030s. They will observe merging BHs and NSs when the Universe was still in its infancy.

LIGO Voyager [77], a major upgrade being considered for the current LIGO observatories in the late 2020s. Voyager could test some of the key technologies required for ET and CE while providing a significant increase in detector sensitivity over the current generation. LIGO Voyager will increase the range of sensitivity by a factor of 4–5 over aLIGO, and the event rate by approximately 100 times, reaching roughly one detection per hour [77].

1.2.2   Space-based interferometers

The Laser Interferometer Space Antenna (LISA) [78, 79] will be launched in the middle of the 2030s and will comprise three spacecraft flying in a triangular formation behind the Earth as our planet orbits the Sun. The separation of free-floating reference surfaces in each satellite is measured precisely using laser interferometry over the 2.5 million km long "arms"

to detect and measure minuscule variations caused by a passing GW. LISA will investigate a significant portion of the GW Universe within 100 μHz to 100 mHz. LISA's all-sky field of view ensures observation in its frequency window of every GW source. Its coherent observation mode allows for resolving and distinguishing overlapping signals and locating them in the sky. LISA can achieve 10^{-21} strain resolution by measuring displacements of the order of fractions of a picometer. Its observations in the quiet space environment will not be disturbed by seismic and gravity-gradient noise.

LISA will be able to detect the first seed BHs formed out to redshifts $z \, sim 20$ or higher [80], as well as intermediate-mass and super-massive coalescing BH [81] systems in the $10^2 - 10^7 M_\odot$ range. Furthermore, LISA could detect stellar-mass BBH systems years before ground-based detectors could [81, 82, 83, 84] and provide exact sky localization of such events for electromagnetic follow-up.

1.2.3 Pulsar timing arrays

Pulsars are rotating NSs that act as cosmic lighthouses, manifesting periodic pulsating radio sources. Since pulsars have rotational stabilities comparable to the most accurate atomic clocks, they are ideal timing sources. The arrival times of pulses can be precisely modeled and predicted to fractions of a microsecond for decades into the future [85]. GWs cause the time of arrival of the pulses to vary, and we can measure such resulting variations.

Thus pulsars can be used as a huge cosmic interferometer. Such pulsar timing arrays (PTAs) [86, 87, 88, 89] investigate the nanohertz 10^{-9} to 10^6 Hz range of the GW spectrum. A PTA measures the arrival times of radio-frequency pulses from an array of millisecond pulsars [90, 91]. The main goal of PTA is to measure the amplitude of background GWs caused by a history of supermassive BH mergers, which are the main source of GW waves at nanohertz frequency.

There are currently three major PTAs: the Parkes PTA [92, 93, 94, 95] in Australia, the European PTA Consortium [96, 97, 98], and the NANOGrav [99, 100, 101, 102] consortium

in North America. These arrays routinely achieve sub-microsecond timing on more than one hundred millisecond pulsars (MSPs), collectively comprising the International Pulsar Timing Array (IPTA) [103].

1.3 Gravitational waves - Astrophysics

On September 14, 2015, the LIGO-Virgo collaboration discovered the first direct evidence of merging compact-object binaries. The two ground-based interferometers of the LIGO [1] measured the effect of a passing GW, identified as GW150914. The signal was associated with the merger of two BHs with masses $M_1 = 36^{+5}_{-4} \, M_\odot$ and $M_2 = 29^{+4}_{-4} \, M_\odot$ [104, 67]. The event had numerous scientific implications and laid the groundwork for a new way to investigate the Universe. GW150914 detection confirmed the existence of BHs binaries that can merge within the Hubble time and revealed stellar BHs with masses $\gtrsim 30 M_\odot$.

GW150914 marked the beginning of a new chapter in astrophysics. It gave an unprecedented boost to the development of new theoretical models to investigate the formation and evolution of compact-object binaries and their progenitor stars, with the new objective of providing an astrophysical interpretation of GW sources.

The first run, O1[2], reported the first 3 detections, all BBH mergers. The second run, O2[3], detected 7 BBH mergers and the first BNS merger [105]. The third run, O3, splitted into O3a[4] and O3b[5] made the first detection of the merger of a NS with a BH. The most recent catalog of GWs that was compiled by the LIGO-Virgo-KAGRA collaboration contains 93 compact-binary coalescences, the vast majority of which are BBH [106, 107, 108, 109]. The catalog already contains numerous merging compact-object binaries that challenge even the most recent theoretical models. For example, GW190814 is an event with very asymmetric masses, a merger that most theoretical models find difficult to explain [110]. Furthermore,

---

[1] At the time of the event, the Virgo detector was offline and undergoing a major upgrade.

[2] O1 run from 12 September 2015 to 19 January 2016

[3] O2 run from 30 November 2016 to 25 August 2017

[4] O3a run from 1 April to 30 September 2019

[5] O3b run from 1 November 2019 until it was suspended on 27 March 2020 due to COVID-19

the lightest member is a compact mystery object with an uncertain nature: it can be the heaviest NS or the lightest BH ever observed, and its mass falls right into the lower mass gap. GW190521 is the event with the heaviest BHs, with at least one of the two falling in the upper mass gap [111, 112]. Its merger product, a BH with mass $148^{+28}_{-16}\,M_\odot$, is the first confirmation of the existence of intermediate-mass BHs. Almost all merger events obtained by the LIGO-Virgo-KAGRA collaboration are consistent with eccentricity equal to zero. The main subject of the debate is GW190521. Some work show that the binary system that produced GW190521 might be consistent with a non-zero eccentricity merger [113, 114, 115].

The scientific insights uncovered by these detections have already revolutionized multiple areas of physics and astrophysics. For example, GW170817 is an event associated with a merger of two NSs. It is the only event observed through GWs and throughout the electromagnetic spectrum, a crucial milestone for multi-messenger astronomy [116].

From a theoretical perspective, astrophysical interpretations of the detected GW sources are highly uncertain, although the number of GWs will increase significantly over the following years due to upcoming next-generation GW detectors (see 1.2.1), 1.2.2), 1.2.3). The processes that can shrink a binary system so that it can merge within Hubble time via GWs (e.g., shrinking to tens of solar radii, see Sec. 1.1 and Fig. 1.2) are highly uncertain, as well as the mass spectrum of stellar BHs.

As the latter aspect, the nature and final mass of a stellar remnant depend crucially on the final properties of stellar cores, which, in turn, depend on the amount of mass a star has lost during its life. Stellar winds have a central role in this concept since they drive mass loss over the lifetime of a star. Stellar winds, especially for massive stars, are uncertain, but their strength depends crucially on metallicity (e.g., [117]).

Figure 1.3 shows the typical impact of different metallicity values on the stars' final mass, prior to the SN explosion. Stars at low Z retain significantly more mass than stars at higher Z. Thus the former can collapse and form significantly heavier BHs. Stars with the same initial mass but different amounts of metals will form a remnant whose mass differs by one
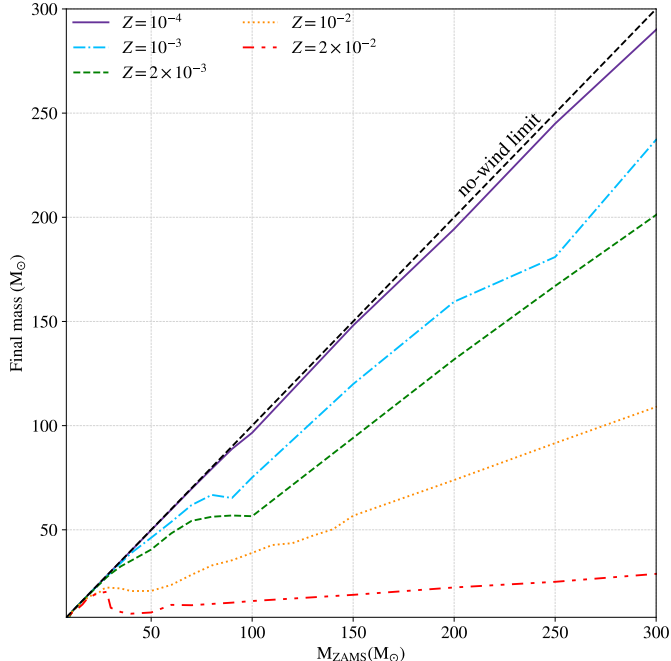
Figure 1.3: Final mass of the stars as a function of their initial mass, for different values of metallicity. The dashed line at 45 degrees corresponds to the no-wind limit (i.e., final mass = initial mass). The plot has been obtained using the SEVN code [118, 119, 120] couples with the PARSEC [121], [122], [123], [124], [125], [126] tracks and it is presented in detail in [117].

order of magnitude.

As a first approximation, the star's initial mass indicates which remnant the star will leave at the end of its life. Very low-mass stars ($M_{ZAMS} \lesssim 0.26\,M_\odot$) do not reach the threshold temperature for helium ignition, and after their long Main Sequence phase, they become helium white dwarfs (WDs) [127]. Stars with $0.26\,M_\odot \lesssim M_{ZAMS} \lesssim 8\,M_\odot$ ignite helium and form a carbon-oxygen (CO) core but do not reach temperatures high enough to ignite CO. After the formation of a CO-core, nuclear reactions in the core stops. Stars with initial masses above $8\,M_\odot$ can reach iron elements, and their life will end with a SN, possibly leaving behind a NS ($8\,M_\odot \lesssim M_{ZAMS} \lesssim 20\,M_\odot$) or a BH ($M_{ZAMS} \gtrsim 20\,M_\odot$). The limits of these mass ranges are also quite uncertain and depend on rotation, chemical composition, convection, dredge-up, wind mass loss, and nuclear reaction rates [128, 129, 130, 131, 132, 133].

The SN process, and so the link between progenitor stars and BHs, is also complex and very uncertain. The SN explosion starts with the collapse of the stellar structure,

which is not sustained anymore by either the core's nuclear reactions or electron degeneracy pressure. The mechanism that triggers the explosion is still a matter of debate, but neutrinos and convection instability are thought to play a crucial role in the explodability of stars. State-of-the-art, three-dimensional hydrodynamical simulations of neutrino-driven SNe predict booming explosions for stars up to $25 - 30\,M_\odot$. However, such sophisticated multi-dimensional simulations are subject to significant uncertainties, and they are computationally intensive (e.g., [134, 135, 136])

Electromagnetic observations and modeling of systems containing BHs have led to speculation about potential "gaps" in the BH mass spectrum. Both gaps may be probed using data from current ground-based GW interferometers and have been the target of a number of studies.

The observations of X-ray binaries combined with Bayesian population modeling [137, 138, 139] suggest a dearth of compact objects with masses between 2.5 $M_\odot$ and 5 $M_\odot$ [140, 141, 142, 143]. The existence and nature of this gap is still to be determined [144]. GW observations can either limit the size of the lower mass gap or disprove its existence [145, 146, 147, 148].

Some 1D SN explosion models predict the existence of such a low-mass gap (e.g. the rapid model presented in Fryer et al. [149]), but 1D models cannot capture the complexity of the explosion mechanism and their results must be taken as provisional.

If the low-mass gap exists, the possible detection of BHs in the gap might be explained by the merger of NS binary stars and not by the collapse of stars into a BH [150].

On the high end of the BH mass spectrum, models of late stellar evolution phases predict the presence of another gap, generally referred to as the upper mass gap. Very massive stars reach a stage where either pair-instability (PISNe) or pulsational pair-instability (PPISNe) occur [151, 152, 153, 120, 154]. Evolved stars with a helium core mass $> 30\,M_\odot$ become unstable because efficient pair production softens their equation of state (EOS). For helium core mass $\sim 30 - 64\,M_\odot$, the star undergoes a sequence of pulsations, losing mass until sta-
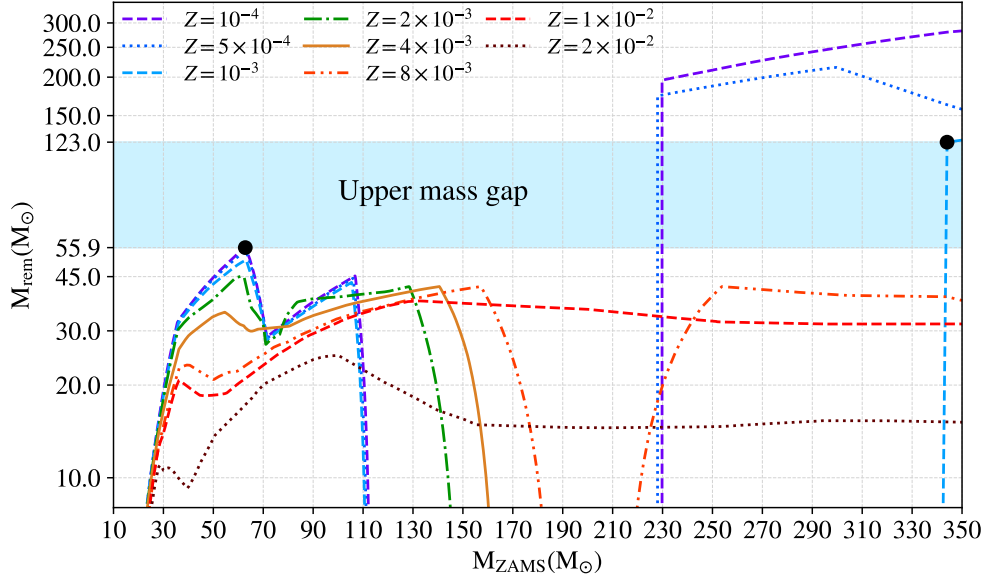
Figure 1.4: Mass of the BH as a function of the initial mass of its progenitor star, for different values of metallicity $Z \in 2[10^{-4}; 2 \times 10^{-2}]$. The shaded cyan area shows the location of the upper mass gap. The two black points set the lower edge ($\sim 55.9 M_\odot$) and the upper edge ($\sim 123 M_\odot$) of the gap. The plot is presented and described in detail in [117].

bility is re-established [155] and it is called PPISN. The enhanced mass loss during PPISNe is expected to significantly affect the final BH mass. The fate of a star with helium core mass $\sim 64 - 135\, M_\odot$ is more dramatic: the entire star is disrupted by a PISNe, leaving no remnant [156, 157, 158]. From the combination of PPISNe and PISNe, it is expected that stars should leave no BH with masses between $\sim 50 - 150\, M_\odot$ because the progenitor star is partially or entirely disrupted by the explosion. Figure 1.4 shows a typical BH mass spectrum expected from state-of-the-art theoretical models when including the effect of PPISNe and PISNe.

While there are many uncertainties about the evolution of isolated stars and their remnants, the number of uncertainties increases even more when we try to investigate the formation and evolution of binaries and how the latter evolution may end up forming merging compact-object systems.

So far, two main formation channels have been proposed to explain the formation of merging compact-object binaries. The first of these is the dynamical scenario. In this

channel, two compact objects approach after a single or a series of gravitational interactions with other stars or compact objects in dense stellar environments, such as globular and young dense star clusters [159, 160, 161, 162, 163], nuclear star clusters [164, 165], or disks of active galactic nuclei [166, 167, 168].Dynamical interactions in triple [169] or quadruple [170] stellar systems can also contribute to the shrinkage of orbital distances and facilitate mergers of compact objects.

The second channel for the formation of merging compact objects is the isolated channel. In the isolated binary scenario, two progenitor stars are bound since their formation. They evolve, become compact objects, and merge without experiencing any external perturbations [171, 172, 173, 174, 175, 176, 177, 178, 179, 180, 181, 182, 183, 184]. The processes of single and binary stellar evolution drive this scenario.

In reality, the two formation pathways might have a strong interplay in star clusters, because single, binary evolution, and stellar dynamics are all active at the same time, and binaries might form in dense environments and merge outside them because of dynamical kicks. Such kind of hybrid scenarios blur the line between the dynamical and the isolated binary channel, and they have already been investigated by various authors [185, 186, 187, 188].

In the context of the isolated channel, chemical homogeneous evolution (CHE) might be one of the key processes that can bring two compact objects very close to each other so they can merge via GWs within the Hubble time. [189, 190, 191]. CHE assumes that the stellar evolution in a very close stellar binary differs from that of a single star due to strong tidal forces. The burning of chemical elements occurs homogeneously, thus the star's outer layers do not expand significantly and they can stay very close to each other without merging during their life. Therefore, the close star systems can survive the phase of stellar expansion and form a merging compact-object binary.

The common envelope (CE) phase is another process that can play a crucial role in the evolution of merging binary systems [192, 193, 194, 195, 196, 197, 198, 199, 200, 201, 202,

203, 204, 205, 206, 207]. In a tight binary system, the CE phase happens when one star overfills its Roche lobe and initiates a process of dynamically unstable mass transfer. In this scenario, the mass transfer rate increases with time, the secondary star cannot accrete all the incoming material, and the latter surrounds the entire binary. The gas surrounding the binary star is known as CE.

During the CE phase, the binary system rotates at a different rate than the CE. The orbital energy decreases due to the friction between the binary system and the CE. More massive and bound envelopes result in stronger friction forces and enhanced loss of orbital energy. Due to orbital energy loss, the core of the donor and the companion star spiral toward one another within the CE (spiral-in phase). The orbital semi-major axis of binary systems can shrink by orders of magnitude during the spiral-in phase.

The lost fraction of orbital energy is transferred to the envelope, which heats up and expands. The CE phase can end with two different outcomes. In the first scenario, the envelope is ejected, leaving the binary system with quite small semi-major axes. In the other scenario, during the spiral-in phase, the two stars merge and become an (evolved) massive star.

If the envelope is completely ejected we have

$$E_{\mathrm{bind}} \leq \Delta E_{\mathrm{orb}} \tag{1.12}$$

otherwise, if the stars merge before the envelope is ejected,

$$E_{\mathrm{bind}} \geq \Delta E_{\mathrm{orb}} \tag{1.13}$$

where E_{bind} is the total binding energy of the envelope and ΔE_{orb} is the change in orbital energy that has been transferred from the orbit to the envelope.

In particular, the amount of energy removed from the orbit and transferred to the envelope (efficiency of the CE evolution) and the envelope's binding energy, which roughly

16

corresponds to the maximum amount of energy that can be removed from the orbit, determine the occurence of the two scenarios. The details of the overall energy balance during the CE phase are highly uncertain from both the observational and theoretical points of view. This aspect hampers us from having detailed constraints on the outcomes of the CE evolution.

1.4 The common envelope phase

CE is thought to play a key role in the formation of many astrophysical systems, including merging compact-object binaries [192, 193, 194, 195, 196, 197, 198, 199, 200, 201, 202, 203, 204, 205, 206, 207], cataclysmic variables ([172], [208], [209], [210]), low mass X-ray binaries ([211], [212], [213], [214]), double white dwarf systems that are supposed to be the progenitors of Type I supernovae ([215], [216], [217], [175], [218], [219], [220]), and tight neutron stars binaries (BNSs) ([221], [222], [223],[224]).

1.4.1 Roche lobe overflow and stability of mass transfer

In a binary stellar system, the Roche limit is the distance from a star above which the latter's external layers are possibly stripped out by the combination of gravity of the companion star and the centrifugal force of the binary motion. Roche discussed the Roche lobe for the first time when he calculated the maximum size of a comet's atmosphere before being disrupted by the Sun [225], [226], [227], [228].

In the formulation of the restricted three-body problem (first star, second star, and unbound material with negligible mass), the first closed equipotential surface is shaped like two tear-drops that surround both stars, with two (Roche) lobes connected by a saddle point at the center (also known as the first Lagrangian point, L_1). Figure 1.5, obtained by Tauris and Heuvel [229], shows the Roche lobes and the first Lagrange point for a binary stellar system.
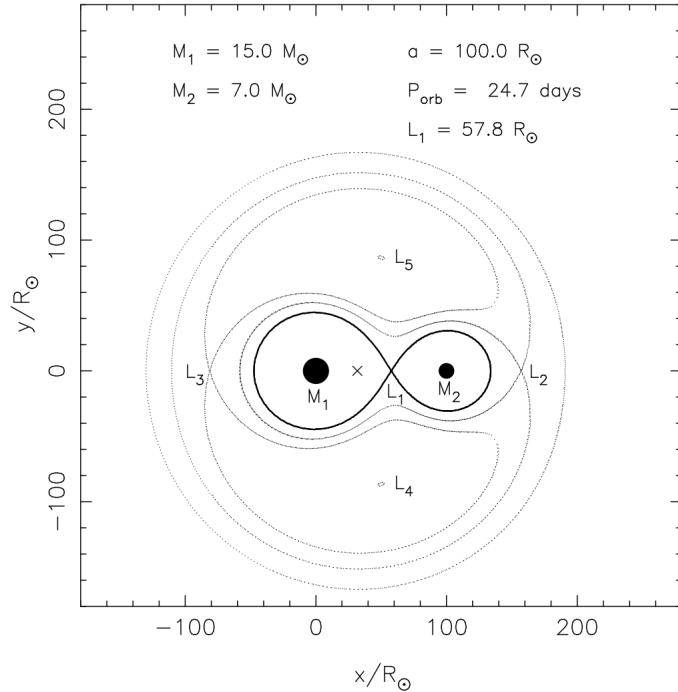
Figure 1.5: A cross-section in the equatorial plane of the critical equipotential surfaces in a binary. The thick curve crossing through L_1 is the Roche-lobe. Tauris and Heuvel [229] obtained and presented this figure in [229].

The study of the geometry of the Roche lobe has been improved and refined over the years. Kopal [230] and Plavec and Kratochvil [231] presented distance tables for several points on the equipotential surfaces that pass through the Lagrange points L_1 and L_2 to approximate the Roche lobe radius. The effective radius of the Roche lobe r_L was determined as the radius of a sphere with a volume equal to the volume of the Roche lobe and approximated in [232]. The latter is known as Pacyński's approximation:

$$ r_L = \max \left[0.46224 \left(\frac{q}{1+q} \right)^{1/3}, \quad 0.38 + 0.2 \log_{10} q \right] \qquad (1.14) $$

where q is the mass ratio M_1/M_2 and the separation of the two stellar centers is unity. Formula 1.14 agrees with the tables of Kopal [230] and Plavec and Kratochvil [231] to within $\sim 2\%$. However, its derivative is discontinuous at $q \approx 0.523$, where the two arguments in the equation 1.14 are equal. This causes the function to be non-smooth when numerically

18

tracking a semi-separated or contact system's evolution near this mass ratio.

Eggleton [233] presented a simple fitting formula for the Roche lobe radius as a function of mass ratio q, which agreed with the two tables above within 1% and it is not singular for any values of q. This fitting formula is widely used and is known as Eggleton's formula:

$$r_{L,1} = \frac{0.49}{0.6 + q^{-2/3} \ln(1 + q^{1/3})} \tag{1.15}$$

$r_{L,1}$ is in units of semi-major axis.

When two stars are isolated, gravitationally bound, and separated by significant distances, such as thousands of solar radii, they are in hydrostatic equilibrium and within their Roche lobes. Because of stellar evolution processes, the more massive star (primary) typically expands first and if the orbital distance in the system is small enough, the star can fill its Roche lobe. When a star completely fills its Roche lobe, it comes into contact with the system's first Lagrange point L_1. At that moment, hydrostatic equilibrium is no longer possible in proximity of L_1. The matter must flow through the nozzle around L_1 and into the Roche lobe of its companion. Roche-lobe overflow (RLO) is the term used to describe this phenomenon.

Below, we will refer to a star that fills its Roche lobe and initiates mass transfer through the internal Lagrange point as a "donor" ($M_1 = M_d$). We use "accretor" to refer to the companion, which can potentially accrete part of the incoming material ($M_2 = M_a$).

Mass transfer is a crucial process for the evolution of binary systems and has a key impact on many binary physical properties. During mass transfer, the mass ratio changes, and the variation of q leads to a continuous change in the radii of the Roche lobes of both stars $r_{L,d}$ and $r_{L,a}$ (see Equation 1.15). Furthermore, the donor radius R_d changes in response to the loss of the envelope's outer layers, and it might either contract or expand, depending on the envelope's internal structure and on the mass transfer rate. Generally speaking, various authors suggest that stars with radiative envelopes tend to contract rapidly due to mass

loss, whereas stars with convective envelopes expand [234, 235]. Similarly to the donor, also the accretor's radius R_a changes because of mass transfer. Accretion onto a star can cause it to either contract or expand. When accretion rates are sufficiently high, this also results in a significant expansion of the star's radius relative to its main-sequence radius. As a result, the accretor may fill its own Roche lobe, resulting in the formation of a contact binary.

Estimating the response of both stars to mass transfer is challenging, especially when mass transfer is proceeding on very short time scales. However, constraining the relative changes of the RL and the donor's radius is crucial to predict the following evolution of a binary system and the stability of mass transfer [236, 237, 238, 239, 240, 241, 242, 243, 244, 245, 246].

If mass transfer is unstable, the binary system experiences a runaway situation, with increasingly high mass-transfer rates. The mass transfer accelerates to a timescale between the donor's thermal and dynamic timescale. The accelerated mass transfer dramatically affects the evolution of the binary, leading to a CE.

The CE can form not only because of the unstable runaway mass outflow from the donor star. Another path to the CE stage involves a tidal instability [247], [248], [249], [250], [251], [252], [253], which occurs when a system reaches a minimum of the total angular momentum for a synchronized close binary system [254]

$$L_{\text{min}} = 4 \left(\frac{1}{27} G \frac{M_1^3 M_2^3}{M_1 + M_2} (I_1 + I_2) \right)^{1/4} \tag{1.16}$$

where I_1 and I_2 are moments of inertia of first and second star. If the system's total angular momentum is less than L_{min}, the binary cannot remain in the synchronized rotation, leading to orbital decay and a CE phase. Angular momentum loss or tidal dissipation may occur due to many reasons [255]. For example, turbulent viscosity, where the shearing of tidally driven fluid oscillations in the convective envelope is dissipated as heat [256, 257, 258, 259]. The other is radiative dissipation in the stellar interior [260, 261].

A CE phase involving a star and a compact object can also start if mass transfer proceeds at so high rates, such as the super-Eddington rate [262, 263, 264], so that the compact object cannot accrete all of it.

1.4.2   Modeling the common envelope phase

We have already mentioned that the CE evolution is very uncertain from both the observational and theoretical points of view. This happens because (i) the CE phase is supposed to be very short ($\sim 10^4$ years), so it is very difficult to observe, (ii) the details of energy balancing considerations are difficult to constrain, and (iii) we have major uncertainties in stellar evolution calculations especially when rapid mass losses are involved.

Accurate three-dimensional hydrodynamic simulations might provide a comprehensive view of the processes within the overall envelope, however such simulations are very complex because the involve a very wide range of time and spatial scales [265, 266, 267, 268, 269, 270, 271, 272, 273, 274, 275, 276, 277, 265, 278, 279, 280, 281, 279, 282].

For fast population-synthesis calculations, the CE process is modeled using approximate approaches. The (α,λ)-formalism is one of the most used among the scientific community. This is based on simplified considerations on energy exchanges between the orbit and the envelope where α parameterizes the fraction of orbital energy transferred to the envelope, and λ is the envelope's binding-energy parameter.

The α_{CE} parameter parametrizes all sinks or sources of energy, such as radiative losses and, possibly, recombination energy. In this formalism, the condition for envelope ejection becomes

$$E_{\mathrm{bind}} \leq \alpha_{\mathrm{CE}} \, \Delta E_{\mathrm{orb}} \tag{1.17}$$

and, respectively, the condition for a merger is

$$E_{\mathrm{bind}} \geq \alpha_{\mathrm{CE}} \, \Delta E_{\mathrm{orb}} \tag{1.18}$$

.

The λ parameter is generally referred to as the envelope shape factor and it constraints the envelope energy reservoir for a specific binary star system.

A parameter λ was introduced by de Kool [283] as a numerical factor to simplify the computationally expensive calculation of the binding energy of the stellar envelope:

$$E_{\text{bind}} = -G \frac{M_{\text{d}} \, M_{\text{env}}}{\lambda \, a_i \, r_L} \tag{1.19}$$

where M_{env} is the mass of the donor's envelope.

A proper binding energy estimation is required to accurate prediction of a binary system's fate.

For many years, the λ parameter was used as a constant for all stars, independently of their initial mass M_{ZAMS}[6], chemical composition, metallicity Z, and, more importantly, stellar evolution phase. This is a rough approximation since the main stellar evolution parameters and evolutionary stage all have a crucial impact on the stellar envelopes' binding energies.

Using the (α, λ)-formalism, assuming that envelope is completely ejected, we can write the change of orbital energy as

$$\Delta E_{\text{orb}} = G \left(\frac{M_{\text{core}} \, M_{\text{a}}}{2 a_{\text{f}}} - \frac{M_{\text{d}} \, M_{\text{a}}}{2 a_{\text{i}}} \right) \tag{1.20}$$

By combining equation 1.20 with the energy balance equation $E_{\text{bind}} = \alpha_{\text{CE}} \, \Delta E_{\text{orb}}$, we can find the ratio between the final and the initial orbital semi-major axis:

$$\frac{a_{\text{f}}}{a_{\text{i}}} = \frac{M_{\text{core}} \, M_{\text{a}}}{M_{\text{d}}} \left(M_{\text{a}} + \frac{2 \, M_{\text{env}}}{\alpha_{\text{CE}} \, \lambda \, r_L} \right)^{-1} \tag{1.21}$$

---

[6]A star's initial mass is the star's mass at the beginning of the main sequence. Such mass is called the Zero-Age Main Sequence (ZAMS) mass.

By substituting equation 1.21 into equation 1.7, we obtain the following:

$$\tau_{GW+CE} = \frac{5}{256} \frac{c^5}{G^3} \frac{a_i^4 \, M_{\text{core}}^3 \, M_a^3}{M_d^4 \, (M_{\text{core}} + M_a)} \left(M_a + \frac{2 \, M_{\text{env}}}{\alpha_{\text{CE}} \, \lambda \, r_L} \right)^{-4} (1 - e^2)^{7/2} \qquad (1.22)$$

The time required for the coalescence of a binary system that evolves through a CE phase scales as

$$\tau_{GW+CE} \; \propto \; \alpha_{\text{CE}}^4 \, \lambda^4 \qquad (1.23)$$

The time required for a binary system to merge is highly dependent on the α and λ parameters, so their values have a crucial impact on the interpretation of many astrophysical systems, including merging compact-object binaries. While constraining the α parameter is challenging [284, 285, 286, 287], we can calculate the λ values and consider λ as a physical quantity instead of a parameter.

Many authors have already investigated the same problem for various stars at different evolutionary stages:

- Kruckow et al. [198] used the Bonn Evolutionary Code (BEC) [288, 289, 290, 291] to calculate λ parameters for two values of metallicity ($Z = Z_\odot/50$[7] and $Z = Z_\odot/2$) and for 5 initial masses of stars between 4 and 115 $M_\odot$,

- Klencki et al. [197] calculated λ parameters using the Modules for Experiments in Stellar Astrophysics (MESA) code [292, 293] for stars with initial masses M_{ZAMS} from 10 $M_\odot$ to 80 $M_\odot$, and for 6 values of metallicities,

- Xu and Li [195] calculated λ parameters adopting stellar evolution tracks from the EV code [294, 295] and considered initial masses M_{ZAMS} between 1 $M_\odot$ and 20 $M_\odot$ and two values of metallicity $Z = 0.02$ and $Z = 0.001$,

- Wang et al. [196] calculated λ parameters using the MESA code for stars with initial masses M_{ZAMS} between 1 $M_\odot$ and 60 $M_\odot$ at metallicity $Z = 0.02$.

---

[7]$Z_\odot = 0.0196 \pm 0.0014$ is metallicity of the Sun.

Despite the existence of self-consistent λ parameter calculations, a comprehensive and detailed analysis of λ parameters for all stellar stages at all possible metallicities and for a broad range of stellar masses is still missing, as well as studying the implications of self-consistent calculations of λ on large populations of binary stars and how up-to-date λ values can affect the formation of loud GW sources.

This thesis aims to perform self-consistent λ-parameter calculations for a large set of stars and metallicity using up-to-date stellar evolution tracks through the PARSEC code and study how new prescriptions of CEE affect the formation of loud GW sources with the use of the up-to-date population-synthesis code - SEVN.

Section 2 describes the methods and approximations we used to calculate the self-consistent binding energy parameters. Moreover, we describe the stellar evolution code used to obtain the stellar tracks. We also present the set of initial parameters of stars that we used in our calculations. In addition, we discuss the uncertainty in determining the boundary between the core and envelope of a star and describe how we evaluate the impact of this uncertainty on the obtained results.

Chapter 3 contains the main obtained results for CEE prescription and we show how various assumptions affect the calculation of binding energies.

We also show the results we obtained using a dedicated set of pure helium stars, where the stellar envelope is mainly composed of helium and the core of carbon and oxygen. We also compare the obtained binding energy parameters with the results of other authors (e.g., Wang et al. [196], Klencki et al. [197], Kruckow et al. [198], Claeys et al. [296], Giacobbo et al. [297]), and we analyze the sources of disagreement in the results and qualitatively evaluate the influence of the discrepancy on the interpretation of merging binary systems. Finally, we present fitting formulas for the new binding energy parameters for hydrogen and helium stars obtained in this work, and we evaluate their accuracy with respect to self-consistent data.

Chapter 4 focuses on population-synthesis codes and simulations. We have focused on

the SEVN code, which is based on the star tracks of the PARSEC stellar evolution code. Since our binding energies are obtained using the stellar tracks from the PARSEC code, it will be self-consistent to use the SEVN code to test our new prescriptions and study their impact on the evolutionary pathways of binary systems.

In this thesis, we focus mainly on introducing several technical improvements in the SEVN code (e.g., single and multi-node parallelization), which is the preparatory work that will be crucial to perform efficient simulations of large populations of binary stars and testing the new binding-energy prescriptions.

In section 5, we highlight all the main conclusions about the binding energy parameter and the influence of different physical parameters on its value. We also briefly emphasize all the main results obtained from the optimization of the SEVN population-synthesis code. We also present many follow-up projects that will be developed after the end of the PhD.

Finally, in section 5 we provide a link to an online repository with tables containing the binding energy parameters for all stars, evolutionary stages and metallicities. The tables contain fitting coefficients for both hydrogen stars and helium stars.

Chapter 2

Methodology

To calculate the binding energy parameter for stellar envelopes we used different approximations. In the zero-level approximation, we assumed that the envelope contains only gravitational energy. In this case, the formula for calculating the λ_g parameter is

$$E_{\text{bind}} = \int\limits_{M_{\text{core}}}^{M_{\text{d}}} - G\,\frac{M(r)}{r}\,\mathrm{d}m = -G\,\frac{M_{\text{d}}\,M_{\text{env}}}{\lambda_g\,a_i\,r_L} \tag{2.1}$$

where G is gravitational constant, a_i is initial semi-major axes, M_{d} is the mass of the donor, r_{L} is the radius of the Roche lobe 1.15, M_{core} is the mass of the stellar core and M_{env} is the mass of the stellar envelope. Thus, the λ_g parameter from equation 2.1 is

$$\lambda_g = -G\,\frac{M_{\text{d}}\,M_{\text{env}}}{R_{\text{d}}\,\displaystyle\int\limits_{M_{\text{core}}}^{M_{\text{d}}} - G\,\frac{M(r)}{r}\,\mathrm{d}m} \tag{2.2}$$

The values that define the integration interval in formula 2.1 are the first source of uncertainty. M_{core} depends on the criterion adopted to distinguish between the core and the envelope of an evolved star, which is not unique.

A better approximation of the λ parameter with respect to the previous one takes into

account both the gravitational and the thermodynamic energy of the envelope. The formula for calculating the λ_b parameter is

$$E_{\text{bind}} = \int\limits_{M_{\text{core}}}^{M_d} \left[-G\,\frac{M(r)}{r} + U \right]\,\mathrm{d}m = -G\,\frac{M_d\,M_{\text{env}}}{\lambda_b\,a_i\,r_L} \tag{2.3}$$

where U is the thermodynamic energy of the envelope. Explicitly,

$$\lambda_b = --\,G\,\frac{M_d\,M_{\text{env}}}{R_d \displaystyle\int\limits_{M_{\text{core}}}^{M_d} \left[-G\,\dfrac{M(r)}{r} + U \right]\,\mathrm{d}m} \tag{2.4}$$

Many distinct energy sources and sinks of the envelope complicate the computation of the thermal binding energy parameter, among which, the calculation of the thermal energy of the stellar matter, the radiation energy, and ionization energies.

Furthermore, Ivanova and Chaichenets [193], Ivanova et al. [192] proposed to consider enthalpy as a "new energy source". While enthalpy is not a real energy source, it plays a significant role in energy redistribution and causes quasi-steady outflows from envelopes. That is, enthalpy can significantly contribute to the envelope's outward acceleration, thus reducing, in practice, the total amount of energy reservoir that the envelope can subtract to the binary orbit before dissolving into space.

The critical aspect for considering enthalpy is the timescale of quasi-steady outflows. Ivanova and Chaichenets [193] stated that the timescale for these outflows is when the envelope redistributes the dumped heat, i.e., the thermal timescale (about a few hundred years). These time frames are consistent with the Podsiadlowski [298] results, according to which the self-regulating spiral-in stage can last up to 1000 years. Klencki et al. [197] questioned this suggestion because radiative losses in CE require a longer timescale for the CE ejection (more than 10^5 yr).

Taking into account enthalpy, the formula for λ_{h} is:

$$E_{\mathrm{bind}} = \int_{M_{\mathrm{core}}}^{M_{\mathrm{d}}} \left[-G\frac{M(r)}{r} + U + \frac{P}{\rho} \right] \mathrm{d}m = -G\frac{M_{\mathrm{d}}\,M_{\mathrm{env}}}{\lambda_{\mathrm{h}}\,a_i\,r_L} \qquad (2.5)$$

where P is the local pressure, and ρ is the density of the stellar layer. We can also write

$$\lambda_{\mathrm{h}} = -G\frac{M_{\mathrm{d}}\,M_{\mathrm{env}}}{R_{\mathrm{d}} \displaystyle\int_{M_{\mathrm{core}}}^{M_{\mathrm{d}}} \left[-G\frac{M(r)}{r} + U + \frac{P}{\rho} \right] \mathrm{d}m} \qquad (2.6)$$

From equations 2.2, 2.4 and 2.6, it is apparent that to calculate the binding energy parameters for a single star, we need to know, at each stellar evolution stage, the following quantities of the donor:

- total mass M_{d},

- the mass of the core M_{core},

- total radius R_{d},

- the thermodynamic energy $U(r)$,

- pressure $P(r)$,

- density $\rho(r)$

- and mass $M(r)$ distribution inside the star.

To compute these physical quantities, for this thesis, we used the **PA**dova and **TR**ieste **S**tellar **E**volution **C**ode (PARSEC, [121], [122], [123], [124], [125], [126], [299], [123]). We calculated them for a large set of stars with different initial masses M_{ZAMS} and metallicities Z.

During the simulation of a star's evolution, the PARSEC code records detailed data about the internal structure of the star. Each record contains information about approximately 40 shells inside the star, and they include the following local information that are relevant

for this work: local mass, radius, temperature, pressure, density, luminosity, gravitational energy, thermal energy, enthalpy, the local fraction of hydrogen, helium, carbon, nitrogen, and oxygen. The 40 shells are not distributed uniformly inside the star, as they are more dense where the star's internal structure is rapidly varying with the mass coordinate. Overall, during each simulation, the PARSEC code produces few thousand of such records.

We used the PARSEC code to calculate λ_g, λ_b, and λ_h for non-rotating hydrogen stars with metallicities $Z =$0.0001, 0.0005, 0.001, 0.002, 0.004, 0.006, 0.008, 0.014, 0.017, 0.02 and 48 values of initial masses, equally spaced in a logarithmic scale in the range between 2.0 $M_\odot$ and 600.0 $M_\odot$.

We also considered the possibility that pure-helium stars can act as donors during the CE phase. Helium stars are stars that have completely lost all hydrogen through either stellar winds or mass transfer in binaries. We used the PARSEC code to simulate the evolution of non-rotating helium stars with varying metallicities $Z =$0.0001, 0.0002, 0.0005, 0.001, 0.002, 0.004, 0.006, 0.008, 0.01, 0.02, 0.03, 0.05 and for 78 log-spaced values of initial masses in the range between 2.0 $M_\odot$ and 350.0 $M_\odot$. Claeys et al. [296], in the context of the Binary Stellar Evolution (BSE) code [300, 301, 178, 178, 302, 183], also considered the possibility of having a naked helium star as a donor for the CE phase, but they assumed $\lambda_b = 0.5$ for all pure-helium stars, independently of mass, metallicity, and stellar evolution phase. We compare results for helium-naked stars obtained using the PARSEC code with their constant value of λ_b in section 3.4.1.

Overall, we calculated binding energies for 1416 stellar evolution tracks, and for more than 100 points over each single track.

Throughout this work we will refer to the following stellar evolutionary phases:

- The Main Sequence (MS),
- The Terminal-Age Main Sequence (TAMS),
- Hydrogen-shell burning,
- Core-helium burning,

- Terminal Core-helium burning,

- Helium-shell burning.

We use x_{cen}, y_{cen}, xc_{cen} to refer to the central fractions of hydrogen, helium, and carbon, respectively. We use l_{x}, l_{y}, l_{c} to refer to the fraction of core luminosity that comes from hydrogen, helium, and carbon burning, respectively.

We identify the MS as the stellar evolution phase such that:

$$x_{\mathrm{cen}}(t) < x_{\mathrm{cen}}(0) \cdot 0.99, \quad x_{\mathrm{cen}}(t) > 10^{-3} \quad \text{and} \quad l_{\mathrm{x}}(t) > 0.6 \tag{2.7}$$

In contrast, the TAMS phase starts when:

$$l_{\mathrm{y}}(t) < 0.2 \quad \text{and} \quad x_{\mathrm{cen}}(t) < 10^{-3} \quad \text{and} \quad x_{\mathrm{cen}}(t) > 10^{-8} \tag{2.8}$$

The Hydrogen-shell burning phase starts when:

$$x_{\mathrm{cen}}(t) < 10^{-8} \quad \text{and} \quad l_{\mathrm{y}}(t) < 0.2 \tag{2.9}$$

The core-helium burning stage starts when:

$$l_{\mathrm{y}}(t) > 0.2 \quad \text{and} \quad x_{\mathrm{cen}}(t) < 10^{-8} \quad \text{and} \quad y_{\mathrm{cen}}(t) > 10^{-3} \tag{2.10}$$

We identify the Terminal Core-helium burning stage such that:

$$l_{\mathrm{y}}(t) > 0.2, \quad 10^{-8} < y_{\mathrm{cen}}(t) < 10^{-3} \quad \text{and} \quad x_{\mathrm{cen}}(t) < 10^{-8} \tag{2.11}$$

The Helium-shell burning stage stars when:

$$xc_{\mathrm{cen}}(t) > 0 \quad \text{and} \quad y_{\mathrm{cen}}(t) < 10^{-8} \tag{2.12}$$

All the PARSEC stellar tracks stop at carbon ignition, that is when

$$xc_{\mathrm{cen}}(t) > 10^{-8}, \quad y_{\mathrm{cen}}(t) < 10^{-8} and l_{\mathrm{c}}(t) > 0.5 \tag{2.13}$$

The boundary between the core and the envelope is one of the integration limits in the equations 2.2, 2.4, and 2.6. The criterion to define the separation between the outer edge of the core and the inner edge of the envelope of an evolved star is not unique. There are, at least, two main possible selection criteria.

- The first one is to consider the pure core of the star, i.e. the hydrogen-exhausted region in the star's center. The exhausted core can be identified through considerations on the local chemical composition. The helium core of a star is the inner region of a star that contains a very low fraction of hydrogen, for example, 15% ([195]) or 10% ([194]) of hydrogen or less. However, there are no unique threshold values for such a fraction of hydrogen, and this value is still actively debated.

- The second one is to consider the star's separation points, i.e., the boundaries between the radiative and convective layers of the hydrogen envelope. This method relies on the idea that the mass transfer might stop when the radiative layers are met, because the latter tend to respond to mass loss by shrinking while convective layers tend to expand. While the details depend also on the mass ratio of a binary, radiative layers are less prone to runaway mass-transfer scenarios (e.g., CE phase) since they allow stars to shrink faster than their Roche-lobe radius. This means that the actual core to consider during a CE evolution is the whole star minus its lost outermost convective layers (envelope).

Generally speaking, understanding what is the actual fraction of a star that is lost and forms the common envelope and the fraction that will remain bound to the donor as a "core" is challenging and it is closely associated to the response of the donor star to mass transfer. The stability of a lobe-filling star in close binary systems against mass loss on a dynamical

31

time scale is determined by the adiabatic response of that star to mass loss [241]. The donor's reaction is mainly a function of whether the envelope is convective or radiative. The ability of a star with a deep radiative envelope to contract rapidly in response to mass loss is intimately connected with the steep entropy gradient in its outer envelope [234, 235]. A star with a convective envelope has a nearly constant entropy profile and, therefore, expands upon the loss of the outer portion of the envelope [235]. Thus, a careful CE simulation requires following the detailed step-by-step response of the donor star.

Pre-determining the edge of the core using either of the two criteria mentioned above significantly simply the CEE, because they are supposed to be predictive of the following mass transfer stability, thus the CEE can be performed in only one step.

In our work, we considered the core as a hydrogen-exhausted region in the star's center, so we adopted the first of the two presented criteria. While simplified, the second criterion requires a more in-depth analysis of the layers within each stellar track, thus we will investigate its impact on λ calculations in a follow-up project.

To determine the boundary between the helium and carbon cores, we need to know the distribution of the hydrogen and helium fractions inside the star. We get these physical parameters from the PARSEC tracks. We found the mass and radius of the stellar core using the information about the star's chemical composition.

We tried different threshold values of hydrogen fraction and investigated how they affect the calculation of the binding energies with respect to adopting different criteria for defining the core-envelope boundary. We used the following criteria $X_{\mathrm{H}} =0.2$, 10^{-2}, 10^{-3}, 10^{-5}, 10^{-7}, 10^{-9} of hydrogen fraction to identify the helium core, and $X_{\mathrm{He}} =0.2$, 10^{-2}, 10^{-3}, 10^{-5}, 10^{-7}, 10^{-9} of helium fraction X_{He} to identify the carbon-oxygen core.

Chapter 3

Results

3.1 Impact of different core-envelope criteria

Figure 3.1 shows the evolution of binding energy, mass, and radius of a star with mass 5 $M_\odot$ and metallicity $Z = 0.002$ as a function of time. The figure has been obtained using the stellar track models of the PARSEC code. From figure 3.1 it is apparent the impact of using different criteria for the helium core-hydrogen envelope boundary. When we use the criterion $X_H < 0.2$, the helium core is formed before the hydrogen-shell burning phase, i.e. when the star is still on the MS. Specifically, the core emerges ~ 80 million years after the beginning of the MS. When we use $X_H < 10^{-9}$, the helium core is identified during the hydrogen-shell burning phase, i.e. ~ 88 million years after the beginning of the MS. As the carbon-oxygen core, when we use $X_{He} < 0.2$, the core emerges when helium is still burning in the core, about 95 million years after the beginning of the MS. When we use $X_{He} < 10^{-9}$, the carbon-oxygen core is identified later, ~ 200 hundred years after the beginning of the helium-shell burning phase.

From figure 3.1 it is apparent that different core-envelope boundary criteria do not significantly affect the value of the envelope's binding energy. The maximum uncertainty on the latter is always less than a factor of 2. Different criteria have also a mild impact on the
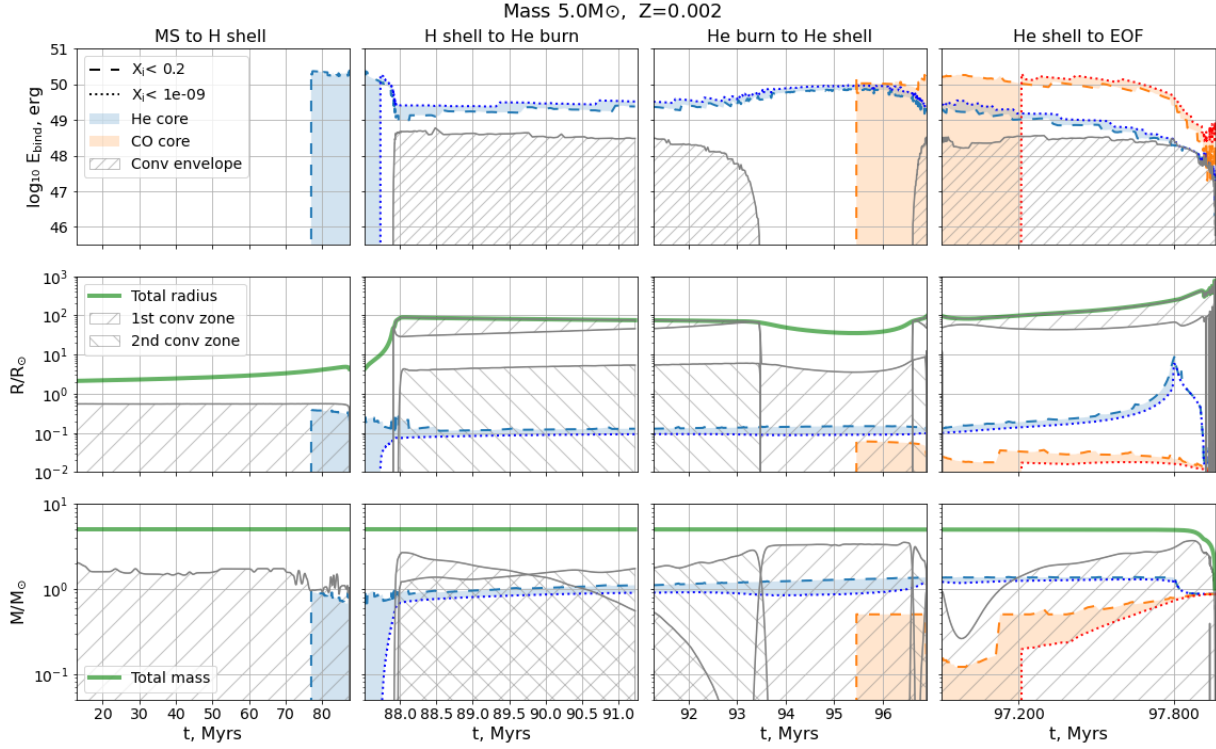
Figure 3.1: Evolution of various physical parameters of a 5 $M_\odot$ star at metallicity $Z = 0.002$, from MS to carbon ignition. The dashed (dotted) line shows the time evolution of the envelope's binding energy - top row, the radius of the core - middle row, and the mass of the core - bottom row, when using $X_i < 0.2$ ($X_i < 10^{-9}$) as core-envelope boundary criterion. The subscript i is hydrogen for young stars (i.e., helium core - shaded blue area), and helium for evolved stars (i.e., carbon-oxygen core - shaded orange area). The green solid line in the middle (bottom) row represents the evolution of the star's total radius (mass). The hatched region in the top row shows the binding energy of the hydrogen convective envelope. The right-hatched (left-hatched) region in the middle and bottom rows shows the radius and mass of the first (second) convective zones, respectively.

radius of the star at the moment of core identification. The latter is $R = 35.1\,R_\odot$ if we use $X_H < 0.2$, and it is $R = 99.4\,R_\odot$ if using $X_H < 10^{-9}$. The latter aspect might still have an impact on the CE evolution and merging compact-object binaries; if we use the criterion $X_H < 0.2$ we expect to have slightly more stars that survive the beginning of the CE phase without merging with the companion, that is stars that initiate an unstable mass transfer phase with a well-identified core.

Figure 3.1 shows also two first convective zones inside the star, in terms of binding energy, mass, and radial coordinate (grey hatched areas). The 5 $M_\odot$-star develops quite deep convective zones during most of its evolutionary history but at the end of the TAMS. Specifically, we define the convective envelope as the first convective zone that is no further from the surface of a star by more than 3% of the total stellar radius. Figure 3.1 shows that the convective envelope exists non-continuously during the evolution of the considered star. It is formed during hydrogen-shell burning phase and exists for ~ 3 million years, and then for ~ 0.5 million years during helium-shell burning. Instead of chemical-composition-based criteria, these convective regions might be used to define an effective core to be used during the CE evolution (see the discussion on the importance of convective layers in chapter 2). A detailed analysis of convective zones and the applicability of convection-based, core-envelope boundary criteria is beyond the scope of the thesis and it will be done in a follow-up project.

Figure 3.2 is very similar to figure 3.1 and shows the evolution of binding energy, mass, and radius of a star with an initial mass 60 $M_\odot$ and metallicity $Z = 0.002$, as a function of time. The impact of using different core-envelope criteria for 60 $M_\odot$ star is similar to that discussed for the 5 $M_\odot$-mass star in Fig. 3.1. The main differences are apparent in terms of convective zones. The star is fully convective at the beginning of MS. Then, very tiny convective zones appear during the helium-core burning stage, and during the helium-shell stage, the star becomes fully convective. For simplicity, we did not consider the third and fourth convective zones on figures 3.1 and 3.2. However, they exist for the star with an initial mass of 60 $M_\odot$ during helium-shell burning (at the star's age ~ 4.2 million years).
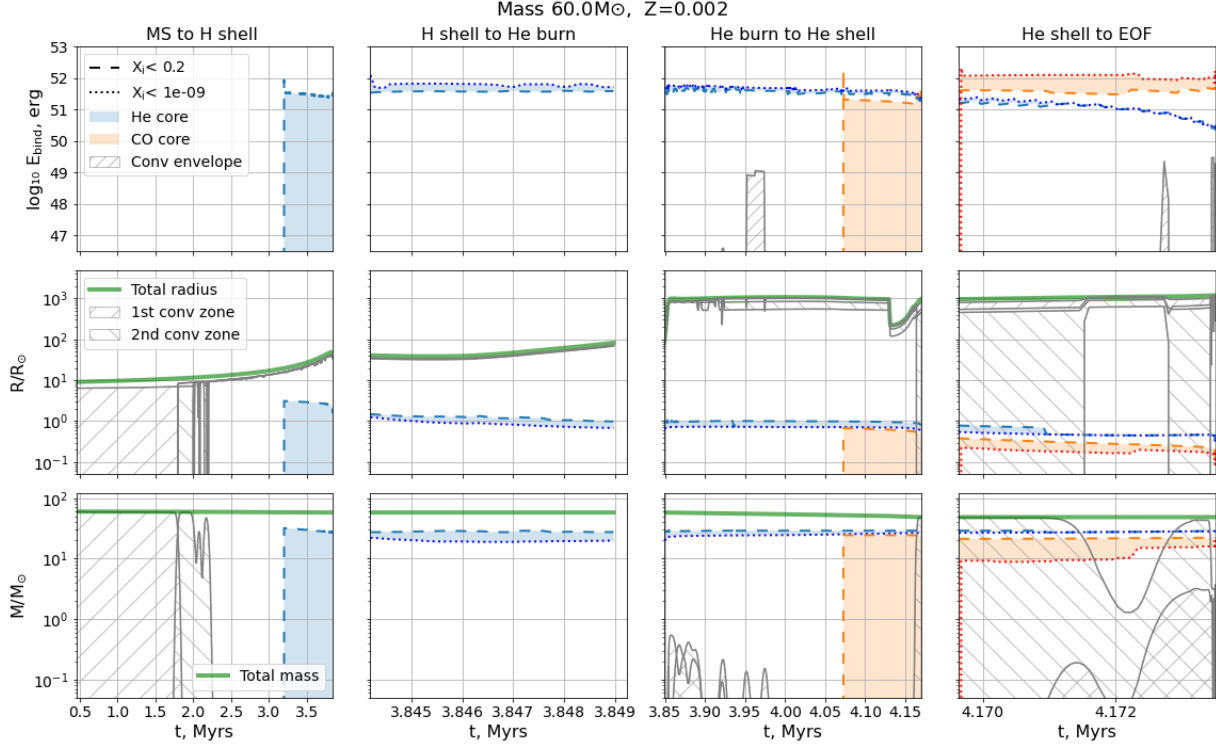
Figure 3.2: Same as Fig. 3.1 but for a 60-$M_\odot$ star.

Figure 3.3 shows the binding energy profiles and HR diagrams for stars with different initial masses at metallicity $Z = 0.001$.

Specifically, the width of the vertical shaded areas shows the uncertainty on the core's mass when using $X_H < 10^{-9}$ (left boundary, vertical dashed line) and $X_H < 0.2$ (right boundary, vertical dotted line), in units of solar mass. The figure shows that at the beginning of the hydrogen-shell burning phase (green solid line), the uncertainty in the mass of the core is significant (green shaded area). Specifically, for a star with an initial mass of 35 $M_\odot$, the uncertainty on the helium core mass is about 8 $M_\odot$, which is about 25% of the star's total mass. This happens because during this stellar evolution phase, the shell where hydrogen is burning is rapidly moving outwards and the helium core is quickly growing, thus the hydrogen fraction X_H is rapidly evolving. This uncertainty might have important implications for the CE evolution because, the hydrogen-shell burning phase is precisely when stars expand significantly and are likely to fill their Roche lobe, possibly evolving towards a
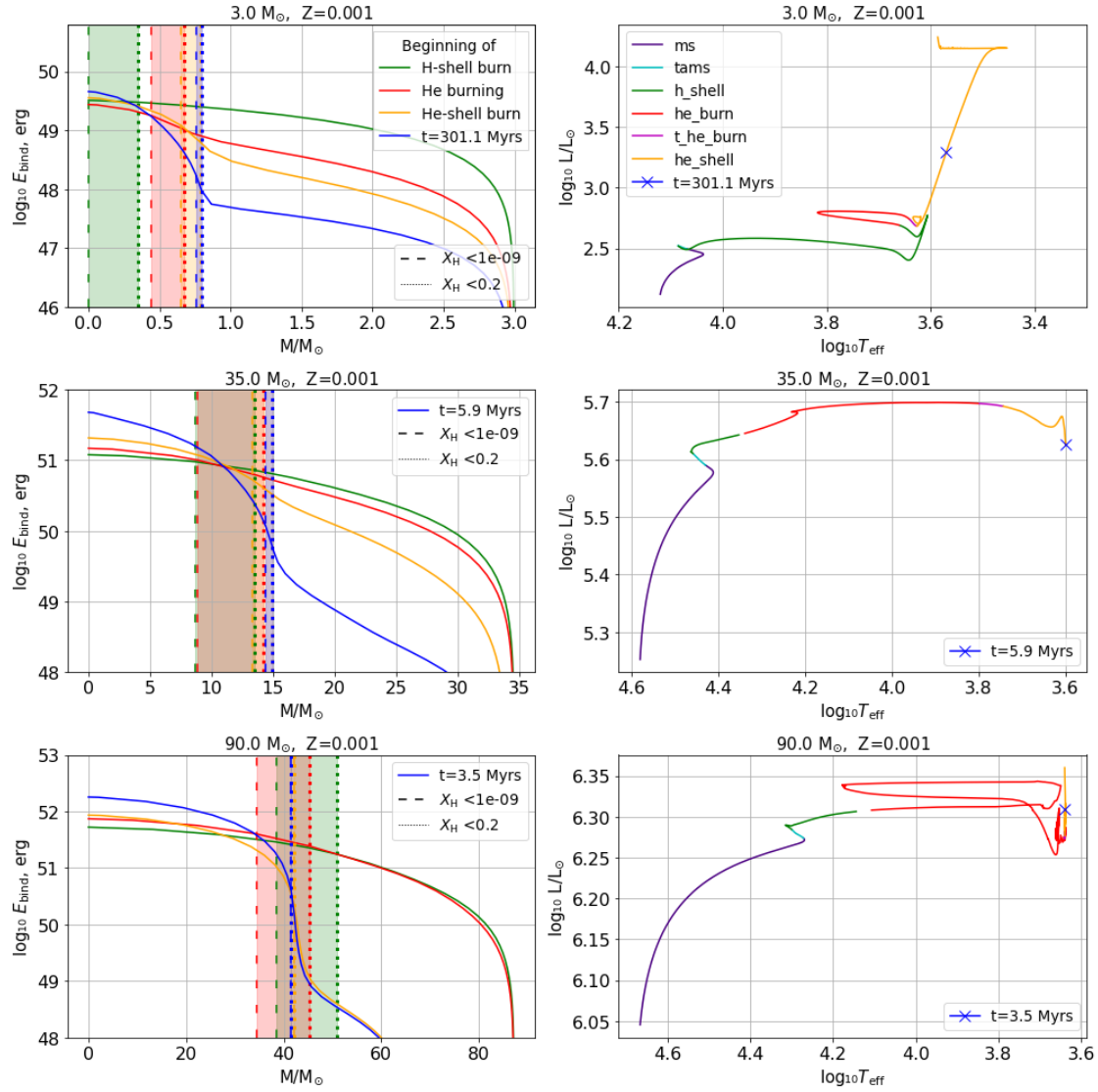
36

Figure 3.3: <u>Left column</u>: internal binding energy profile as a function of the mass coordinate for stars with masses 3 $M_\odot$ (top panel), 35 $M_\odot$ (middle panel), and 90 $M_\odot$ (bottom panel), at metallicity $Z = 0.001$. Different colored lines represent the binding energy profile at the beginning of various stellar evolution stages. Green: beginning of hydrogen-shell burning, red: beginning of he-core burning, yellow: beginning of he-shell burning, and blue: final snapshot of the PARSEC code, i.e. carbon ignition. The vertical shaded areas show the uncertainty on the core's mass when using $X_H < 10^{-9}$ (left boundary, vertical dashed line) and $X_H < 0.2$ (right boundary, vertical dotted line), at the beginning of various stellar evolution phases (same colors as solid lines). <u>Right column</u>: HR diagram evolution of the considered stars. Different colors represent different stellar evolution phases. The crosses mark the beginning of the different phases.

CE phase. The impact of using different values of X_H to identify the core-envelope boundary decreases significantly during the following stellar evolution phases (e.g., helium core and helium-shell burning).

Figure 3.3 also shows that the binding energy profiles behave very smoothly at the boundary of the helium core at the beginning of the early evolutionary stages. However, at the helium-shell burning stage, the energy profile strongly bends at the helium core boundary (blue lines). The bending in the binding energy profile is about two orders of magnitude or even more for star with initial mass 90 $M_\odot$. This means that even small variations on the criterion used to distinguish core and envelope might result in big differences in the calculation of the envelope's binding energy.

3.2 Binding energy parameters

3.2.1 Hydrogen stars

Figure 3.4 shows the binding energy parameters as a function of stellar radius for stars with different initial masses and metallicities. The binding energy parameters vary by a few orders of magnitude during the lifetime of most stars. Thus, depending on the stellar evolution phase, the outcome of a potential CE evolution can be significantly different.

The λ_g parameter significantly increases in the late evolutionary stages (i.e., helium-shell burning stage) for a star with initial mass 5 $M_\odot$ because the helium core's radius grows by two orders of magnitude (see figure 3.1). In contrast, the radius of the helium core of more massive stars remains almost constant (see figure 3.2), and the binding energy parameters for those stars tend to decrease.

The λ_b parameter for the star with initial mass 5 $M_\odot$ differs by three orders of magnitude compared to more massive stars in the late evolutionary stages. For example, the λ_b parameter for a low-mass star with a mass of 5 $M_\odot$ in the late evolutionary stage is equal to ~ 1. In comparison, the λ_b parameter for a massive star with a mass of 70 $M_\odot$ equals $\lambda_b \sim 10^{-2}$.
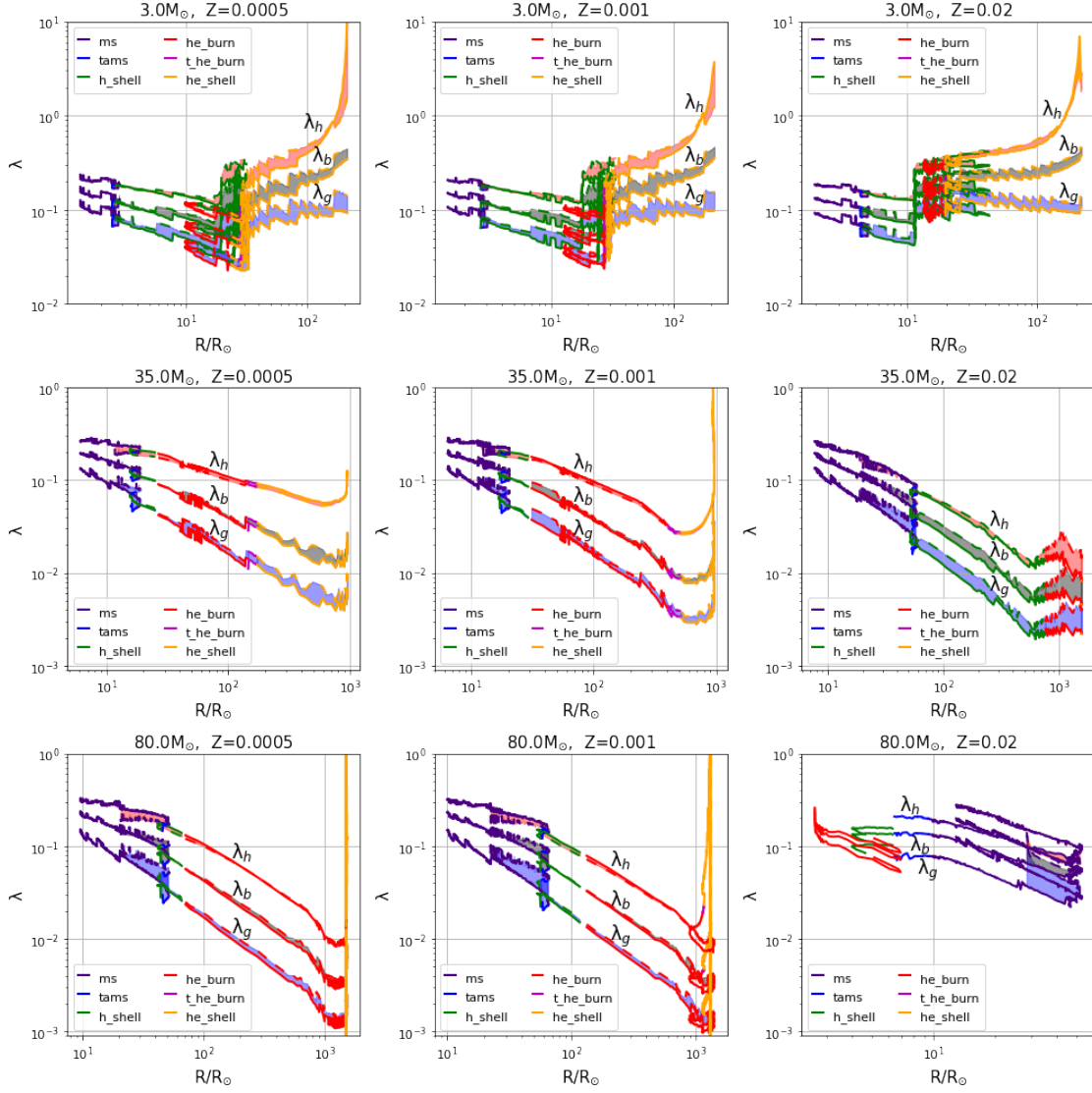
Figure 3.4: The λ_g (upper lines), λ_b (middle lines) and λ_h (bottom lines) parameters versus radius $R/R_\odot$ for stars with initial masses of 3 $M_\odot$ (first row), 35 $M_\odot$ (second row), and 80 $M_\odot$ (and third row), and metallicities $Z = 0.0005$ (left column), $Z = 0.001$ (middle column), and $Z = 0.02$ (right column). The colors of the lines indicate the evolutionary stage of stars: purple for MS (`ms`), blue for TAMS (`tams`), green for the hydrogen-shell burning (`h shell`), red for the core-helium burning (`he burn`), magenta for the terminal core-helium burning (`t he burn`), and yellow for the helium-shell burning (`he shell`). The thickness of the lines represents the uncertainty of using different core-envelope boundary criteria, i.e. $X_H < 10^{-9}$ and $X_H < 0.2$

That happens because of the expansion of the helium core and the effective temperature of low-mass stars rises during the helium-shell burning stage while the radius of the helium core of more massive stars remains constant, and the effective temperature decreases for massive stars during helium-shell burning (see figure 3.3). The temperature value directly affects the value of the internal energy of the star's envelope and, consequently, affects the λ_b parameter (see formula 2.3 and 2.4).

The thickness of the lines in figure 3.4 represents the impact of using different criteria to identify the core-envelope boundary on the values of λ_g, λ_b, and λ_h. Choosing different criteria for the core-envelope separation does not play a major role in the values of the lambda parameters. The maximum uncertainty on the λ parameter is less than a factor 1.5 for all stellar evolutionary stages and rarely reach a maximum of a factor of 3.

We can conclude that the binding energy parameters depend significantly on the evolutionary stage of the star and the star's initial mass. Additionally, we find that metallicity has little effect on the values of the λ_g, λ_b and λ_h parameters.

Fig. 3.4 shows the importance of determining the onset of mass transfer. Specifically, let us consider a star with a mass of 5 $M_\odot$ that initiates mass transfer at the end of the core-helium burning stage t_1 and the end of the helium-shell burning stage t_2. According to formulas 1.22 and 1.23, we get the following ratio of merger times via GW emission:

$$\frac{\tau(t_1, 5M_\odot)}{\tau(t_2, 5M_\odot)} \sim \left(\frac{7 \times 10^{-1}}{7 \times 10^{-2}}\right)^4 \sim 10^4 \tag{3.1}$$

Suppose that a star with a mass of 80 $M_\odot$ initiates mass transfer at the beginning of the core-helium burning stage (t_1) and the end of the core-helium burning stage (t_2). Then, we obtain the following ratio of merger times:

$$\frac{\tau(t_1, 80M_\odot)}{\tau(t_2, 80M_\odot)} \sim \left(\frac{5 \times 10^{-2}}{5 \times 10^{-3}}\right)^4 \sim 10^{-4} \tag{3.2}$$

The merger time can differ by four orders of magnitude over relatively short evolutionary

stages for the same star. At the same time, a star with a low mass tightens the binary system less effectively with time, while a more massive star tightens the binary system more effectively with time.

3.2.2 Helium stars

Figure 3.5 shows the binding energy parameters for pure-helium stars with different initial masses, metallicities, and using various core-envelope boundary criteria. The binding energy parameter varies considerably for low-mass helium-naked stars ($M \lesssim 8\,M_\odot$). For example, the λ_b parameter changes more than two orders of magnitude during lifetime of star with initial mass $2.2M_\odot$ and metallicity $Z = 0.02$, but less than order of magnitude for $Z = 0.0005$.

Binding energy parameters are roughly constant for helium stars with masses $M \gtrsim 8\,M_\odot$.

From figure 3.5 it is apparent that the λ parameters obtained for helium stars depend significantly on metallicity, but only for low-mass stars.

We compared the values of the λ parameters obtained for helium stars with the values obtained by other authors in section 3.4.1.

3.3 Merger time formula with CE phase

We can estimate semi-analytically the merger time of a binary system that has evolved through a CE phase. Our semi-analytical approach is based on a very rough assumption: we assume that all considered stellar binary systems initiate an unstable mass transfer phase, which leads to the formation of a CE that will be ejected from the system. We are neglecting the possible effect of SN explosions, further episodes of mass transfer, and any further orbit modification. Self-consistent population synthesis simulations are needed to take into account all the mentioned effects, so here we just discuss a qualitative estimation.

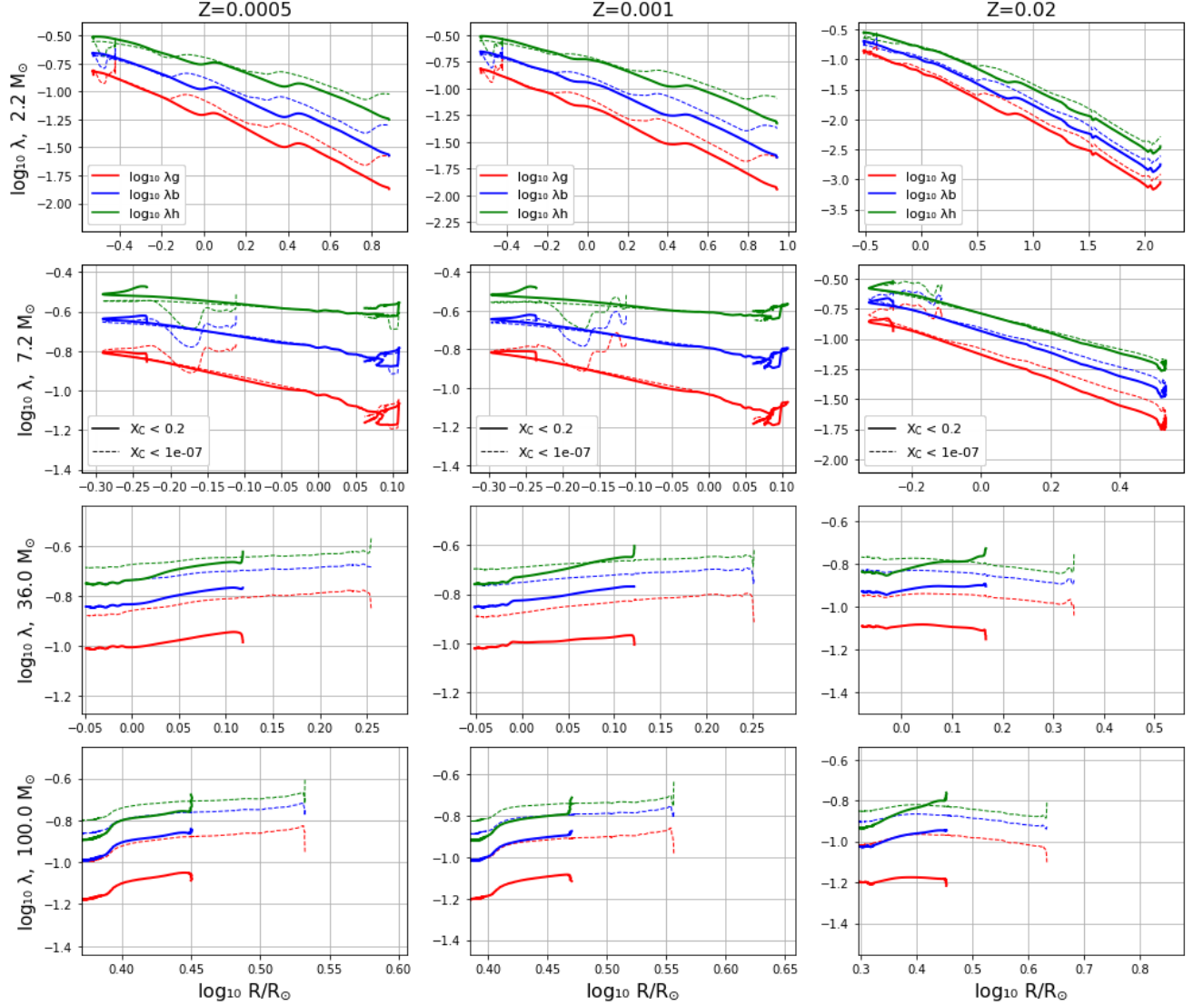To do semi-analytically estimation, we substitute the final semi-major axis from formula

Figure 3.5: The $\log_{10} \lambda_g$ (red line), $\log_{10} \lambda_b$ (blue line) and $\log_{10} \lambda_h$ (green line) parameters for helium stars with initial masses of 2.2 $M_\odot$ (first row), 7.2 $M_\odot$ (second row), 36.0 $M_\odot$ (third row), and 100.0 $M_\odot$ (fourth row) and metallicities $Z = 0.0005$ (left column), $Z = 0.001$ (middle column), and $Z = 0.02$ (right column), as a function of stellar radius. The solid and dashed lines show the values of the λ parameters calculated using the criterion $X_C < 0.2$ and $X_C < 10^{-7}$, respectively (see section 3.1).

1.21 as the initial semi-major axis in formula 1.7. Also, instead of the mass of a first star, we take the mass of the donor's helium core because we assume that the donor lost the entire hydrogen envelope to produce the CE. Furthermore, for the mass of a second star, we take the total mass of the accretor at the beginning of the mass transfer phase. Thus, we get the following formulas for the time of the merger of a binary system:

$$\tau_{\mathrm{GW+CE}} = \frac{5}{256} \frac{c^5}{G^3} \frac{a_\mathrm{f}^4}{M_{\mathrm{core}} \, M_\mathrm{a} \, (M_{\mathrm{core}} + M_\mathrm{a})} (1 - e^2)^{7/2} \tag{3.3}$$

where

$$a_\mathrm{f} = a_\mathrm{i} \frac{M_{\mathrm{core}} \, M_\mathrm{a}}{M_\mathrm{d}} \left(M_\mathrm{a} + \frac{2 \, M_{\mathrm{env}}}{\alpha_{\mathrm{CE}} \, \lambda \, r_L} \right)^{-1} \tag{3.4}$$

Now we substitute the radius of the Roche lobe 1.15 into formula 3.5:

$$a_\mathrm{f} = a_\mathrm{i} \frac{M_{\mathrm{core}} \, M_\mathrm{a}}{M_\mathrm{d}} \left(M_\mathrm{a} + \frac{2 \, M_{\mathrm{env}} \, \left(0.6 + q^{-2/3} \, \ln(1 + q^{1/3}) \right)}{0.49 \quad \alpha_{\mathrm{CE}} \, \lambda} \right)^{-1} \tag{3.5}$$

where $q = M_\mathrm{d}/M_\mathrm{a}$.

By replacing a_f in equation 3.3 with equation 3.5, we conclude that the timescale for a binary that evolved through the CE phase and will merge via the emission of GWs depends strongly on the value of the binding energy parameter. Thus, adopting self-consistent calculations of the λ parameters in complex population-synthesis simulations is crucial to obtain reliable results on the population of merging compact-object binaries. Specifically, fitting formulas obtained by other authors using different stellar evolution tracks should be adopted with care (see section 3.4).

3.4 Comparison of λ values with other authors

Wang et al. [196] calculated λ_g, λ_b and λ_h for stars with $Z = 0.02$ for 18 different values of masses in the range $M \in [1 \, M_\odot, 60 \, M_\odot]$. Wang et al. [196] adopted two different prescriptions for the wind mass loss rates, i.e. "Wind1" and "Wind2" models. The first one, denoted

as "Wind1", is the same as in [303, 304] The second one, denoted as "Wind2", takes the maximum value of the above loss rates in all the evolutionary stages, to be consistent with [305, 306].

Wang et al. [196] adopted the Modules for Experiments in Stellar Astrophysics (MESA) [292, 293] to calculate stellar evolution and to obtain the binding energy parameters. Wang et al. [196] applied polynomial formulas previously developed by Xu and Li [195]. The formulas for λ_g, λ_b and λ_h are the following:

$$\lambda_g = a_0 + a_1 x + a_2 x^2 + a_3 x^3 + a_4 x^4 + a_5 x^5 + a_6 x^6 \tag{3.6}$$

$$\lambda_b = a_0 + a_1 x + a_2 x^2 + a_3 x^3 + a_4 x^4 + a_5 x^5 + a_6 x^6 \tag{3.7}$$

$$\lambda_h = a_0 + a_1 x + a_2 x^2 + a_3 x^3 + a_4 x^4 + a_5 x^5 + a_6 x^6 \tag{3.8}$$

where x is $R/R_\odot$. a_i are fitting coefficients that can be found in Table 1 of [196]. For low-mass stars, Wang et al. [196] split stellar evolution into three stages and obtained the set of coefficients for three stages. "Stage 1" begins at the exhaustion of central hydrogen and ends when the star starts to shrink (i.e., near the ignition of helium in the core). "Stage 2" is the following shrinking phase, and in "Stage 3" the star expands again, until the end of the evolution.

We compared the λ parameters obtained using the fitting polynomials 3.6, 3.7, 3.8 with the coefficients reported in Table 1 of [196], with the results obtained in this thesis using the PARSEC stellar tracks.

Figure 3.6 compares our binding energy parameters with those obtained by Wang et al. [196], at metallicity $Z = 0.02$ and for stars with different initial masses. In the early stages of stellar evolution, the average difference between the values of the binding energy parameters is slightly less than an order of magnitude and decreases as the star evolves. At the end of the helium-shell burning phase, the discrepancy between the values of the λ parameters approaches zero. The discrepancy between the results for a star with mass of 18
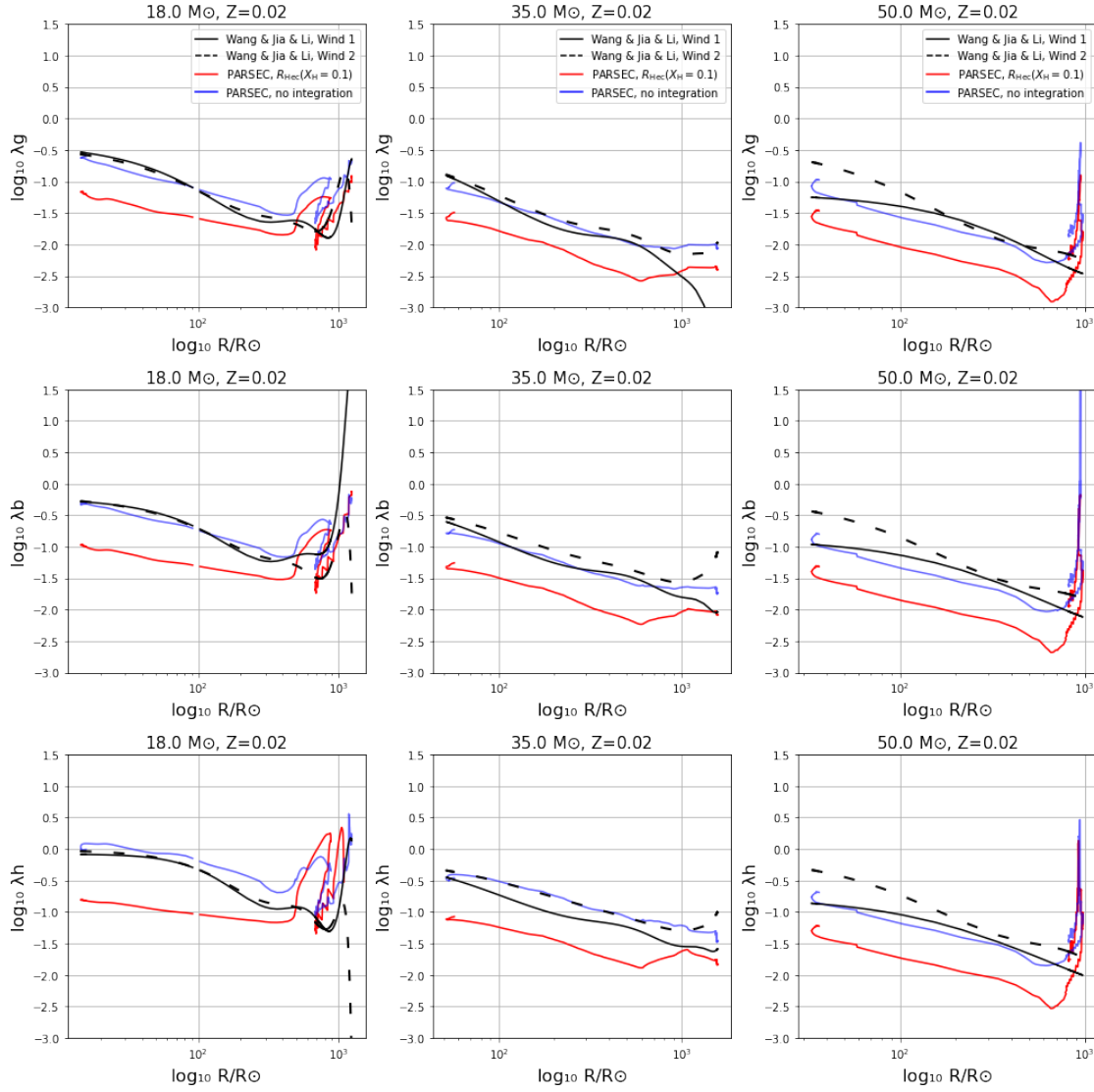
44

Figure 3.6: Comparison of our binding energy parameters with those from Wang et al. [196]. λ_g (top row), λ_b (middle row) and λ_h (bottom row) are shown for stars with $18.0 M_\odot$ (left column), $35.0 M_\odot$ (middle column), and $50.0 M_\odot$ (right column), at metallicity $Z = 0.02$. The red lines show the results calculated with the use of PARSEC tracks for hydrogen stars using a core-envelope boundary criterion $X_H < 0.1$. The black lines show the results of [196] for two different stellar wind models, "Wind1" - solid lines, "Wind2" - dashed lines.

The blue lines show the values of the binding energy parameter from the PARSEC code, obtained without integrating the binding energy from the core's outer boundary to the star's surface, but only when taking into account the energy of one layer of the star above the surface of the helium core (to be consistent with the methodology of [196]).

$M_\odot$ increases with the contribution of new energy sources to the λ parameter's value. That is, the difference between the λ_g parameters is less than that for the λ_b parameters, and the difference between the λ_b parameters is less than that obtained for the λ_h parameters. If the mass transfer occurs in early evolutionary stages, according to formula 1.23, we get the following discrepancy in merger time:

$$\frac{\tau_\mathrm{b,\ Wang\&Li}}{\tau_\mathrm{b,\ Nazarova}} \sim \frac{\lambda^4_\mathrm{b,\ Wang\&Li}}{\lambda^4_\mathrm{b,\ Nazarova}} \sim (7.5)^4 \sim 3 \times 10^3 \tag{3.9}$$

Variations in stellar evolution processes, wind models, and other factors may contribute to the explain the differences between our and their results. Wang et al. [196] also comment in [196] that the stellar tracks [195] obtained using the EV [294, 295] and MESA codes differ significantly in the early stages of evolution for stars with the same initial parameters.

An important aspect that is worth noting is that, as discussed in Section 2, the PARSEC code records the physical parameters for about 40 inner layers of the star during the simulations. In formulas 2.2, 2.4 and 2.6, the energies are integrated from the layer above the core to the surface (the outermost layer). In contrast, Wang et al. [196] take into account only one layer of the hydrogen envelope, i.e., the layer above the surface of the core. Therefore, to be consistent with Wang et al. [196], we need to ignore the energy contribution of many layers in the PARSEC stellar models. Taking into account only part of the stellar layers to calculate the envelope's binding energy produces results significantly more consistent with Wang et al. [196] (see Fig. 3.6, solid blue curve), but this has a crucial impact on the overall energy reservoir for a possible CE evolution.

Klencki et al. [197] obtained stellar tracks for rotating stars with an initial rotation rate of 40% of the critical value using the MESA stellar evolution code. Klencki et al. [197] provided fitting formulas of the binding energy parameters as a function of the radius of the
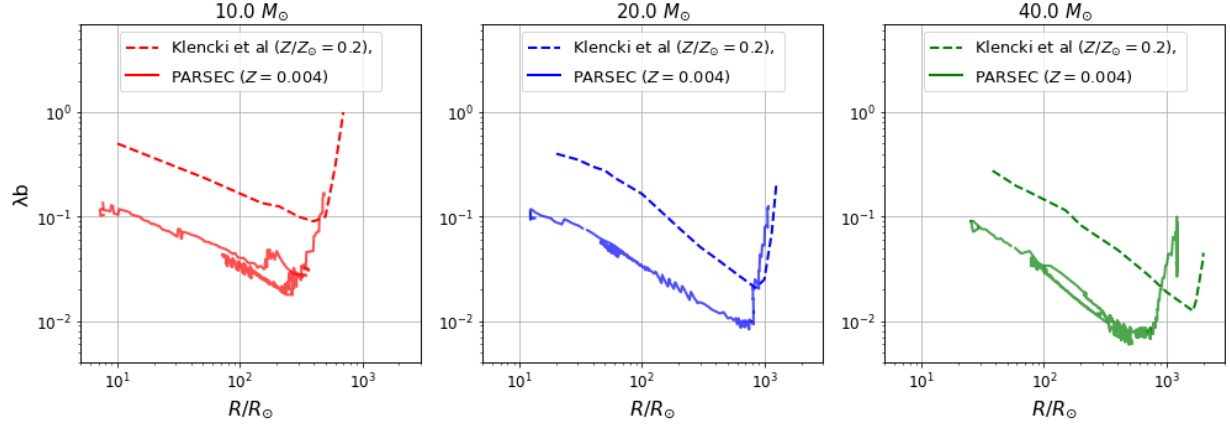
Figure 3.7: Comparison of the thermal binding energy parameters λ_b are shown for hydrogen stars with initial masses 10.0 $M_\odot$ (on the left), 20.0 $M_\odot$ (in the middle) and 40.0 $M_\odot$ (on the right). The colorful (red, blue and green) thin dashed lines shows the binding energy parameters λ_b presented in paper [197] on Fig.A.1 for metallicity $Z/Z_\odot \approx 0.2$. The colorful (red, blue, and green) thin solid lines show λ_b, calculated with the use of PARSEC tracks for hydrogen stars for metallicity $Z = 0.008$.

donor star using third-order polynomials (formula A.1 in [197]):

$$\log_{10}(\lambda) = a_i \log_{10}\left(\frac{R}{R_\odot}\right)^3 + b_i \log_{10}\left(\frac{R}{R_\odot}\right)^2 + c_i \log_{10}\left(\frac{R}{R_\odot}\right) + d_i \qquad (3.10)$$

Fig. A.1 in [197] shows the λ_b parameters obtained for stars with initial masses 10 $M_\odot$, 20 $M_\odot$, 40 $M_\odot$ and metallicity $Z/Z_\odot = 0.2$.

Figure 3.7 shows the result of the comparison of the thermal binding energy parameters with the results of Klencki et al. [197], for hydrogen stars with different initial masses. The difference in the results is about a factor of 5 for almost the entire evolution of the stars. According to formula 1.23, the average discrepancy in merger time is:

$$\frac{\tau_{b,\text{ Klencki}}}{\tau_{b,\text{ Nazarova}}} \sim \frac{\lambda_{b,\text{ Klencki}}^4}{\lambda_{b,\text{ Nazarova}}^4} \sim 5^4 = 625 \qquad (3.11)$$

One important difference that can partly justify the observed discrepancies is that Klencki et al. [197] considered rotating stars, while our set contains only non rotating stars. It means that the stellar physical properties of stars, including envelopes' binding energies, might differ
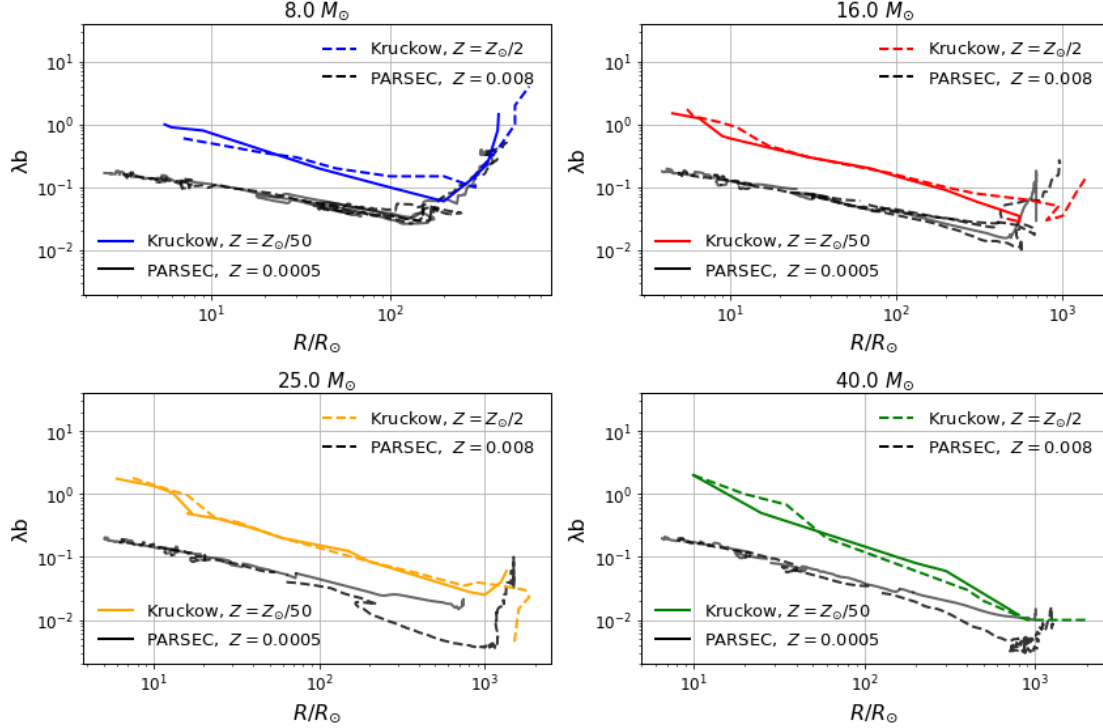
Figure 3.8: Comparison of the thermal binding energy parameters λ_b for hydrogen envelopes for stars with initial masses 8.0 $M_\odot$ (top left), 16.0 $M_\odot$ (top right), 25.0 $M_\odot$ (bottom left), and 40.0 $M_\odot$ (bottom right). as a function of stellar radius. Colored lines (blue, red, yellow, and green) show the binding energy parameters λ_b presented in Kruckow et al. [198] in their Fig.1. The black lines show the λ_b values calculated with the PARSEC code. Thin solid and thin dashed lines shows the result for $Z = 0.0005 \approx Z_\odot/50$, and $Z = 0.008 \approx Z_\odot/2$, respectively.

at the same stellar evolution stage depending on stellar rotation. Furthermore, we considered the envelope of hydrogen surrounding a star as a source of CE, while Klencki et al. [197] considered convective envelopes. Klencki et al. [197] established such initial parameters for simulations of stellar tracks to create stars with the largest possible convective envelope.

Kruckow et al. [198] used the Bonn Evolutionary Code (BEC) [288, 289, 290, 291] to obtain stellar tracks for stars at two different metallicities $Z = Z_{\mathrm{MilkyWay}} \simeq Z_\odot/2$ and $Z = Z_\odot/50$[1] and with initial masses between 4 and 115 $M_\odot$).

Based on the obtained tracks, Kruckow et al. [198] calculated λ_b and E_{bind} and presented the obtained values in their Fig. 1. Kruckow et al. [198] applied the $X_H = 0.10$ criterion for the core-envelop boundary.

---

[1] $Z_\odot = 0.0196 \pm 0.0014$ is the solar metallicity adopted in Kruckow et al. [198]

Figure 3.8 compares our results of binding energy parameters with Kruckow et al. [198] results. The difference in the values of λ at the end of the MS is about one order of magnitude and gradually decreases with the time for every considered star. If the mass transfer occurs at the end of the MS, according to formula 1.23, the average discrepancy in merger time via GW emission is:

$$\frac{\tau_{\text{b, Kruckow}}}{\tau_{\text{b, Nazarova}}} \sim \frac{\lambda_{\text{b, Kruckow}}^4}{\lambda_{\text{b, Nazarova}}^4} \sim 10^4 \tag{3.12}$$

The "Binary Star Evolution" (BSE) code [178, 178, 302, 183] is one of the first population-synthesis codes used to study the evolution of massive binaries and their impact on the demography of BH binaries. Stellar evolution is implemented in BSE through polynomial fitting formulas, making this code significantly fast. In addition to all aspects of single-star evolution, features such as mass transfer, mass accretion, CEE, collisions, supernova kicks, and angular momentum loss mechanisms are also included.

The Massive Objects in Binary Stellar Evolution (MOBSE) code [307, 297] is a customized version of BSE. With respect to BSE, MOBSE is a population-synthesis code that includes some important upgrades for the evolution of massive stars for both single stars and binary systems [308, 309, 310, 311]:

- new treatment for the natal kicks velocities,

- up-to-date equations for metal-dependent stellar winds including the dependence on the Eddington factor,

- recent models for core-collapse and electron-capture SNe,

- prescriptions for PISNe and PPISNe,

- updated formulas to compute the core radii,

- maximum initial mass up to 150 $M_\odot$.

As BSE, MOBSE uses Claeys et al. [296] fitting formulas to calculate the λ parameters to use during the CE phase.

Claeys et al. [296] calculated λ parameters for stars with deep convective envelopes using detailed stellar models obtained with the STARS stellar evolution code [312, 313]. To obtain λ parameters, Claeys et al. [296] developed a complex fitting formula that depends on multiple physical parameters: the star's radius at the beginning of MS, the mass of the convective envelope, total mass, total radius, and luminosity during stellar evolution. Also, Claeys et al. [296] formula depends on the evolutionary stage of the star. For example, the formula changes at the beginning of the hertzsprung gap (HG), giant branch (GB), core-helium Burning (CHeB), and asymptotic giant branch (AGB). Claeys et al. [296] described the formula in detail in their Appendix A.

We modified the MOBSE code by adding the values of the λ parameters as output values during runtime. Thus, we obtained the values of λ based on [296] formula and the stellar evolution prescriptions implemented in the MOBSE code.

Furthermore, we used the [296] formula substituting the necessary parameters (R_{ZAMS}, M_{env}, M, R, and L as extracted from the PARSEC stellar tracks.

Figure 3.9 shows the thermal binding energy parameter as a function of the star's radius during stellar evolution for stars with different initial masses and metallicities. The shown values have been obtained using:

- formula 2.4 and stellar tracks of the PARSEC code (solid line),

- MOBSE code (semi-transparent line),

- Claeys fitting formula used with the stellar physical parameters from the PARSEC tracks (dashed line).

The shaded areas on the figures highlight that part of the stellar evolution where the stars have a convective envelope according to the PARSEC stellar tracks.

There is substantial agreement between the λ parameters developed with the MOBSE code and those obtained with laeys formula + the PARSEC stellar tracks for all stars under consideration. This good match is because the MOBSE code uses Claeys' formula to calculate the binding energy parameters. The difference in the stellar tracks used in
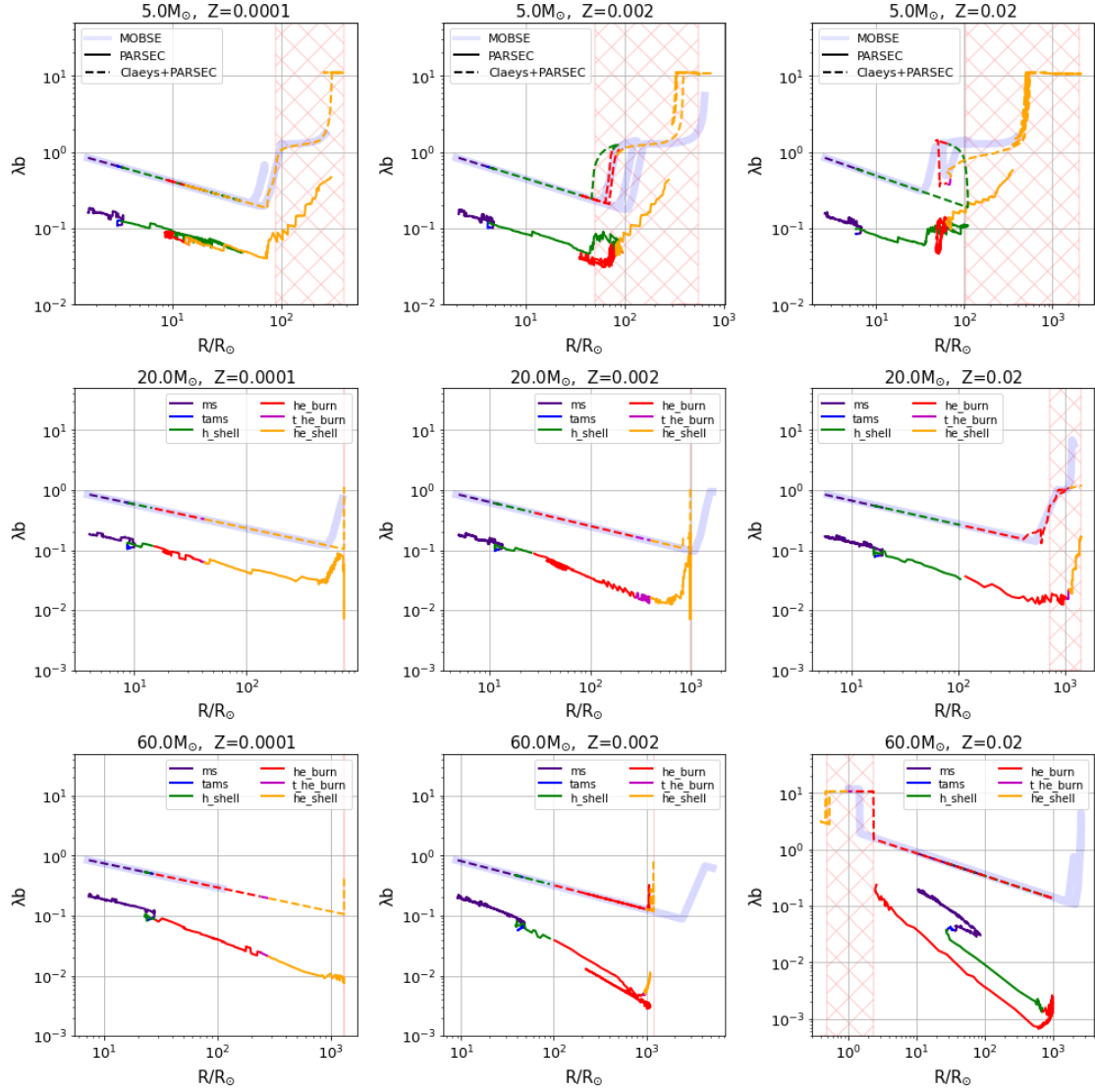
Figure 3.9: The thermal binding energy parameters λ_b versus radius of the star $R/R_\odot$ during stellar evolution for stars with initial masses 5 $M_\odot$ (first row), 20 $M_\odot$ (second row), and 60 $M_\odot$ (and third row) and metallicities $Z = 0.0001$ (left column), $Z = 0.002$ (middle column) and $Z = 0.02$ (right column). The colors of the lines indicate the evolutionary stage of stars: purple for MS (`ms`), blue for TAMS (`tams`), green for hydrogen-shell burning (`h shell`), red for core-helium burning (`he burn`), magenta for terminal core-helium burning(`t he burn`), yellow for helium-shell burning (`he shell`). Binding energy parameters λ_b are calculated with the use of different codes: MOBSE code (thick transparent blue line), PARSEC code (colored thin line), and Claeys formula from Appendix A in [296] with a PARSEC code stellar evolution tracks (colored dashed line). The hatched areas on plots highlight $R/R_\odot$ values where stars have a convective envelope according to the PARSEC stellar tracks.

the calculations may explain the discrepancy between the MOBSE and Clayes+PARSEC results.

More importantly, the λ_b parameters obtained with Claeys' formula (through both MOBSE and PARSEC+Claeys approach) and self-consistent calculations using the PARSEC of stellar tracks show significant differences. The difference between the results throughout the entire stellar evolution is about one order of magnitude, where the λ values from self-consistent calculation are systematically lower. However, the shape of the λ_b curve as a function of the stellar radius is very similar, especially for low-mass stars. For stars with a mass of 60.0 $M_\odot$ and a high metallicity value, the λ_b-parameter's behavior strongly diverges when the star becomes a Wolf-Rayet star. According to formula 1.23, the average discrepancy in merger time is:

$$\frac{\tau_{b,\ \text{MOBSE/Claeys}}}{\tau_{b,\ \text{Nazarova}}} \sim \frac{\lambda_{b,\ \text{MOBSE/Claeys}}^4}{\lambda_{b,\ \text{Nazarova}}^4} \sim 10^4 \tag{3.13}$$

Due to different stellar evolution processes, there is a large discrepancy between the λ parameters (see figures 3.6, 3.7, 3.8 and 3.9). Even minor differences in the physics of stellar evolution may significantly affect the binding energy parameters. For example, differences in stellar rotation (comparison with Klencki et al. [197]), different stellar winds models (comparison with Wang et al. [196]), criteria of core definition (comparison with Claeys et al. [296]), and many others. More importantly, Fig. 3.9 shows that is crucial to calculate the values of λ self-consistently, and using fitting formulas developed using other stellar evolution tracks might have a large impact on envelope's binding energies.

3.4.1 Comparison for helium stars

A value of $\lambda_b = 0.5$ was a widely used constant in the existing literature for pure-helium stars, for example, by [314, 315, 316, 213]. Specifically, BSE and MOBSE code use a constant $\lambda_b = 0.5$.

In our case, we can approximate the λ parameter value for helium stars with masses

$\gtrsim 8 \, M_\odot$ as a constant $\lambda_b = 0.15$ (see figure 3.5).

Following formulas 1.22 and 1.23, we get the following discrepancy in the merger time:

$$\frac{\tau_{\text{Nazarova}}}{\tau_{\text{Clayes}}} = \frac{\lambda_{\text{b, Nazarova}}^4}{\lambda_{\text{b, Clayes}}^4} \simeq 0.3^4 \approx 8.1 \times 10^{-3} \tag{3.14}$$

This means that similar star systems with the binding energy parameters obtained by us will merge a hundred times faster.

3.5   Fits and data

In this section, we provide fitting formulas that approximate our new λ values. Such fits might be useful to easily implement our new λ values in population-synthesis codes, especially those that are based on the PARSEC stellar evolution tracks (e.g., the SEVN code).

Here we present fitting formulas for the thermal binding energy parameter, which is chosen as fiducial model for the calculated λ values.

Due to the complexity of the variation of the lambda parameters, we chose functions that depend on two physical parameters. The function's first parameter is the star's radius during stellar evolution because such a parameter is common in fitting formulas and gives an accurate result for massive stars. We also chose the star's luminosity as a parameter, similarly to the fitting formulas of Claeys et al. [296].

We divide a star's evolution into two phases to obtain accurate fitting formulas. The reason for such a division is to separate the stages of stellar evolution when the structure of the hydrogen envelope is significantly different. As a criterion for separating the evolution of a star into two stages, we selected the star's minimum surface luminosity during helium shell burning. For simplicity, we refer to the stage from MS to the moment of minimum surface luminosity during helium-shell burning as "Stage 1". In contrast, "Stage 2" is the phase that goes from the minimum surface luminosity during helium-shell burning till the beginning of core-carbon burning or till the star becomes a Wolf-Rayet. We refer to a star

as a Wolf-Rayet star when its total mass of hydrogen falls below 3%. We excluded Wolf-Rayet stars because we have separate stellar tracks for such stars, thus we obtain the fits for pure-helium stars independently.

The fitting formula for a single hydrogen star with an any initial mass M_{ZAMS} at any metallicity value Z for the "Stage 1" is:

$$\log_{10} \lambda_{\mathrm{b}} = b_1 \ \log_{10} \left(\frac{R}{R_\odot} \right) + b_2 \ \log_{10} \left(\frac{R}{R_\odot} \right)^2 + b_3 \tag{3.15}$$

The fitting formula for the "Stage 2" is:

$$\log_{10} \left(\frac{1}{\lambda_{\mathrm{b}}} \right) = b_4 \ \log_{10} \frac{L_{\mathrm{eff}}}{L_{\mathrm{eff},0}} + b_5 \tag{3.16}$$

We have obtained b_1, b_2, b_3, b_4 and b_5 coefficients for a wide range of initial masses of hydrogen stars ($2.0 \, M_\odot \leq M_{\mathrm{ZAMS}} \leq 600 \, M_\odot$) and different metallicities ($0.0001 \leq Z \leq 0.02$) and uploaded them to the Binding Energy Parameters Online website. Also, the tables contain mean squared error (MSE) with respect to the real λ values, for each obtained fitting formula.

Instead of look-up tables, we have also obtained fitting formulas for the coefficients, which depend on the initial mass of the hydrogen stars. Such fits for coefficients can be applied to stars with any mass value but within a specific range of masses. The fitting formulas for the b coefficients are:

$$b_1 = a_1 \log_{10} M_{\mathrm{ZAMS}} + a_2 \tag{3.17}$$

$$b_2 = a_3 \log_{10} M_{\mathrm{ZAMS}} + a_4 \tag{3.18}$$

$$b_3 = a_5 \log_{10} M_{\mathrm{ZAMS}} + a_6 \tag{3.19}$$

$$b_4 = a_7 \log_{10} M_{\mathrm{ZAMS}} + a_8 \left(\log_{10} M_{\mathrm{ZAMS}} \right)^2 + a_9 \tag{3.20}$$

$$b_5 = a_{10} \log_{10} M_{\mathrm{ZAMS}} + a_{11} \left(\log_{10} M_{\mathrm{ZAMS}} \right)^2 + a_{12} \tag{3.21}$$

We have obtained a_1, a_2, a_3, a_4, a_5, a_6, a_7, a_8, a_9, a_{10}, a_{10} and a_{12} coefficients and MSE for the following initial mass ranges M_{ZAMS} of hydrogen stars:

- $2.0 - 7.5\ M_\odot$

- $8.0 - 20.0\ M_\odot$

- $25.0 - 50.0\ M_\odot$

- $60.0 - 90.0\ M_\odot$

- $100 - 600\ M_\odot$

and uploaded them to the Binding Energy Parameters Online website. Figure 3.10 shows the results of the fitting formulas for the thermal binding energy parameters as a function of the star's radius. The figure also shows the comparison between fitting formulas and real values of λ_{b}, including the estimation of maximum relative error as a function radius (small bottom panels). The results are shown for stars with different initial masses and metallicities. From figure 3.10 it is apparent that the derived fitting formulas is fairly accurate and the average relative error with respect to the real λ_{b} values is approximately $10^{-2} - 10^{-1}$.

Also, we obtained the fitting formulas for binding energy parameters of helium-naked stars. The fitting functions of helium stars' binding energy parameters depend on one physical parameter: the star's total radius. The fitting functions for helium stars are more straightforward because the λ parameter's time dependence is less complex than in hydrogen stars. We produced the fitting formula for a single helium star with an initial mass M_{ZAMS} and metallicity Z from the beginning of carbon-oxygen core production till the end of PARSEC tracks:

$$\log_{10} \lambda_{\mathrm{b}} = b_1\ \log_{10}\left(\frac{R}{R_\odot}\right) + b_2 \tag{3.22}$$

We obtained b_1 and b_2 coefficients and MSE for helium stars with every considered value of initial mass ($2.0 M_\odot \leq M_{\mathrm{ZAMS}} \leq 350.0 M_\odot$) and metallicity ($0.0001 \leq Z \leq 0.05$) and uploaded them to the Binding Energy Parameters Online website.
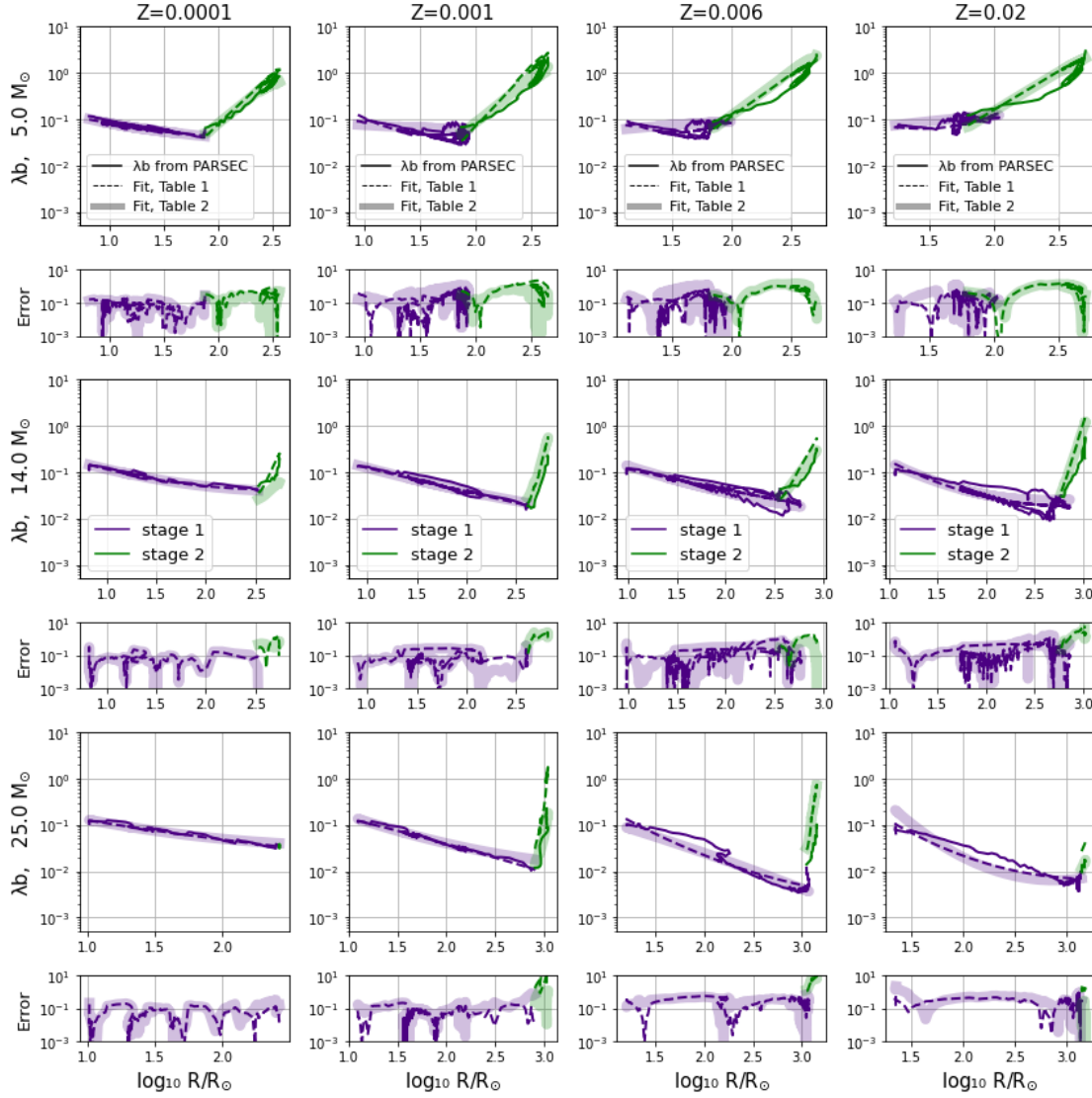
Figure 3.10: The λ_b parameters for hydrogen stars as a function of stellar radius for stars with initial masses $5.0 M_\odot$ (first row), $14.0 M_\odot$ (second row) and $25.0 M_\odot$ (third row), and for metallicities $Z = 0.0001$ (left column), $Z = 0.001$ (second column), $Z = 0.006$ (third column) and $Z = 0.02$ (fourth column). The purple line shows the "Stage 1" phase (i.e., MS to minimum luminosity during helium-shell burning), while green refers to "Stage 2" (from the end of Stage 1 until carbon ignition). Solid lines refer to the real values of the λ parameters. Dashed lines show the results of fitting formulas in Eqs. 3.15 and 3.16. Thick transparent lines show the λ values as obtained from the fitting formulas that include fits for coefficients, i.e. Eqs. 3.17, 3.18, 3.19, 3.20 and 3.21.
The subplots at the bottom of each row show the relative errors of fitting formulas with respect to real λ values.

We have also obtained fitting formulas for the coefficients b_1 and b_2:

$$b_1 = a_1 \log_{10} M_{\mathrm{ZAMS}} + a_2 \left(\log_{10} M_{\mathrm{ZAMS}}\right)^2 + a_3 \tag{3.23}$$

$$b_2 = a_4 \log_{10} M_{\mathrm{ZAMS}} + a_5 \left(\log_{10} M_{\mathrm{ZAMS}}\right)^2 + a_6 \tag{3.24}$$

We obtained a_1, a_2, a_3, a_4, a_5 and a_6 coefficients and MSE for the following initial mass ranges of helium stars:

- $2.0 - 7.0 \ M_\odot$

- $7.2 - 22.0 \ M_\odot$

- $24.0 - 70.0 \ M_\odot$

- $75.0 - 350.0 \ M_\odot$

and uploaded them to the Binding Energy Parameters Online website. These mass ranges were chosen to obtain the lowest possible median value of the MSE.

Figure 3.11 shows the results of fitted thermal binding energy parameters as a function of star's radius and comparison with the real values of λ_{b} for helium stars with different initial masses and metallicities. In most cases, the relative error is of the order of 10^{-2}.
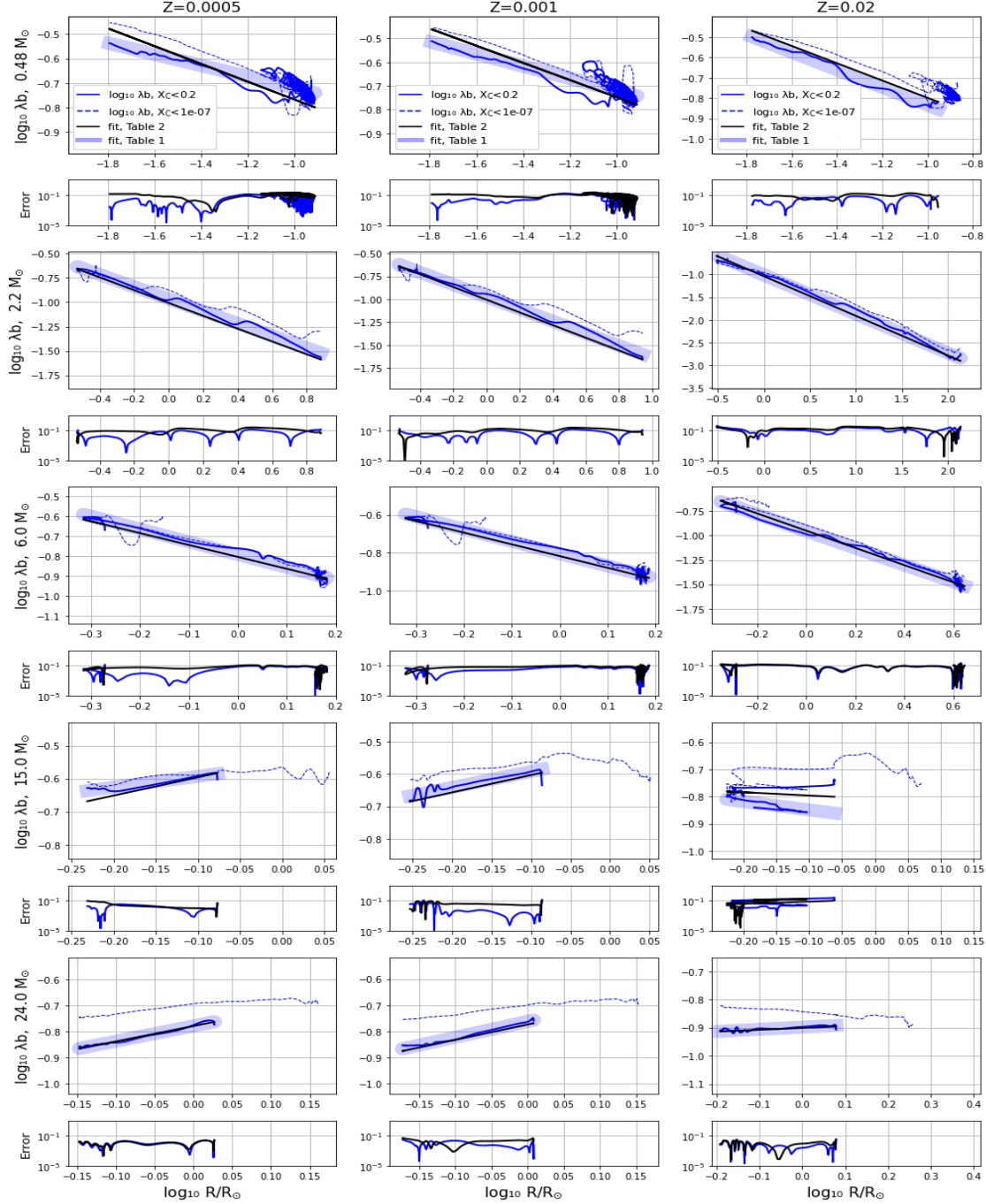
Figure 3.11: The thermal binding energy parameters $\lambda_{\rm b}$ for different helium stars during the latter stellar evolution. The initial masses are $0.48 M_\odot$ (first row), $2.2 M_\odot$ (second row), $6.0 M_\odot$ (third row), $15.0 M_\odot$ (fourth row), $22.0 M_\odot$ (fifth row), at metallicity $Z = 0.0005$ (left column), $Z = 0.001$ (second column), and $Z = 0.02$ (third column). Thin solid ($X_C < 0.2$) and thin dashed ($X_C < 10^{-7}$) blue lines show $\lambda_{\rm b}$ values obtained from PARSEC helium star tracks using the different core-envelope boundary criteria (see section 3.1). Thick transparent blue lines show values of the $\lambda_{\rm b}$ parameter with relative errors, fitted by formulas 3.22. Thin black solid lines show values of the $\lambda_{\rm b}$ parameter with relative errors, fitted by formulas 3.23 and 3.24.
The subplots at the bottom of each row show the relative errors of fitting formulas with respect to real λ values.

Chapter 4

Binary population synthesis and optimization of the SEVN code

The work presented in the previous chapters was related to single, isolated stars. To investigate the impact of the results presented in the previous chapters on the CE evolution and, consequently, on populations of merging compact-object binaries, we need to include our prescriptions in a population-synthesis code, which can (quickly) evolve a statistically significant number of binaries starting from early stellar evolution stages until the formation of compact objects.

Binary population synthesis (BPS) codes can provide valuable insights into the expected rate and distribution of the target population's properties, the different evolutionary pathways that lead to the formation of merging compact object binaries, and the effect that different physical processes and parameters have on their evolution.

In general, there are essentially three different approaches to implement stellar evolution in BPS codes:

- the most common method to quickly evolve the fundamental stellar parameters (e.g., luminosity, radius, mass, temperature, and chemical composition) far a large number of either single or binary stars as a function of time, is using polynomial fitting formulas.

Population-synthesis codes based on fitting formulas are computationally very fast, but updating fitting formulas with new prescriptions might be challenging. Some examples of BPSs based on fitting formulas are the "Single Star Evolution" (SSE, [317]), the "Binary Stellar Evolution" (BSE, [178]), the SEBA [318], the BRUSSELS CODE [319], the BINARYC [320], the STARTRACK [245], the "Compact Object Mergers: Population Astrophysics Statistics" (COMPAS, [321, 182]), the "Massive Objects in Binary Stellar Evolution" (MOBSE, [307, 297]), and the "Compact Object Synthesis and Monte Carlo Investigation Code" (COSMIC, [322, 323]).

- The second option is to utilize look-up tables instead of fitting formulas [324]. These tables include grids of pre-evolved stellar evolution models for single stars that are dynamically read and interpolated on the fly by BPS codes, for example by "Stellar Evolution for N-body" (SEVN, [118, 119, 120]) and COMBINE [325]. For binary stellar evolution such codes also use analytical prescriptions. This method is both computationally efficient and flexible. The main advantage is also that we can update stellar models by simply changing the look-up tables, without the need of modifying directly the code.

- Hybrid methods typically use population synthesis codes combined with detailed simulations of stellar and binary evolution [326, 327, 328, 329, 330, 331, 332, 333, 334] These studies show that including more detailed modeling of binary interactions may reveal details that are missed using simpler approaches. The "Binary Population and Spectral Synthesis code" (BPASS, [203]) and POSYDON [335, 336] use a hybrid approach to study the effect of detailed modeling of stellar and binary physics on compact object mergers.

In this thesis, we focus on the SEVN population-synthesis code, which is based on the look-up tables approach. This will allow us to easily implement the new λ descriptions developed in this thesis in the form of a new look-up table that SEVN can interpolate

on the fly. SEVN interpolates stellar evolution from look-up tables (the default tables being derived from PARSEC, [337, 338], includes five different models for core-collapse SNe, contains prescriptions for PPISNe and PISNe and has been updated to implement also binary evolution processes (wind mass transfer, Roche lobe overflow, CE, stellar mergers, tidal evolution, GW decay and magnetic braking).

Since SEVN is already based on PARSEC tracks, the obtained binding energy parameters will be fully self-consistent with the code.

The attributes for each object that we want to evolve can be set in the SEVN input file. If the object is a "single star", the input file needs to contain the following initial attributes:

- initial mass,

- metallicity,

- spin,

- stage of stellar evolution of each star.

If the type of the object to evolve is a "binary star", we need to specify the following initial physical quantities:

- initial mass of each star,

- metallicity of each star,

- spin of each star,

- stage of stellar evolution of each star,

- initial orbital distance,

- eccentricity of binary system.

Before implementing the new λ prescriptions, the SEVN code must be first optimized, especially in terms of performance, so that we can quickly simulate large population of binary stars (tens of millions, at least), that is an enough number to get statistically significant result on the population of merging compact-object binaries.

Parallel computing can accomplish this goal. The strategy to enable an effective parallelization of the SEVN code would be to divide the total number of objects to evolve into smaller groups and run their simulations simultaneously using different processing units (central processing units - CPUs or even graphics processing units - GPUs).

Supercomputers, workstations, and even personal laptops with multiple CPUs can execute parallel tasks. Workstations offer higher performance than mainstream personal computers, especially in CPU, graphics, memory, and multitasking. Distributed systems with many nodes, such as supercomputers, allow for massive parallelism.

We will achieve our main goal to speed-up the SEVN code by completing the following tasks:

- implementing the parallelization on a single computing node,

- doing the same for multi-node supercomputers,

- evaluating potential bottlenecks, including input-output operations and/or memory pressure, to understand how to further improve performance in the next future,

- evaluating a possible porting on GPUs.

4.0.1 Computer Architectures

We develop and test the parallel version of the SEVN code on the "Mizar" workstation (single node) and on the Ulysses Compute Cluster in SISSA (multi node). Mizar and Ulysses are both Linux-based systems. Mizar is a workstation, which contains 6 cores - 12 threads. In contrast, each node on the `regular2` partition of Ulysses contains:

- 2 sockets,

- 16 cores per socket.

- 2 CPUs per core,

- The maximum number of threads is 2 per core or 64 per node.
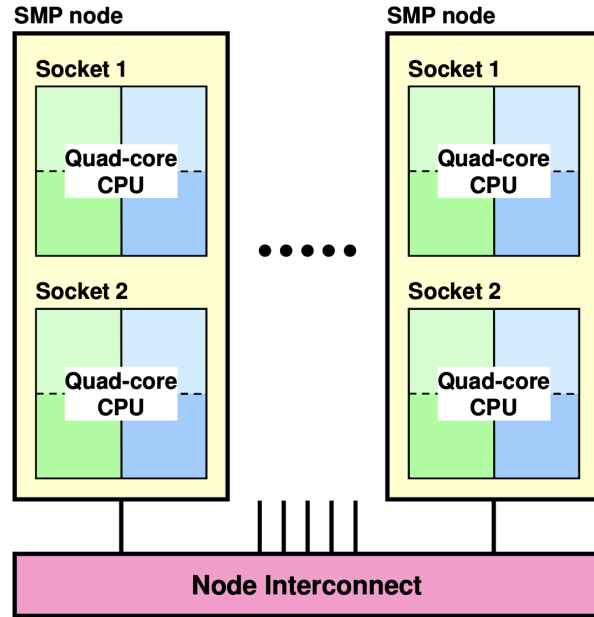
- Max available memory is 63500 MB.

Figure 4.1: Symmetric multiprocessing or shared-memory multiprocessing design.

The detailed information about Mizar and Ulysses (`regular2` partition) is presented in table 4.1. We chose the `regular2` partition of Ulysses because all nodes have the same configuration and available memory.

.

Ulysses has then been extended and a new infrastructure was made available during late 2019. This new infrastructure consists of additional nodes, an upgraded software stack and a new job scheduler, SLURM (Simple Linux Utility for Resource Management). After the upgrade the old nodes are used in partitions `regular1, long1, wide1` and `gpu1`, while the new nodes are available as `regular2, long2, wide2` and `gpu2` (datailed information on the Ulysses webcite).

Computer Architecture is very important for parallel computing. Total amount of CPUs, their type and amount of available memory constrain the total speed up and scaling of paralellization.

On Ulysses we used the following modules and compilers:

- `cmake/3.15.4` CMake is a cross-platform build system generator. Projects specify

63

Computer/property	Mizar	Ulysses, regular2
Architecture:	x86_64	x86_64
CPU op-mode(s):	32-bit, 64-bit	32-bit, 64-bit
Byte Order:	Little Endian	Little Endian
Address sizes:	46 bits physical, 48 bits virtual	
CPU(s):	12	64
On-line CPU(s) list:	0-11	0-63
Thread(s) per core:	2	2
Max Threads per Node		64
Core(s) per socket:	6	16
Socket(s):	1	2
NUMA node(s):	1	2
Max Memory per Node (MB)	15500 MB	63500 MB
Vendor ID:	GenuineIntel	GenuineIntel
CPU family:	6	6
Model:	62	79
Model name:	Intel(R) Core(TM) i7-4930K CPU @ 3.40GHz	Intel(R) Xeon(R) CPU E5-2683 v4 @ 2.10GHz
Stepping:	4	1
CPU MHz:	1253.196	1200.000
CPU max MHz:	3900.0000	2100.0000
CPU min MHz:	1200.0000	1200.0000
BogoMIPS:	6800.40	4190.39
Virtualization:	VT-x	VT-x
L1d cache:	192 KiB	32K
L1i cache:	192 KiB	32K
L2 cache:	1,5 MiB	256K
L3 cache:	12 MiB	40960K
NUMA node0 CPU(s):	0-11	0-15,32-47
NUMA node1 CPU(s):		16-31,48-63

Table 4.1: The table displays information about the architecture of Mizar workstation and Ulysses, regular2 partition.
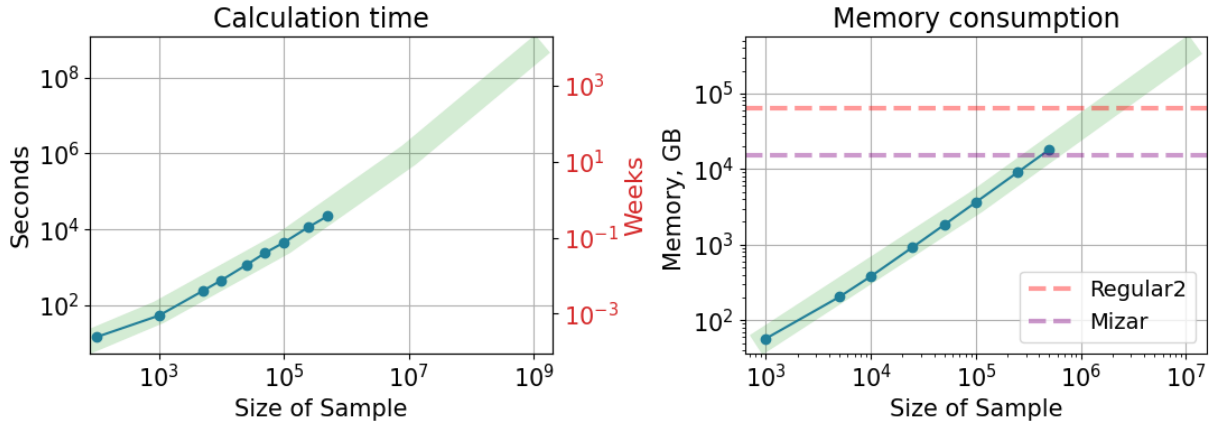
Figure 4.2: Left panel shows the computational time of SEVN for different numbers of binaries. The left vertical axis displays the total computational time for SEVN in seconds, while the right vertical axis displays the time in weeks. Right panel is the memory usage of SEVN for different numbers of binaries. The vertical axes represents the percentage of total available memory on the `regular2` partition during the execution of SEVN code. The dashed purple horizontal line represents the maximum memory available on the Mizar workstation.

their build process with platform-independent CMake listfiles included in each directory of a source tree with the name `CMakeLists.txt`. Users build a project by using CMake to generate a build system for a native tool on their platform.

- `gnu8/8.3.0` GNU module provides C++ compilers. The variant 3.15.4 supporting OpenMP and OpenACC offload is available. GCC 8.3 February 22, 2019 https://gcc.gnu.org/gcc-8/changes.html

- `openmpi3/3.1.4`

- `C++14`

4.1   Time and memory constrains

Currently, the SEVN code is not parallel and sequentially evolves a population of binary systems. Figure 4.2 shows the calculation time and the memory consumption of the serial SEVN code for different numbers of input binaries. Consumed memory is shown in units of available memory on each Ulysses `regular2` nodes, i.e. 64.0 GB. From Fig. 4.2 it is

apparent that the time needed to evolve 1 million binaries is approximately a week, which is a very large amount of time considering that, to have a statistically significant sample of merging compact-object binaries at all metallicities, we will need to evolve at least tens of thousands of binaries.

Also, it is apparent that the serial version of SEVN is a high memory-consumption code. Due to memory constraints, we can evolve up to one million binaries on Ulysses's `regular2` partition while only 500 thousand on Mizar's workstation. The memory consumption of SEVN is surely one of the aspects that must be improved, thus just speeding up the code's execution is not enough to guarantee sustainable performance on multiple architectures.

Specifically, the serial version of the SEVN code will complete the evolution of one set of billion objects over 1000 weeks or 19 years (see Figure 4.2). In addition, such calculations require an enormous amount of memory (more than 50 thousand GB) Thus, we need to modify the SEVN code to both (i) speed up the calculations, and (ii) avoid the high pressure on memory. To evaluate the performance of our parallelized code, we will evaluate the speed-up as:

$$S_{\mathrm{p}} = \frac{\text{execution time using one process}}{\text{execution time using } p \text{ processes}} = \frac{t_1}{t_{\mathrm{p}}} \tag{4.1}$$

4.2   Adaptive data loading

Device capabilities and size of the Random-Access Memory (RAM) vary a lot. Occasionally, the amount of data loaded during calculations may exceed the device's capabilities. To mitigate the issue of memory consumption of the SEVN code when evolving a very large number of binaries, we implement the following automatic strategy. The SEVN code splits the set of stars into chunks that fit into the available memory of the actual device. We call this method adaptive data loading.

We use some pre-load strategies to find the ideal adaptive chunk size for the device the SEVN code is running on. To find what is the maximum possible amount of binaries the

SEVN code can load without filling the hardware memory resources, we use the following proportional formula.

$$\text{Adaptive chunk} = \text{Memory Target Max} \ \times \ \frac{\text{Test Chunk}}{\text{Memory Consumed}} \qquad (4.2)$$

where "Test Chunk" is a test-reference sample of any size which we run with the SEVN code (for example, 1000 binary stars), and "Memory Consumed" is the memory consumption associated with the evolution of the test chunk. "Maximum Target Memory" is the maximum fraction of total Available Memory that we want to SEVN code to allocate during the simulation:

$$\text{Memory Target Max} = \text{Avail Memory} \times \text{Mem Perc Max} \qquad (4.3)$$

The SEVN code reads the total available memory from file `/proc/meminfo` on the fly. To estimate the memory consumed by the test chunk during the run, we use the difference between the amount of allocated virtual memory before and after the code lines that run the test sample. The file `/proc/self/status` contains the information about the current SEVN run, including information about the allocated virtual memory, i.e., Virtual Memory Resident Set Size (`VmRSS`). The SEVN code reads `VmRSS` from file `/proc/self/status` on-the-fly during its run and we can estimate

$$\text{Memory consumed} \ = \Delta\text{VmRSS} = \text{VmRSS}_2 - \text{VmRSS}_1 \qquad (4.4)$$

where VmRSS_2 and and VmRSS_1 are the amount of allocated virtual memory after and before the code run the test sample.

Users need to manually set the maximum percentage of memory "Mem Perc Max" the code can use during the run. In all our calculations, we use 80 % of the available memory on the devices. It is crucial to avoid the usage of all the available memory so to avoid filling up the resources of any system without control.

The formula 4.2 for calculating the adaptive chunk size assumes that the consumed memory scales linearly with the number of binaries. Figure 4.2 shows that this is a reasonable assumption.

4.3 Parallelization with OpenMP

After implementing the adaptive loading method, our next goal is to parallelize the SEVN code on a single computing node. We can accomplish the goal through the Open Multi-Processing (OpenMP) directives.

OpenMP is an Application Programming Interface (API) that supports multi-platform shared-memory multiprocessing programming. Multithreading, in which a single thread (a sequence of instructions executed in order) splits off into a number of parallel "sub-threads," is implemented in OpenMP. The threads are then scheduled to execute simultaneously, with the runtime environment distributing them across the available CPU cores.

The beginning of a parallel section in the code is identified through a compiler directive that initiates thread creation before the code is executed. Once the parallelized code has completed running, all created threads will merge back into the main thread, which continues the execution until the end of the run.

Each thread operates autonomously on its own copy of the parallelized code, by default. Using work-sharing constructs, it is possible to delegate specific portions of a task's execution to individual threads. OpenMP allows to accomplish task parallelism and data parallelism in this way.

Threads are distributed to processors by the runtime environment based on factors such as usage, machine load, and other conditions. The number of threads can be determined either by the runtime environment using environment variables or by the code using thread assignment functions. In C/C++, the "omp.h" header file contains the OpenMP directives.

In the SEVN code, all the objects to evolve can be either single or binary stars and their

initial conditions are stored into a C++ standard-template-library vector. In the following, we will only refer to binaries, though the parallelization and the presented results are the same for single stars. In our parallelization strategy, each OpenMP thread takes care of the evolution of only its part of binaries (Bin Per Thread), simultaneously to other threads:

$$\text{Bin Per Thread} = \text{std::ceil} \left(\frac{\text{Total Number of Binaries}}{\text{Total Number of Threads}} \right) \tag{4.5}$$

The adaptive chunk loading modulates the total number of binaries:

$$\text{Total Number of Binaries} = \min(\text{ Total Number of Binaries, Adaptive chunk }) \tag{4.6}$$

Function std::ceil(x) returns the smallest integer that is greater than or equal to x, so only the last OpenMP thread will evolve less binaries in case the total amount of binaries and adopted number of threads are not exact multiple of each other. Then each set of binaries evolves simultaneously within the `parallel` loop construct. The initial (Omp Start) and final (Omp End) binary that each thread must evolve within the parallel loop are then

$$\text{Omp Start} = \text{ Bin Per Thread } \times \text{ Thread ID} \tag{4.7}$$

and

$$\text{Omp End} = \min (\text{ Bin Per Thread} \times (\text{Thread ID} + 1), \text{ Total Number of Binaries })) \tag{4.8}$$

The main part of the code with OpenMP implementation is shown in the Appendix A.1. This shows only the core of the OpenMP implementation. The results of our OpenMP implementation are presented together with MPI results, in the next section (Sec. 4.4).

4.4 Parallelization with MPI

Message Passing Interface (MPI) is a standardized and portable message-passing standard designed to function on parallel computing architectures. MPI does not depend on its underlying programming language.

MPI and OpenMP enable parallel programming, but they have an important difference. MPI is used in distributed memory architectures. Unlike shared memory described above, distributed memory uses a collection of independent memory units that synchronize using a network, primarily found in supercomputers. It means that each core or node has a memory space of its own and does not require locks like shared memory.

However, synchronization is still required to distribute the computation and collect results, and that is done through message passing. OpenMPI provides API calls such as MPI_Send and MPI_Recv to allow communication between computation nodes. Unlike OpenMP, each computational unit has to send its results to a master and manually compile and aggregate the final result.

Global communication primitives are carried out on all processes belonging to the same communication group. By default, once MPI got initialized, all processes belong to the same group of communication called MPI_COMM_WORLD.

Typically, for maximum performance, to each CPU core will be assigned just a single MPI process.

To perform MPI parallelization, we divided the input binaries in the SEVN code into partitions, similarly to what we did for OpenMP, but now considering the total number of MPI processes:

$$\text{Bin Per MPI} = \frac{\text{Total number of binaries}}{\text{Number of MPI procs}} \tag{4.9}$$

Then the number of binaries is compared with the size of the adaptive chunk.

$$\text{Bin to do} = \min\left(\text{Bin Per MPI} - \text{Bin Done}, \text{Adaptive Chunk}\right) \tag{4.10}$$
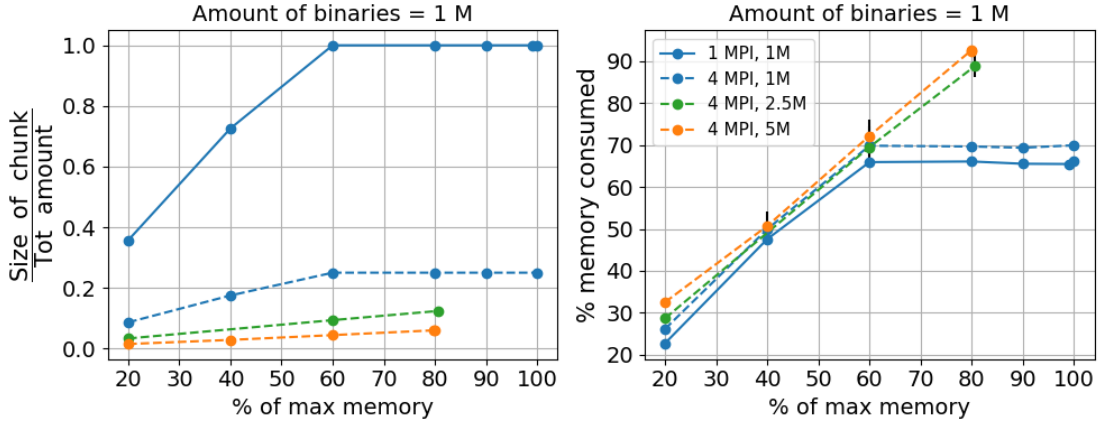
Figure 4.3: The relative size of a chunk (on the left) and the percentage of memory consumed during the run of SEVN (on the right) as the function of the maximum available memory. We obtained dependencies for 1 (blue lines) and 4 (orange lines) MPI processes.

An important aspect that it is worth noting is that here the adaptive chunk method must constrain the binaries to evolve per MPI process ("Bin per MPI") because, as already mentioned, each MPI process has its own memory copy of the binaries. Thus, if the number of binaries per MPI process requires more memory than is available on the device, then the evolution of objects by each MPI process happens in a loop. Specifically, depending on the available memory, increasing the number of MPI processes results in a decreased chunk size and, consequently, in a decreased speed-up (e.g., too few binaries per MPI process, see figure 4.3).

The main part of the code with MPI implementation is in the Appendix A.2.

Figure 4.3 shows the relative size of a chunk and the percentage of memory consumed in the process of calculations as the function of the maximum available memory. We obtained dependencies for 1 (blue lines) and 4 (orange lines) MPI processes. The figure shows that as the number of available memory increases, the adaptive chunk size grows linearly for 1 and 4 MPI processes. The size of an adaptive chunk for 4 MPI processes is approximately two times smaller than that for 1 MPI process. It happens because 4 MPI processes use more available memory to store in the memory vector with objects and more virtual memory per test chunk construct (see formula 4.2).
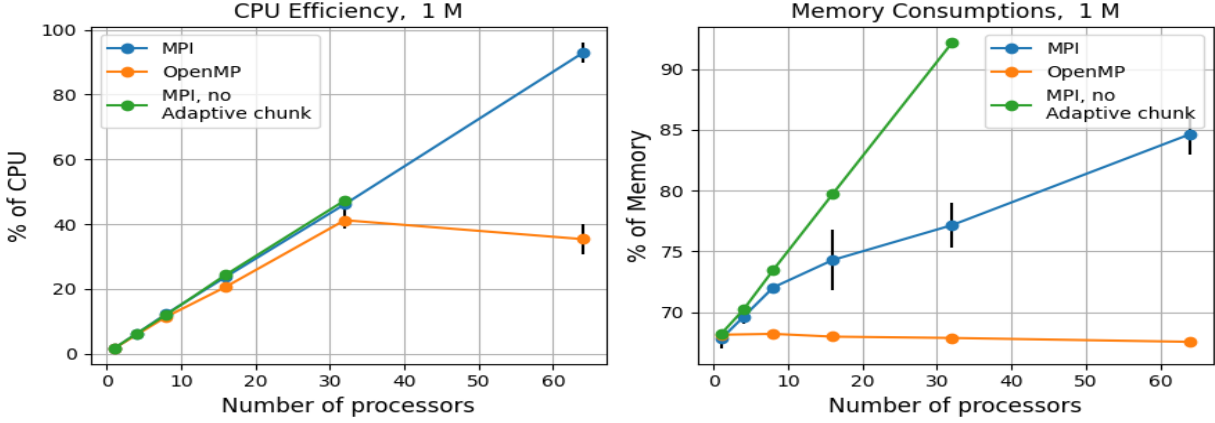
71

Figure 4.4: CPU efficiency (on the left) and memory consumption (on the right) for 1 million of input binaries for different amount of processors units (CPUs), used during the run.

The right side of Fig. 4.3 shows that the amount of physical RAM used for calculations differs from the maximum value of memory specified. For threshold values below 60%, the actual memory consumption is roughly 10% higher. This occurs because the SEVN code, initial data, and libraries take up about 10% of total RAM. The simulation's memory consumption stabilizes at approximately 70% at a threshold value greater than 60%. We assume this to be the case since the SEVN code data load is based on the interpolation of used virtual memory, not physical memory (see formula 4.2). During any program execution, virtual memory consumption is always greater than physical memory consumption.

Successful parallelization of code requires efficient use of both processing power (CPUs) and memory. Figure 4.2 shows that simulations of a million binary systems with serial SEVN code use all the available node memory on the Ulysses, `regular2` partition. We performed calculations using the parallelized SEVN code to check whether we had reached our mission. In Figure 4.4, we show the CPU efficiency and the memory consumption for one million input binaries. We can see that CPU efficiency grows almost linear with the number of threads or MPI processes. This outcome is consistent with our expectations, as we utilize more available CPUs while increasing the number of MPI processes or threads.

Memory consumption increases when using only the MPI interface, while for OpenMP, it remains constant. It happens for obvious reasons: With the OpenMP interfaces, processes
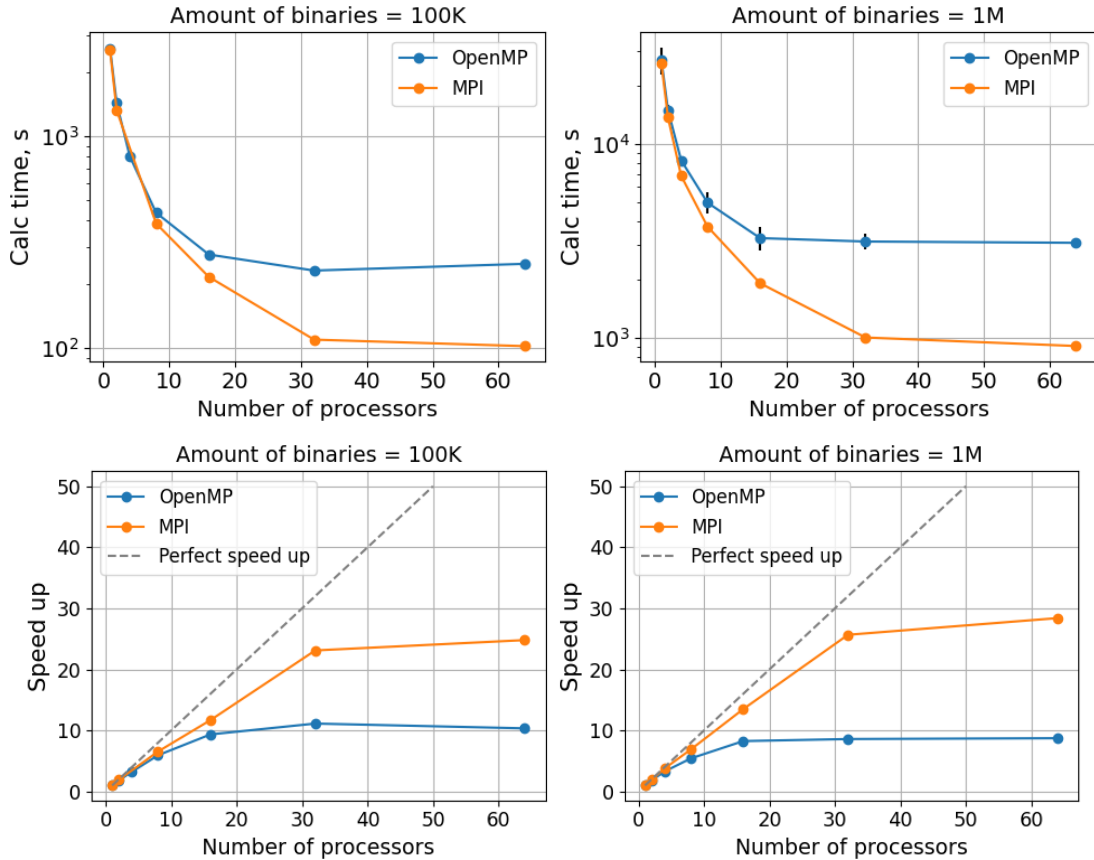
Figure 4.5: SEVN calculation time (on the top) and speed-up (on the bottom) for the different numbers used processors (CPUs) for 100 thousand and 1 million binaries. Calculations performed on Ulysses, `regular2` partition. The solid orange lines show the results with the use of the OpenMP interface, and the solid blue line with the use of the MPI interface. The dashed grey line is perfect speed up.

share memory and access an array of binary systems. With the MPI interface, all processes copy and allocate memory for the entire array of binary systems. Memory usage grows linearly without the adaptive chunk implementation. For a larger number of systems or employed CPUs, all available memory will be used for calculations.

Figure 4.5 shows the calculation time, and speed-up of the parallelized version of the SEVN code on a single node of the Ulysses computing cluster at SISSA (see Table 4.1), as a function of the adopted CPUs and for different total numbers of evolved binaries. We show the results of both the OpenMP and the MPI parallelizations.

We see that the code calculation time decreases by one order of magnitude when using

only the OpenMP interface and by a factor 25 when using only the MPI version of the code. The speed-up of the SEVN code when using MPI is quite close to the values of perfect speed-up. When using OpenMP, the speed-up saturates at 16 used CPUs and it gives a maximum speed-up of 10x on a single node.

The reason why the OpenMP version of the SEVN code stops scaling for a number of threads larger than 16 might be ascribed to false-sharing. Most high-performance processors insert a cache buffer between slow memory and the high-speed registers of the CPU. Accessing a memory location causes a slice of actual memory (a cache line) containing the memory location requested to be copied into the cache. Each update of an individual element of a cache line coming from different threads marks the line as invalid, and threads are forced to fetch a more recent copy of the line from memory, even though the element accessed has not been modified. As a result, there will be an increase in interconnect traffic and overhead. Also, while the cache-line update is in progress, access to the elements in the line is inhibited. If this occurs frequently, the performance and scalability of an OpenMP application will suffer significantly. This probably happens in our code since all the OpenMP threads access simultaneously the same C++ vector, which is shared among the threads.

If the issue is false-sharing, then the code needs to be restructured, especially when it comes to storing and accessing data. As a follow-up project, we will investigate whether it is worth restructuring the code for better OpenMP performance, or simply do a complete porting on, for example, GPUs, though the latter is beyond the scope of this thesis.

4.5   Hybrid Parallelization - MPI + OpenMP

We have many possible implementations of hybrid parallelization. To choose the best combination, we need to consider all the advantages and pitfalls of using OpenMP and MPI interfaces.

OpenMP: The advantage of using only the OpenMP interface is the ease of use, and the

data is not replicated as the number of threads increases. The latter is a major benefit for the SEVN code, which has high memory pressure. The major disadvantages are the reduced speed-up on a single node and the inability to perform parallelization on multiple nodes.

MPI: The main advantage of using MPI is increased performance, if a single process is assigned to a single CPU core, and the possibility to scale on multi-node computing clusters. Also, MPI is a good candidate for perfectly load-balanced applications. The main problem of MPI is memory consumption because each MPI process replicates the data. Specifically, if we start increasing the number of MPI processes, at some point, the adaptive data loading mechanism will force the chunk of binaries to a very small value, resulting in a compromised speed-up (see also Fig. 4.3)

Thus, with a hybrid parallelization strategy we might try to take full advantage of both OpenMP and MPI implementations. The hybrid approach will take the main advantage of MPI in terms of scaling performance across multiple nodes and the main advantage of OpenMP in terms of reducing memory pressure.

The optimal implementation of hybrid parallelization on a single node is an outer loop with an MPI interface and an inner loop with OpenMP. It is necessary to understand how to choose the optimal number of OpenMP threads per MPI process and the number of MPI processes per node.

So we tried the following combinations:

- 1 MPI process per socket, i.e. 2 MPI processes per node on Ulysses,

- 2 MPI process per socket, i.e. 4 MPI processes per node on Ulysses,

- 4 MPI processes per socket, i.e. 8 MPI processes per node on Ulysses.

We varied the number of threads for each combination from one to the maximum possible number. Figure 4.6 shows the calculation time and speed up depending on the number of CPUs used on a single node of the Ulysses cluster using 100 thousand binary star systems. We get the slowest calculations when using 2 MPI processes per node. When using 4 and 8 MPI processes per node, we get approximately the same calculation time/speed-up. Given
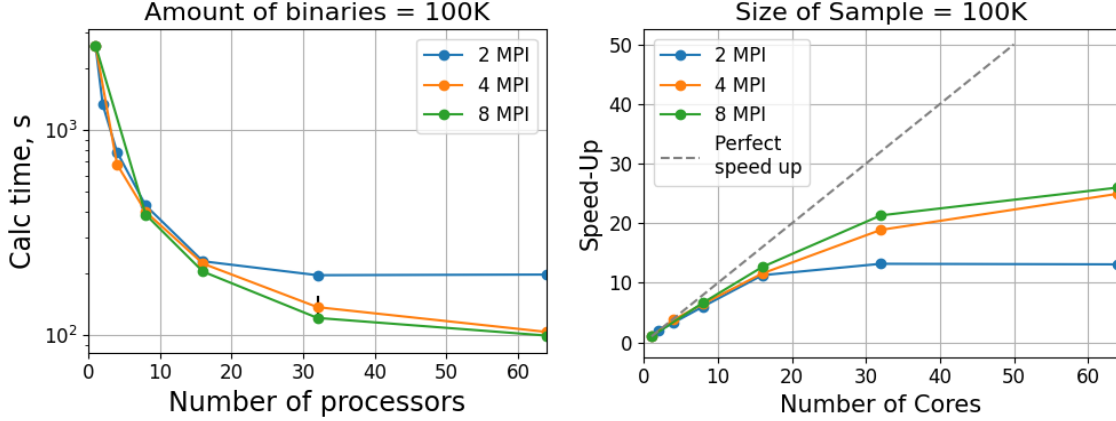
Figure 4.6: The calculation time (on the left) and speed-up (on the right) depending on the number of processors (CPUs) used. We obtained the results for 100 thousand binary star systems. During the calculation, we used 2, 4, and 8 MPI processes and a different number of threads. The dashed grey line is perfect speed up.

that 4 MPI processes use half as much memory as 8 MPI, we get the following optimal configuration of processes for the current version of the SEVN code on Ulysses: 2 MPI process per socket (i.e., 4 per node) and 16 OpenMP threads, i.e. total of 64 "processors", as in the x-axis of Fig. 4.6. Such a combination of MPI and OpenMP processes is favorable for large statistical sample simulations. As we stated above, a smaller number of MPI processes significantly softens the memory requirements and increases the size of the adaptive chunk.

Figure 4.7 shows the calculation time and speed-up of the SEVN code when using multiple nodes on the Ulysses cluster. We run the parallelized SEVN code on up to four compute nodes. The speed-up of the SEVN code with only MPI on one node (up to 64 CPUs) is about 25x. The speed-up on multi-nodes does not deviate significantly from a straight line:

$$\text{Speed-up}_p \sim \text{Speed-up}_1 \times p \tag{4.11}$$

where p is a number of the node. On four Ulysses compute nodes, with pure MPI, we get a speed-up of about 100x.

Hybrid parallelization gives approximately the same computation time and acceleration as pure MPI on a single node, but it uses significantly less memory. Therefore, despite a
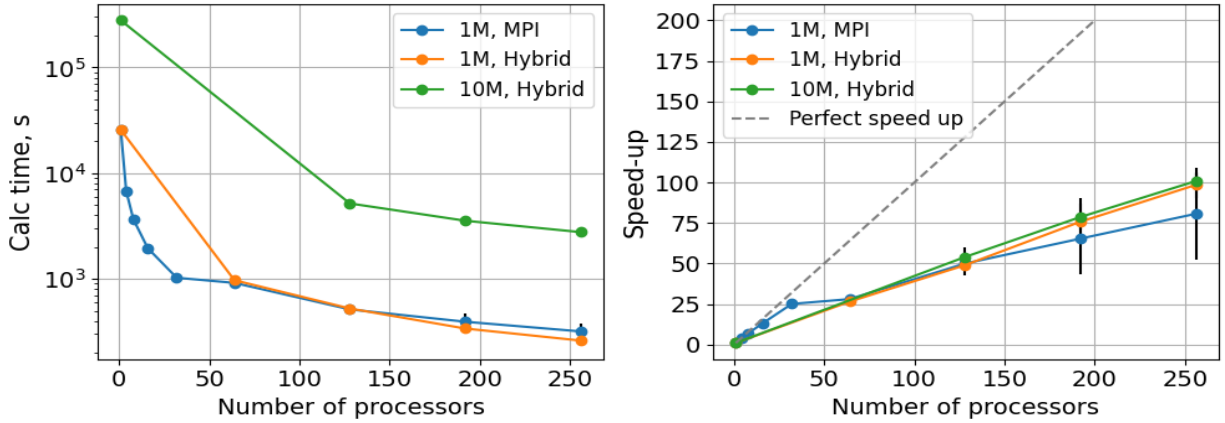
Figure 4.7: The calculation time (on the left) and speed-up (on the right) depending on the number of processors (CPUs) used. The solid blue lines show the results using the MPI interface on multiple nodes. The solid orange lines show the results using hybrid parallelization (both the OpenMP and MPI interface). We used 16 OpenMP threads and 4 MPI processes per node for hybrid parallelization. The dashed grey line is perfect speed up.

slightly lower speed-up on multi-nodes, hybrid parallelization has a more promising potential for very large statistical population samples, which will be run in the next months.

Chapter 5

Conclusions

Common envelope is a key binary stellar evolution process that is likely to play a crucial role in the formation and evolution of very tight binaries. Such systems have the potential to merge during the life of the Universe, and current and next-generation interferometers can detect gravitational waves from their mergers.

Despite its importance, our knowledge of the common envelope phase is hampered by the uncertainties we have in the details of stellar evolution and on the physics of the interaction between the stars and the (common) envelope. Self-consistent hydrodynamical simulations of CE are very complex and require powerful computation resources, thus state-of-the-art simulations performed through binary population-synthesis codes use approximate methodologies to treat this phase. The (α,λ)-formalism, where α is the efficiency of CE ejection and parametrizes the fraction of binary orbital energy transferred to the envelope, and λ is the envelope's binding-energy parameter

Both parameters play a vital role in predicting the fate of a binary system that evolves through CE and, consequently, on the astrophysical interpretation of gravitational wave sources.

For many years, the λ parameter was used as a constant for all stars. In the last decade, Wang et al. [196], Dewi and Tauris [194], Klencki et al. [197], Kruckow et al. [198], Kruckow

et al. [199] self-consistently calculated the λ parameter and demonstrated that it varies by two orders of magnitude during the life of stars. They also established that the parameter depends on the star's initial mass, metallicity, stellar wind model, and many other physical parameters.

Despite the availability of self-consistent calculations for the λ parameters, a comprehensive and detailed analysis of λ parameters across all stellar stages, metallicities, and stellar masses, is still missing. Furthermore, their impact in the formation and evolution of loud gravitational-wave sources in large populations of binary stars remains to be investigated.

In this thesis, we performed self-consistent calculations of the λ parameter for a large set of stars, at different metallicities, through an up-to-date version of the PARSEC stellar evolution code. We calculated the values of λ for non-rotating hydrogen stars with metallicities $Z =$ 0.0001, 0.0005, 0.001, 0.002, 0.004, 0.006, 0.008, 0.014, 0.017, 0.02 and 48 values of initial masses in the range between 2.0 $M_\odot$ and 600.0 $M_\odot$ (equally spaced in logarithmic scale). Furthermore, we also considered pure-helium stars as potential donors in the CE phase, and we performed self-consistent λ-parameter calculations for a large set of helium stars, at metallicity $Z =$ 0.0001, 0.0002, 0.0005, 0.001, 0.002, 0.004, 0.006, 0.008, 0.01, 0.02, 0.03, 0.05, and for 78 log-spaced values of initial masses in the range between 2.0 $M_\odot$ and 350.0 $M_\odot$.

We showed that the criterion for defining the separation between the outer edge of an evolved star's core and the inner edge of its envelope is not unique. However, identifying the stellar envelope-core boundary and the time of core production can affect the calculation of envelope's binding energies and the outcome of a possible common envelope phase.

We used a chemical composition method to determine the outer edge of the core: the helium (carbon) core is the inner region of a star with a hydrogen (helium) ratio below the threshold value. We investigated the effect of using different threshold values on our results: $X_{\text{H or He}} =$ 0.2, 10^{-2}, 10^{-3}, 10^{-5}, 10^{-7}, 10^{-9}.

Similarly to Wang et al. [196], Dewi and Tauris [194], Klencki et al. [197], Kruckow et al.

[198], Kruckow et al. [199], we found that λ parameters vary about two orders of magnitude during a star's lifetime (see figure 3.4). The λ parameters depend significantly on the initial mass of the star. For example, on figure 3.4 the λ_{b} parameter differs by three orders of magnitude for low-mass (5 $M_\odot$) and massive (70 $M_\odot$) stars. We did not find a significant impact of metallicity value on the value of the λ parameter, which agrees with findings of Dewi and Tauris [194], Wang et al. [196], Kruckow et al. [198], Klencki et al. [197]. The various criteria we have considered for determining the outer edge of the core do not make a significant contribution to the value of the λ parameters (see figure 3.4), though they can still have an impact on the number of binary systems that will survive a possible common envelope phase.

We also compared our results for hydrogen stars with those from other authors (see section 3.4 and figures 3.6, 3.7, 3.8 and 3.9). The main result we obtained is that our thermal binding energy parameter is about one order of magnitude less than Wang et al. [196], Klencki et al. [197], Kruckow et al. [198], Claeys et al. [296] results.

We also showed the binding energy parameters obtained for helium stars. We found that the λ parameters can vary significantly during the stellar evolution of low-mass stars. For example, λ parameters for star with initial mass $2.2\,M_\odot$ and $Z = 0.02$ vary more than two orders of magnitude during stellar evolution (see figure3.5). For massive helium stars ($> 8M_\odot$), the λ parameters are approximately constant ($\lambda_{\mathrm{b}} = 0.15$). Since self-consistent calculations for the λ parameter of helium-free stars were not performed, Claeys et al. [296], the BSE and MOBSE codes use a constant $\lambda_{\mathrm{b}} = 0.5$ for helium stars. The PARSEC code yields λ parameter values for massive helium stars that differ by a factor of three from the generally accepted constant. The binding energy parameters for massive helium stars also do not depend on the metallicity value and the criteria for determining the core-envelope boundary. However, the λ parameters of low-mass helium stars depend significantly on metallicity. For example, the λ parameters for the star with initial mass $2.2\,M_\odot$ and $Z = 0.0005$ vary by less than the order of magnitude, while the star with mass

$2.2\,M_\odot$ and $Z = 0.02$ vary 2.5 times during stellar evolution.

The main result is that differences in the details of stellar evolution calculations, such as stellar rotation, stellar winds models, criteria of core definition, and overshooting, can have a crucial impact on the calculation of the λ parameters for both non-naked and naked-helium stars. Thus, having self-consistent calculations for the envelopes' binding energies is a crucial step that must be performed before studying populations of merging compact-object binaries via population-synthesis codes.

In Sec. 3.5 we also provide fitting formulas for our values of λ for both non-naked and naked-helium stars. The fits coefficients and λ tables can be downloaded from the website github.com/NataNazar/Binding_energy_parameters.

As next steps, we will soon implement a new look-up table in the SEVN code containing the new set of λ parameters and we will run many population-synthesis simulations of binary systems, with different initial conditions, and we will study the impact of the new self-consistent λ calculations on the formation and evolution of merging compact-object binaries and their imlications for the astrophysical interpretation of present and forthcoming gravitational-wave sources.

In this thesis, we have already started the process of implementing the new λ values on the SEVN population-synthesis code, but we had to focus on a preliminary optimization of the SEVN code which is preparatory for the implementation of our new prescriptions. We found that the SEVN code requires significant optimization to evolve large samples of objects with different initial parameters since such simulations require a significant amount of memory and time (see figure 4.2).

Thus, we optimized SEVN to run very large samples of binary systems in a reasonable amount of time and with low memory consumption. To do that, we parallelized the SEVN code on both single computing nodes (through OpenMP) and multi-node supercomputers (through MPI).

In order to mitigate the memory requirements of the computing device, we implemented

a new method which we refer to as adaptive data loading. Adaptive loading divides the entire initial set of objects into chunks of sufficient size to avoid filling the system's available memory.

We also tested our parallel implementations on the Ulysses supercomputing cluster at SISSA. We used the OpenMP interface to speed up and optimize simulations on a single node and achieved a maximum speed-up of 10x. We used the MPI interface to scale computations across multiple compute nodes and improve the speed-up. On a single node, we got a speed-up of 30x with only MPI.

However, a large number of MPI processes on one node significantly increase memory requirements. Therefore, we used hybrid parallelization to take full advantage of OpenMP and MPI parallelization. As a result, we found that, on the Ulysses supercomputing cluster, the best hybrid combination for one node is 2 MPI processes per socket, and the number of threads is equal to the number of cores on one socket. This combination provides approximately 25x speed-up per compute node and minimal memory usage. We also performed MPI, and hybrid parallelization on multiple compute nodes. On 4 Ulysses compute nodes, with pure MPI, we get a speed-up of about 100x. With hybrid parallelization, we get a speed-up of about 75x.

Our main task of parallelization and code optimization is to evolve with SEVN large statistical samples of binaries, which may contain up to 10^9 objects. However, in this case, we will likely meet another issue related to loading the input files containing all the initial conditions of all stars. The problem is that such files will be heavy and require a large amount of memory. Figure 5.1 shows the dependence of the size of files with initial data depending on the number of binary systems. From figure it is apparent that the `regular2` partition on Ulysses will not have enough memory to simulate all binaries, even using just one MPI process. Thus, in the future, we will need to modify the SEVN data-loading method to take into account this aspect.

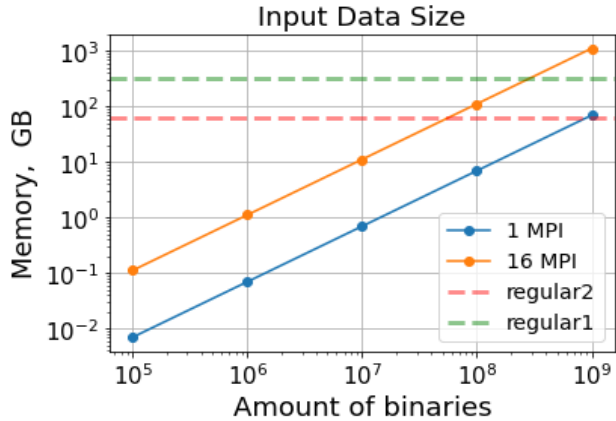A future optimization of the SEVN code will also be to port the code, or part of it,

Figure 5.1: The dependence of the size of files with initial data depending on the number of binary systems. The solid blue line shows the amount of memory needed for a single MPI process, while the orange solid line shows the amount of memory needed for 16 MPI processes. The horizontal dashed green line shows the maximum available memory on the `regular1` partition (or `long1`, etc.). The horizontal dashed red line shows the maximum available memory on the `regular2`.

on (multiple) graphics processing units (GPUs). The strategy might be very advantageous when SEVN is used in combination of massively GPU-parallel stellar dynamics codes (e.g., ISTEDDAS [339]), but it requires a profound restructuring of the SEVN code and the GPU-porting must be carefully investigated.

Data Availability

We have provided all the obtained binding energy parameters for hydrogen and helium stars for public use in the form of look-up tables. Tables containing the following data: the mass (M_i, in grams), radius (R_i, in centimeters), effective temperature (T_{eff}, in Kelvin), luminosity (L, in watts), the λ_g, λ_b and λ_h parameter of the star during stellar evolution.

We have also provided a detailed description of the fitting functions and their coefficients for public use. For each function, we pointed out the value of mean squared errors. The data available on the website github.com/NataNazar/Binding_energy_parameters

List of abbreviations

GR – General Relativity

GW - Gravitational Waves

BH – Black Hole

NS – Neutron Star

SN – Supernova

WR – Wolf-Rayet

WDs – White Dwarfs

BBHs – Binary Black Holes

BNSs – Binaries of Neutron Stars

sGRBs – short Gamma-Ray-Bursts

CO – carbon-oxygen

MS – Main Sequence

TAMS – The Terminal-Age Main Sequence

ZAMS – Zero-Age Main Sequence

HG – Hertzsprung Gap

GB – Giant Branch CHeB – Core-Helium Burning

AGB – Asymptotic Giant Branch

LIGO – Laser Interferometer Gravitational-wave Observatory

KAGRA – Kamioka Gravitational Wave Detector

ET – Einstein Telescope

CE – Cosmic Explorer

LISA – Laser Interferometer Space Antenna

SNR – Signal-to-Noise ratio

PISNe – Pair Instability Supernova

PPISNe – Pulsational Pair-Instability Supernova

EOS – Equation Of State

CHE - Chemical Homogeneous Evolution

CE – Common Envelope

CEE – Common Envelope Evolution

RLO – Roche-lobe overflow

HR diagram – Hertzsprung-Russell Diagramm

MSE – Mean Squared Error

BEC – the Bonn Evolutionary Code

MESA – the Modules for Experiments in Stellar Astrophysics

BPSs – Binary Population-Synthesis

SEVN – Stellar Evolution N-body

PARSEC – PAdova TRieste Stellar Evolution Code

SSE – Single Star Evolution

BSE – Binary-Star Evolution

MOBSE – Massive Objects in Binary Stellar Evolution

COSMIC – Compact Object Synthesis and Monte Carlo Investigation Code

BPASS – Binary Population and Spectral Synthesis code

RAM – Random-Access Memory

OpenMP – Open Multi-Processing

MPI – Message Passing Interface

API – Application Programming Interface

RAM – Random Access Memory

CPU – Central Processing Units

GPU – Graphics Processing Unit

NUMA – Non-Uniform Memory Access

VmRSS – Virtual Memory Resident Set Size

SLURM – Simple Linux Utility for Resource Management

List of Figures

89

List of Tables

Appendix A

Optimization of the SEVN code

A.1 OpenMP implementation

```cpp
int evolve_list(..., std::vector<std::unique_ptr<System>>& systems, ..., int
    Nevolve=-1){

    if (Nevolve==-1) Nevolve=systems.size();

    unsigned Nfailed=0;


    #pragma omp parallel num_threads(sevnio.nthreads) reduction(+: Nfailed)

    {

        long int omp_start = sevnomp->get_start(Nevolve);

        long int omp_end = sevnomp->get_end(Nevolve);

        for (long int i = omp_start; i < omp_end; i++) {


            T_BEGIN("Binary")

            /****** EVOLVE ******/

            if((*evolve_function)(systems[i])==EXIT_FAILURE)

                Nfailed++;

            T_END("Binary")
```

```
            }

            sevnomp->set_completed();

        }

        return Nfailed;

    }
```

```cpp
class treads_class{
  public:
    unsigned int threads_tot;
    treads_class(int num_threads) : threads_tot(num_threads){}


    long int get_start(int Nevolve);
    long int get_end(int Nevolve);
};
long int treads_class::get_start(int Nevolve) {
    long int bin_per_thread = (long int) (std::ceil(Nevolve/(double)
        threads_tot));
    return(omp_get_thread_num()*bin_per_thread);


}
long int treads_class::get_end(int Nevolve) {
    long int bin_per_thread = (long int) (std::ceil(Nevolve/(double)
        threads_tot));
    return(std::min(bin_per_thread*(omp_get_thread_num() + 1), (long int)
        Nevolve));
}
```

A.2   MPI implementation

```cpp
MPI_Init(&argc, &argv);                     // Initialization of MPI
/*

   ...

*/
long Nchunk = adapt_evolve_chunk<T>(&sevnio); // Calculate the adaptive chunk
    size that fits perfectly into the available memory of the actual device.
int numprocs;
MPI_Comm_size(MPI_COMM_WORLD, &numprocs);   // Get the number of processes in
    MPI_COMM_WORLD
int procid;
MPI_Comm_rank(MPI_COMM_WORLD, &procid);     // Get the rank of this process in
    MPI_COMM_WORLD


Nchunk = Nchunk/numprocs;
std::vector<std::unique_ptr<System>> systems; // Preliminary assignment
long Ntot = sevnio.STARS_MATRIX.size();     // Max size
long Tot_binaries = Ntot;
systems.reserve(Nchunk);                    //Reserve space for systems
unsigned int Ndone=0;
size_t current_idx=0;
int Ntodo=0;
int Nfailed=0;


unsigned int partition =std::ceil((double) Ntot /(double) numprocs);
// Calculation size of partition
Ntot = partition;                           // Redefining the Ntot for each MPI
    process
```

```cpp
current_idx = procid*partition;

Ntot = current_idx + Ntot > Tot_binaries ? Tot_binaries - current_idx: Ntot;

while (Ndone<Ntot){

    //Assign Ntodo

    Ntodo = current_idx + Ntodo > Tot_binaries ? Tot_binaries - current_idx :

        Ntot-Ndone;

    Ntodo = std::min(Ntot-Ndone, Nchunk);




    sevnomp.set_offset(current_idx);        //Fill vector

    T_BEGIN("EmplaceBack")

    for (size_t i = 0; i < (size_t) Ntodo; i++) {

        try{

            systems.emplace_back(new T(&sevnio, sevnio.STARS_MATRIX[current_idx],

                current_idx));

        }

        catch(sevnstd::sevnio_error& e){ //sevnio error contains initialisation

            errors

            sevnio.print_failed_initilisation_summary(current_idx);

            sevnlog.error("Failed initilisation for System with

                ID="+utilities::n2s(current_idx,__FILE__,__LINE__)+

                " with

                    message:\n"+e.what(),__FILE__,__LINE__,sevnio.svpar.get_bool("initerror_stop'

        }

        current_idx++;

    }

    T_END("EmplaceBack")

    //Evolve and update Nfailed
```

```
    Nfailed+=evolve_list(evolve_function, systems, sevnio, &sevnomp, Ntodo);

    //Clear

    systems.clear();


    //Update Ndone

    Ndone+=Ntodo;
}
/*

    ...

*/
MPI_Finalize();
```

Bibliography

[1] A. Einstein, "Näherungsweise Integration der Feldgleichungen der Gravitation," Sitzungsberichte der Königlich Preussischen Akademie der Wissenschaften, pp. 688–696, Jan. 1916.

[2] ——, "Über Gravitationswellen," Sitzungsberichte der Königlich Preussischen Akademie der Wissenschaften, pp. 154–167, Jan. 1918.

[3] ——, "Zur allgemeinen Relativitätstheorie," Sitzungsberichte der Königlich Preussischen Akademie der Wissenschaften, pp. 778–786, Jan. 1915.

[4] ——, "Die Grundlage der allgemeinen Relativitätstheorie," Annalen der Physik, vol. 354, no. 7, pp. 769–822, Jan. 1916.

[5] D. Kennefick, Traveling at the Speed of Thought. Princeton: Princeton University Press, 2016.
[Online]. Available: https://doi.org/10.1515/9781400882748

[6] J. Cervantes-Cota, S. Galindo-Uribarri, and G. Smoot, "A brief history of gravitational waves," Universe, vol. 2, no. 3, p. 22, sep 2016.
[Online]. Available: https://doi.org/10.3390%2Funiverse2030022

[7] E. Albert, The Collected Papers of Albert Einstein, Volume 8: The Berlin Years: Correspondence, 1914–1918, 1914-1918.
[Online]. Available: https://einsteinpapers.press.princeton.edu/vol8-trans/

[8] E. Albert and B. Max, The Born-Einstein Letters. Friendship, Politics and Physics in Uncertain Times. London, UK: Macmillan, 2005.

[9] B. Haskell, N. Andersson et al., "Gravitational waves from rapidly rotating neutron stars," in Gravitational Wave Astrophysics. Springer International Publishing, nov 2014, pp. 85–102.
[Online]. Available: https://doi.org/10.1007%2F978-3-319-10488-1_8

[10] L. Bildsten, "Gravitational Radiation and Rotation of Accreting Neutron Stars," , vol. 501, no. 1, pp. L89–L93, Jul. 1998.

[11] C. Horowitz and K. Kadau, "Breaking strain of neutron star crust and gravitational waves," Physical review letters, vol. 102, p. 191102, 06 2009.

[12] N. K. Johnson-McDaniel and B. J. Owen, "Maximum elastic deformations of relativistic stars," Phys. Rev. D, vol. 88, p. 044004, Aug 2013.
[Online]. Available: https://link.aps.org/doi/10.1103/PhysRevD.88.044004

[13] R. Ciolfi and L. Rezzolla, "Twisted-torus configurations with large toroidal magnetic fields in relativistic stars," Monthly Notices of the Royal Astronomical Society: Letters, vol. 435, no. 1, pp. L43–L47, 08 2013.
[Online]. Available: https://doi.org/10.1093/mnrasl/slt092

[14] B. Haskell, L. Samuelsson et al., "Modelling magnetically deformed neutron stars," , vol. 385, no. 1, pp. 531–542, Mar. 2008.

[15] D. J. B. Payne and A. Melatos, "Burial of the polar magnetic field of an accreting neutron star – I. Self-consistent analytic and numerical equilibria," Monthly Notices of the Royal Astronomical Society, vol. 351, no. 2, pp. 569–584, 06 2004.
[Online]. Available: https://doi.org/10.1111/j.1365-2966.2004.07798.x

[16] M. Priymak, A. Melatos, and D. J. B. Payne, "Quadrupole moment of a magnetically confined mountain on an accreting neutron star: effect of the equation of state," Monthly Notices of the Royal Astronomical Society, vol. 417, no. 4, pp. 2696–2713, sep 2011.

[Online]. Available: https://doi.org/10.1111%2Fj.1365-2966.2011.19431.x

[17] A. Melatos and D. J. B. Payne, "Gravitational radiation from an accreting millisecond pulsar with a magnetically confined mountain," The Astrophysical Journal, vol. 623, no. 2, p. 1044, apr 2005.

[Online]. Available: https://dx.doi.org/10.1086/428600

[18] J. W. Murphy, C. D. Ott, and A. Burrows, "A model for gravitational wave emission from neutrino-driven core-collapse supernovae," The Astrophysical Journal, vol. 707, no. 2, p. 1173, dec 2009.

[Online]. Available: https://dx.doi.org/10.1088/0004-637X/707/2/1173

[19] B. Müller, H.-T. Janka, and A. Marek, "A new multi-dimensional general relativistic neutrino hydrodynamics code of core-collapse supernovae. iii. gravitational wave signals from supernova explosion models," The Astrophysical Journal, vol. 766, no. 1, p. 43, mar 2013.

[Online]. Available: https://dx.doi.org/10.1088/0004-637X/766/1/43

[20] C. D. Ott, E. Abdikamalov et al., "General-relativistic Simulations of Three-dimensional Core-collapse Supernovae," , vol. 768, no. 2, p. 115, May 2013.

[21] P. Cerdá -Durán, N. DeBrye et al., "GRAVITATIONAL WAVE SIGNATURES IN BLACK HOLE FORMING CORE COLLAPSE," The Astrophysical Journal, vol. 779, no. 2, p. L18, dec 2013.

[Online]. Available: https://doi.org/10.1088%2F2041-8205%2F779%2F2%2Fl18

[22] K. N. Yakunin, A. Mezzacappa et al., "Gravitational wave signatures of ab initio

two-dimensional core collapse supernova explosion models for $12 - -25$ m$_\odot$ stars,"
Phys. Rev. D, vol. 92, p. 084040, Oct 2015.
[Online]. Available: https://link.aps.org/doi/10.1103/PhysRevD.92.084040

[23] T. Kuroda, K. Kotake, and T. Takiwaki, "A new gravitational-wave signature
from standing accretion shock instability in supernovae," The Astrophysical Journal
Letters, vol. 829, no. 1, p. L14, sep 2016.
[Online]. Available: https://dx.doi.org/10.3847/2041-8205/829/1/L14

[24] H. Andresen, B. Müller et al., "Gravitational wave signals from 3D neutrino
hydrodynamics simulations of core-collapse supernovae," Monthly Notices of the
Royal Astronomical Society, vol. 468, no. 2, pp. 2032–2051, 03 2017.
[Online]. Available: https://doi.org/10.1093/mnras/stx618

[25] S. Richers, C. D. Ott et al., "Equation of state effects on gravitational waves from
rotating core collapse," Phys. Rev. D, vol. 95, p. 063019, Mar 2017.
[Online]. Available: https://link.aps.org/doi/10.1103/PhysRevD.95.063019

[26] T. Takiwaki and K. Kotake, "Anisotropic emission of neutrino and gravitational-wave
signals from rapidly rotating core-collapse supernovae," , vol. 475, no. 1, pp. L91–L95,
Mar. 2018.

[27] E. P. O'Connor and S. M. Couch, "Exploring fundamentally three-dimensional
phenomena in high-fidelity simulations of core-collapse supernovae," The Astrophysical
Journal, vol. 865, no. 2, p. 81, sep 2018.
[Online]. Available: https://dx.doi.org/10.3847/1538-4357/aadcf7

[28] D. Radice, V. Morozova et al., "Characterizing the gravitational wave signal from
core-collapse supernovae," The Astrophysical Journal Letters, vol. 876, no. 1, p. L9,
apr 2019.
[Online]. Available: https://dx.doi.org/10.3847/2041-8213/ab191a

[29] D. Vartanyan, A. Burrows, and D. Radice, "Temporal and angular variations of 3D core-collapse supernova emissions and their physical correlations," <u>Monthly Notices of the Royal Astronomical Society</u>, vol. 489, no. 2, pp. 2227–2246, 08 2019. [Online]. Available: https://doi.org/10.1093/mnras/stz2307

[30] J. Powell and B. Müller, "Three-dimensional core-collapse supernova simulations of massive and rotating progenitors," , vol. 494, no. 4, pp. 4665–4675, Jun. 2020.

[31] O. E. Andersen, S. Zha <u>et al.</u>, "Equation-of-state dependence of gravitational waves in core-collapse supernovae," <u>The Astrophysical Journal</u>, vol. 923, no. 2, p. 201, dec 2021. [Online]. Available: https://doi.org/10.3847%2F1538-4357%2Fac294c

[32] M. A. Pajkos, M. L. Warren <u>et al.</u>, "Determining the structure of rotating massive stellar cores with gravitational waves," <u>The Astrophysical Journal</u>, vol. 914, no. 2, p. 80, jun 2021. [Online]. Available: https://dx.doi.org/10.3847/1538-4357/abfb65

[33] S. Shibagaki, T. Kuroda <u>et al.</u>, "Characteristic Time Variability of Gravitational-Wave and Neutrino Signals from Three-dimensional Simulations of Non-Rotating and Rapidly Rotating Stellar Core-Collapse," <u>Mon. Not. Roy. Astron. Soc.</u>, vol. 502, no. 2, pp. 3066–3084, 2021.

[34] S. Khlebnikov and I. Tkachev, "Relic gravitational waves produced after preheating," <u>Physical Review D</u>, vol. 56, no. 2, pp. 653–660, jul 1997. [Online]. Available: https://doi.org/10.1103%2Fphysrevd.56.653

[35] R. Easther and E. A. Lim, "Stochastic gravitational wave production after inflation," <u>Journal of Cosmology and Astroparticle Physics</u>, vol. 2006, no. 04, pp. 010–010, apr 2006. [Online]. Available: https://doi.org/10.1088%2F1475-7516%2F2006%2F04%2F010

[36] J. Garcí a-Bellido and D. G. Figueroa, "Stochastic background of gravitational waves from hybrid preheating," Physical Review Letters, vol. 98, no. 6, feb 2007. [Online]. Available: https://doi.org/10.1103%2Fphysrevlett.98.061302

[37] J.-F. Dufaux, A. Bergman et al., "Theory and numerics of gravitational waves from preheating after inflation," Physical Review D, vol. 76, no. 12, dec 2007. [Online]. Available: https://doi.org/10.1103%2Fphysrevd.76.123517

[38] D. G. Figueroa, M. Hindmarsh, and J. Urrestilla, "Exact scale-invariant background of gravitational waves from cosmic defects," Physical Review Letters, vol. 110, no. 10, mar 2013. [Online]. Available: https://doi.org/10.1103%2Fphysrevlett.110.101302

[39] D. G. Figueroa, "Imprints of the standard model in the sky: Gravitational waves from the decay of the higgs after inflation," 2014. [Online]. Available: https://arxiv.org/abs/1402.1345

[40] D. G. Figueroa, J. Garcí a-Bellido, and F. Torrentí, "Gravitational wave production from the decay of the standard model higgs field after inflation," Physical Review D, vol. 93, no. 10, may 2016. [Online]. Available: https://doi.org/10.1103%2Fphysrevd.93.103521

[41] S. Antusch, F. Cefalà , and S. Orani, "Gravitational waves from oscillons after inflation," Physical Review Letters, vol. 118, no. 1, jan 2017. [Online]. Available: https://doi.org/10.1103%2Fphysrevlett.118.011303

[42] A. Kosowsky, M. S. Turner, and R. Watkins, "Gravitational radiation from colliding vacuum bubbles," Phys. Rev. D, vol. 45, pp. 4514–4535, Jun 1992. [Online]. Available: https://link.aps.org/doi/10.1103/PhysRevD.45.4514

[43] M. Kamionkowski, A. Kosowsky, and M. S. Turner, "Gravitational radiation from

first-order phase transitions," Physical Review D, vol. 49, no. 6, pp. 2837–2851, mar 1994.
[Online]. Available: https://doi.org/10.1103%2Fphysrevd.49.2837

[44] C. Caprini, R. Durrer, and G. Servant, "Gravitational wave generation from bubble collisions in first-order phase transitions: An analytic approach," Physical Review D, vol. 77, no. 12, jun 2008.
[Online]. Available: https://doi.org/10.1103%2Fphysrevd.77.124015

[45] C. Caprini, R. Durrer et al., "General properties of the gravitational wave spectrum from phase transitions," Physical Review D, vol. 79, no. 8, apr 2009.
[Online]. Available: https://doi.org/10.1103%2Fphysrevd.79.083519

[46] C. Caprini, M. Hindmarsh et al., "Science with the space-based interferometer eLISA. II: gravitational waves from cosmological phase transitions," Journal of Cosmology and Astroparticle Physics, vol. 2016, no. 04, pp. 001–001, apr 2016.
[Online]. Available: https://doi.org/10.1088%2F1475-7516%2F2016%2F04%2F001

[47] D. J. Weir, "Revisiting the envelope approximation: Gravitational waves from bubble collisions," Physical Review D, vol. 93, no. 12, jun 2016.
[Online]. Available: https://doi.org/10.1103%2Fphysrevd.93.124037

[48] T. Vachaspati and A. Vilenkin, "Gravitational radiation from cosmic strings," Phys. Rev. D, vol. 31, pp. 3052–3058, Jun 1985.
[Online]. Available: https://link.aps.org/doi/10.1103/PhysRevD.31.3052

[49] P. Biné truy, A. Bohé et al., "Cosmological backgrounds of gravitational waves and eLISA/NGO: phase transitions, cosmic strings and other sources," Journal of Cosmology and Astroparticle Physics, vol. 2012, no. 06, pp. 027–027, jun 2012.
[Online]. Available: https://doi.org/10.1088%2F1475-7516%2F2012%2F06%2F027

[50] S. A. Sanidas, R. A. Battye, and B. W. Stappers, "Constraints on cosmic string tension imposed by the limit on the stochastic gravitational wave background from the european pulsar timing array," Physical Review D, vol. 85, no. 12, jun 2012. [Online]. Available: https://doi.org/10.1103%2Fphysrevd.85.122003

[51] J. Garcí a-Bellido, A. Linde, and D. Wands, "Density perturbations and black hole formation in hybrid inflation," Physical Review D, vol. 54, no. 10, pp. 6040–6058, nov 1996. [Online]. Available: https://doi.org/10.1103%2Fphysrevd.54.6040

[52] S. Clesse and J. García-Bellido, "Detecting the gravitational wave background from primordial black hole dark matter," 2016. [Online]. Available: https://arxiv.org/abs/1610.08479

[53] S. Clesse and J. García-Bellido, "The clustering of massive primordial black holes as dark matter: Measuring their mass distribution with advanced LIGO," Physics of the Dark Universe, vol. 15, pp. 142–147, mar 2017. [Online]. Available: https://doi.org/10.1016%2Fj.dark.2016.10.002

[54] S. Bird, I. Cholis et al., "Did LIGO detect dark matter?" Physical Review Letters, vol. 116, no. 20, may 2016. [Online]. Available: https://doi.org/10.1103%2Fphysrevlett.116.201301

[55] I. Cholis, E. D. Kovetz et al., "Orbital eccentricities in primordial black hole binaries," Physical Review D, vol. 94, no. 8, oct 2016. [Online]. Available: https://doi.org/10.1103%2Fphysrevd.94.084013

[56] R. Dong, W. H. Kinney, and D. Stojkovic, "Gravitational wave production by hawking radiation from rotating primordial black holes," Journal of Cosmology and Astroparticle Physics, vol. 2016, no. 10, pp. 034–034, oct 2016. [Online]. Available: https://doi.org/10.1088%2F1475-7516%2F2016%2F10%2F034

[57] K. S. Thorne, "Probing black holes and relativistic stars with gravitational waves," 1997.

[Online]. Available: https://arxiv.org/abs/gr-qc/9706079

[58] K. Schwarzschild, "Über das Gravitationsfeld eines Massenpunktes nach der Einsteinschen Theorie," Sitzungsberichte der Königlich Preussischen Akademie der Wissenschaften, pp. 189–196, Jan. 1916.

[59] ——, "Über das Gravitationsfeld einer Kugel aus inkompressibler Flüssigkeit nach der Einsteinschen Theorie," in Sitzungsberichte der Königlich Preussischen Akademie der Wissenschaften zu Berlin, Mar. 1916, pp. 424–434.

[60] H. Goldstein, Classical Mechanics.   Addison-Wesley, 1980.

[61] L. D. Landau and E. M. Lifshitz, Mechanics, Third Edition: Volume 1 (Course of Theoretical Physics), 3rd ed.   Butterworth-Heinemann, Jan. 1976.
[Online]. Available: http://www.worldcat.org/isbn/0750628960

[62] D. G. Blair, The detection of gravitational waves / edited by David G. Blair, digitally printed 1st pbk. version. ed.   Cambridge University Press Cambridge ; Melbourne, 2005.
[Online]. Available: http://www.loc.gov/catdir/enhancements/fy0659/2006274605-t.html

[63] R. Rubenzahl, "Gravitational Wave Radiation by Binary Black Holes," PHY, p. 413, 2017.
[Online]. Available: https://rrubenza.github.io/project/p413_gws/RR_PHY413_GW_Paper.pdf

[64] P. C. Peters and J. Mathews, "Gravitational radiation from point masses in a Keplerian orbit," Phys. Rev., vol. 131, pp. 435–439, 1963.

[65] B. P. Abbott, R. Abbott et al., "Prospects for observing and localizing gravitational-wave transients with Advanced LIGO, Advanced Virgo and KAGRA," Living Reviews in Relativity, vol. 23, no. 1, p. 3, Sep. 2020.

[66] A. A. Michelson and E. W. Morley, "On the relative motion of the earth and the luminiferous ether," American Journal of Science, vol. s3-34, no. 203, pp. 333–345, 1887.
[Online]. Available: https://www.ajsonline.org/content/s3-34/203/333

[67] B. P. Abbott, R. Abbott et al., vol. 818, no. 2, p. L22, feb 2016.
[Online]. Available: https://dx.doi.org/10.3847/2041-8205/818/2/L22

[68] P. Hariharan, "Preface to the second edition," in Basics of Interferometry (Second Edition), second edition ed., P. Hariharan and P. Hariharan, Eds. Burlington: Academic Press, 2007, pp. xix–xx.
[Online]. Available: https://www.sciencedirect.com/science/article/pii/ B9780123735898500018

[69] LIGO Scientific Collaboration, J. Aasi et al., "Advanced LIGO," Classical and Quantum Gravity, vol. 32, no. 7, p. 074001, Apr. 2015.

[70] F. Acernese, M. Agathos et al., "Advanced virgo: a second-generation interferometric gravitational wave detector," Classical and Quantum Gravity, vol. 32, no. 2, p. 024001, Dec 2014.
[Online]. Available: http://dx.doi.org/10.1088/0264-9381/32/2/024001

[71] Y. Aso, Y. Michimura et al., "Interferometer design of the KAGRA gravitational wave detector," Phys. Rev. D, vol. 88, no. 4, p. 043007, 2013.

[72] KAGRA Collaboration, "Kagra: 2.5 generation interferometric gravitational wave detector," Nature Astronomy, vol. 3, no. 1, p. 35–40, Jan 2019.
[Online]. Available: http://dx.doi.org/10.1038/s41550-018-0658-y

[73] C. S. UNNIKRISHNAN, "IndIGO AND LIGO-INDIA: SCOPE AND PLANS FOR GRAVITATIONAL WAVE RESEARCH AND PRECISION METROLOGY IN INDIA," International Journal of Modern Physics D, vol. 22, no. 01, p. 1341010, jan 2013.

[Online]. Available: https://doi.org/10.1142%2Fs0218271813410101

[74] S. Fairhurst, "Localization of transient gravitational wave sources: beyond triangulation," Classical and Quantum Gravity, vol. 35, no. 10, p. 105002, apr 2018. [Online]. Available: https://dx.doi.org/10.1088/1361-6382/aab675

[75] M. Punturo, M. Abernathy et al., "The einstein telescope: a third-generation gravitational wave observatory," Classical and Quantum Gravity, vol. 27, no. 19, p. 194002, sep 2010.

[Online]. Available: https://dx.doi.org/10.1088/0264-9381/27/19/194002

[76] B. P. Abbott, R. Abbott et al., "Exploring the sensitivity of next generation gravitational wave detectors," Classical and Quantum Gravity, vol. 34, no. 4, p. 044001, Feb. 2017.

[77] R. X. Adhikari, K. Arai et al., "A cryogenic silicon interferometer for gravitational-wave detection," Classical and Quantum Gravity, vol. 37, no. 16, p. 165003, jul 2020.

[Online]. Available: https://doi.org/10.1088%2F1361-6382%2Fab9143

[78] N. Cornish and T. Robson, "Galactic binary science with the new LISA design," Journal of Physics: Conference Series, vol. 840, p. 012024, may 2017.

[Online]. Available: https://doi.org/10.1088%2F1742-6596%2F840%2F1%2F012024

[79] P. Amaro-Seoane, H. Audley et al., "Laser interferometer space antenna," 2017.

[80] A. Klein, E. Barausse et al., "Science with the space-based interferometer eLISA: Supermassive black hole binaries," Physical Review D, vol. 93, no. 2, jan 2016.

[Online]. Available: https://doi.org/10.1103%2Fphysrevd.93.024003

[81] É . É. Flanagan and S. A. Hughes, "Measuring gravitational waves from binary black hole coalescences. i. signal to noise for inspiral, merger, and ringdown," <u>Physical Review D</u>, vol. 57, no. 8, pp. 4535–4565, apr 1998.
[Online]. Available: https://doi.org/10.1103%2Fphysrevd.57.4535

[82] A. Sesana, "Prospects for Multiband Gravitational-Wave Astronomy after GW150914," , vol. 116, no. 23, p. 231102, Jun. 2016.

[83] P. Amaro-Seoane, J. R. Gair <u>et al.</u>, "Intermediate and extreme mass-ratio inspirals—astrophysics, science applications and detection using LISA," <u>Classical and Quantum Gravity</u>, vol. 24, no. 17, pp. R113–R169, aug 2007.
[Online]. Available: https://doi.org/10.1088%2F0264-9381%2F24%2F17%2Fr01

[84] C. P. L. Berry and J. R. Gair, "Expectations for extreme-mass-ratio bursts from the galactic centre," <u>Monthly Notices of the Royal Astronomical Society</u>, vol. 435, no. 4, pp. 3521–3540, sep 2013.
[Online]. Available: https://doi.org/10.1093%2Fmnras%2Fstt1543

[85] D. R. Lorimer and M. Kramer, <u>Handbook of Pulsar Astronomy</u>, 2004, vol. 4.

[86] M. A. McLaughlin, "The North American Nanohertz Observatory for Gravitational Waves," <u>Classical and Quantum Gravity</u>, vol. 30, no. 22, p. 224008, Nov. 2013.

[87] M. Kramer and D. J. Champion, "The European Pulsar Timing Array and the Large European Array for Pulsars," <u>Classical and Quantum Gravity</u>, vol. 30, no. 22, p. 224009, Nov. 2013.

[88] R. N. Manchester, G. Hobbs <u>et al.</u>, "The Parkes Pulsar Timing Array Project," , vol. 30, p. e017, Jan. 2013.

[89] J. P. W. Verbiest, L. Lentati et al., "The International Pulsar Timing Array: First data release,", vol. 458, no. 2, pp. 1267–1288, May 2016.

[90] M. V. Sazhin, "Opportunities for detecting ultralong gravitational waves,", vol. 22, pp. 36–38, Feb. 1978.

[91] S. Detweiler, "Pulsar timing measurements and the search for gravitational waves,", vol. 234, pp. 1100–1104, Dec. 1979.

[92] J. B. Wang, W. A. Coles et al., "Comparison of pulsar positions from timing and very long baseline astrometry," Monthly Notices of the Royal Astronomical Society, vol. 469, no. 1, pp. 425–434, apr 2017.
[Online]. Available: https://doi.org/10.1093%2Fmnras%2Fstx837

[93] L. Lentati, M. Kerr et al., "Wide-band profile domain pulsar timing analysis,", vol. 466, no. 3, pp. 3706–3727, Apr. 2017.

[94] D. R. Madison, X. J. Zhu et al., "Versatile directional searches for gravitational waves with Pulsar Timing Arrays,", vol. 455, no. 4, pp. 3662–3673, Feb. 2016.

[95] P. D. Lasky, C. M. F. Mingarelli et al., "Gravitational-Wave Cosmology across 29 Decades in Frequency," Physical Review X, vol. 6, no. 1, p. 011035, Jan. 2016.

[96] R. Smits, C. G. Bassa et al., "The beamformer and correlator for the Large European Array for Pulsars," Astronomy and Computing, vol. 19, pp. 66–74, Apr. 2017.

[97] J. Antoniadis, Z. Arzoumanian et al., "The International Pulsar Timing Array second data release: Search for an isotropic gravitational wave background," Monthly Notices of the Royal Astronomical Society, vol. 510, no. 4, pp. 4873–4887, 01 2022.
[Online]. Available: https://doi.org/10.1093/mnras/stab3418

[98] S. Chen, R. N. Caballero et al., "Common-red-signal analysis with 24-yr high-precision timing of the European Pulsar Timing Array: inferences in the stochastic

gravitational-wave background search," <u>Monthly Notices of the Royal Astronomical Society</u>, vol. 508, no. 4, pp. 4970–4993, 10 2021. [Online]. Available: https://doi.org/10.1093/mnras/stab2833

[99] H. M. Wahl, M. A. McLaughlin <u>et al.</u>, "The NANOGrav 12.5 yr Data Set: Polarimetry and Faraday Rotation Measures from Observations of Millisecond Pulsars with the Green Bank Telescope," , vol. 926, no. 2, p. 168, Feb. 2022.

[100] Z. Arzoumanian, P. T. Baker <u>et al.</u>, "The NANOGrav 12.5-year Data Set: Search for Non-Einsteinian Polarization Modes in the Gravitational-wave Background," , vol. 923, no. 2, p. L22, Dec. 2021.

[101] J. E. Turner, M. A. McLaughlin <u>et al.</u>, "The NANOGrav 12.5 Year Data Set: Monitoring Interstellar Scattering Delays," , vol. 917, no. 1, p. 10, Aug. 2021.

[102] M. F. Alam, Z. Arzoumanian <u>et al.</u>, "The NANOGrav 12.5 yr Data Set: Observations and Narrowband Timing of 47 Millisecond Pulsars," , vol. 252, no. 1, p. 4, Jan. 2021.

[103] R. N. Manchester and IPTA, "The International Pulsar Timing Array," <u>Classical and Quantum Gravity</u>, vol. 30, no. 22, p. 224010, Nov. 2013.

[104] B. P. Abbott, R. Abbott <u>et al.</u>, "Observation of gravitational waves from a binary black hole merger."

[105] B. Abbott, R. Abbott <u>et al.</u>, "GWTC-1: A gravitational-wave transient catalog of compact binary mergers observed by LIGO and virgo during the first and second observing runs," <u>Physical Review X</u>, vol. 9, no. 3, sep 2019. [Online]. Available: https://doi.org/10.1103%2Fphysrevx.9.031040

[106] B. P. Abbott, R. Abbott <u>et al.</u>, "Gwtc-1: A gravitational-wave transient catalog of compact binary mergers observed by ligo and virgo during the first and second observing runs," <u>Physical Review X</u>, vol. 9, no. 3, Sep 2019.

[Online]. Available: http://dx.doi.org/10.1103/PhysRevX.9.031040

[107] The LIGO Scientific Collaboration and the Virgo Collaboration, "Gwtc-2: Compact binary coalescences observed by ligo and virgo during the first half of the third observing run," Physical Review X, vol. 11, no. 2, Jun 2021.
[Online]. Available: http://dx.doi.org/10.1103/PhysRevX.11.021053

[108] ——, "Gwtc-2.1: Deep extended catalog of compact binary coalescences observed by ligo and virgo during the first half of the third observing run," 2021.

[109] The LIGO Scientific Collaboration and the Virgo Collaboration and the KAGRA Collaboration, "Gwtc-3: Compact binary coalescences observed by ligo and virgo during the second part of the third observing run," 2021.

[110] R. Abbott, T. D. Abbott et al., "Gw190814: Gravitational waves from the coalescence of a 23 solar mass black hole with a 2.6 solar mass compact object," The Astrophysical Journal Letters, vol. 896, no. 2, p. L44, jun 2020.
[Online]. Available: https://dx.doi.org/10.3847/2041-8213/ab960f

[111] LIGO Scientific Collaboration and Virgo Collaboration, "Gw190521: A binary black hole merger with a total mass of 150 $M_{\odot}$," Phys. Rev. Lett., vol. 125, p. 101102, Sep 2020.
[Online]. Available: https://link.aps.org/doi/10.1103/PhysRevLett.125.101102

[112] R. Abbott, T. D. Abbott et al., "Properties and astrophysical implications of the 150 m binary black hole merger gw190521," The Astrophysical Journal Letters, vol. 900, no. 1, p. L13, sep 2020.
[Online]. Available: https://dx.doi.org/10.3847/2041-8213/aba493

[113] I. Romero-Shaw, P. D. Lasky et al., "Gw190521: Orbital eccentricity and signatures of dynamical formation in a binary black hole merger signal," The Astrophysical Journal Letters, vol. 903, no. 1, p. L5, oct 2020.

[Online]. Available: https://dx.doi.org/10.3847/2041-8213/abbe26

[114] V. Gayathri, J. Healy et al., "Eccentricity estimate for black hole mergers with numerical relativity simulations," 2020.
[Online]. Available: https://arxiv.org/abs/2009.05461

[115] A. M. Holgado, A. Ortega, and C. L. Rodriguez, "Dynamical formation scenarios for gw190521 and prospects for decihertz gravitational-wave astronomy with gw190521-like binaries," The Astrophysical Journal Letters, vol. 909, no. 2, p. L24, mar 2021.
[Online]. Available: https://dx.doi.org/10.3847/2041-8213/abe7f5

[116] B. P. Abbott, R. Abbott et al., "Gw170817: Observation of gravitational waves from a binary neutron star inspiral," Phys. Rev. Lett., vol. 119, p. 161101, Oct 2017.
[Online]. Available: https://link.aps.org/doi/10.1103/PhysRevLett.119.161101

[117] M. Spera, A. A. Trani, and M. Mencagli, "Compact binary coalescences: Astrophysical processes and lessons learned," Galaxies, vol. 10, no. 4, p. 76, jun 2022.
[Online]. Available: https://doi.org/10.3390%2Fgalaxies10040076

[118] M. Spera, M. Mapelli et al., "Merging black hole binaries with the SEVN code," Monthly Notices of the Royal Astronomical Society, vol. 485, no. 1, pp. 889–907, feb 2019.
[Online]. Available: https://doi.org/10.1093%2Fmnras%2Fstz359

[119] M. Spera, M. Mapelli, and A. Bressan, "The mass spectrum of compact remnants from the parsec stellar evolution tracks," Monthly Notices of the Royal Astronomical Society, vol. 451, no. 4, pp. 4086–4103, 06 2015.
[Online]. Available: https://doi.org/10.1093/mnras/stv1161

[120] M. Spera and M. Mapelli, "Very massive stars, pair-instability supernovae and

intermediate-mass black holes with the sevn code," Monthly Notices of the Royal Astronomical Society, vol. 470, no. 4, pp. 4739–4749, 06 2017. [Online]. Available: https://doi.org/10.1093/mnras/stx1576

[121] A. Bressan, P. Marigo et al., "PARSEC: stellar tracks and isochrones with the PAdova and TRieste Stellar Evolution Code," , vol. 427, no. 1, pp. 127–145, Nov. 2012.

[122] Y. Chen, L. Girardi et al., "Improving PARSEC models for very low mass stars," , vol. 444, no. 3, pp. 2525–2543, Nov. 2014.

[123] J. Tang, A. Bressan et al., "New PARSEC evolutionary tracks of massive stars at low metallicity: testing canonical stellar evolution in nearby star-forming dwarf galaxies," , vol. 445, no. 4, pp. 4287–4305, Dec. 2014.

[124] J. Montalbán, A. Bressan et al., "PARSEC evolutionary tracks and isochrones including seismic properties," in Rediscovering Our Galaxy, C. Chiappini, I. Minchev et al., Eds., vol. 334, Aug. 2018, pp. 343–344.

[125] P. Marigo, L. Girardi et al., "A New Generation of PARSEC-COLIBRI Stellar Isochrones Including the TP-AGB Phase," , vol. 835, no. 1, p. 77, Jan. 2017.

[126] X. Fu, A. Bressan et al., "New PARSEC database of alpha enhanced stellar evolutionary tracks and isochrones for Gaia," IAU Focus Meeting, vol. 29B, pp. 144–146, Jan. 2016.

[127] A. S. Eddington, "On the Relation between the Masses and Luminosities of the Stars.: (Plate 8.)," Monthly Notices of the Royal Astronomical Society, vol. 84, no. 5, pp. 308–333, 03 1924. [Online]. Available: https://doi.org/10.1093/mnras/84.5.308

[128] S. E. Woosley, A. Heger, and T. A. Weaver, "The evolution and explosion of massive stars," Rev. Mod. Phys., vol. 74, pp. 1015–1071, Nov 2002.

[Online]. Available: https://link.aps.org/doi/10.1103/RevModPhys.74.1015

[129] S. J. Smartt, "Progenitors of Core-Collapse Supernovae," , vol. 47, no. 1, pp. 63–106, Sep. 2009.

[130] S. Horiuchi, J. F. Beacom et al., "The cosmic core-collapse supernova rate does not match the massive-star formation rate," The Astrophysical Journal, vol. 738, no. 2, p. 154, aug 2011.
[Online]. Available: https://dx.doi.org/10.1088/0004-637X/738/2/154

[131] S. J. Smartt, "Observational constraints on the progenitors of core-collapse supernovae: The case for missing high-mass stars," Publications of the Astronomical Society of Australia, vol. 32, p. e016, 2015.

[132] V. S. Aguirre, "Stellar evolution and modelling stars," in Asteroseismology and Exoplanets: Listening to the Stars and Searching for New Worlds, T. L. Campante, N. C. Santos, and M. J. P. F. G. Monteiro, Eds. Cham: Springer International Publishing, 2018, pp. 3–25.

[133] J. S. Vink, "Theory and Diagnostics of Hot Star Mass Loss," , vol. 60, pp. 203–246, Aug. 2022.

[134] H.-T. Janka, Neutrino-Driven Explosions. Cham: Springer International Publishing, 2017, pp. 1095–1150.
[Online]. Available: https://doi.org/10.1007/978-3-319-21846-5_109

[135] ——, "Explosion mechanisms of core-collapse supernovae," Annual Review of Nuclear and Particle Science, vol. 62, no. 1, pp. 407–451, 2012.
[Online]. Available: https://doi.org/10.1146/annurev-nucl-102711-094901

[136] A. Mezzacappa, E. Endeve et al., "Physical, numerical, and computational challenges of modeling neutrino transport in core-collapse supernovae," 2020.

[Online]. Available: https://arxiv.org/abs/2010.09013

[137] C. D. Bailyn, R. K. Jain et al., "The mass distribution of stellar black holes," The Astrophysical Journal, vol. 499, no. 1, p. 367, may 1998. [Online]. Available: https://dx.doi.org/10.1086/305614

[138] F. Özel, D. Psaltis et al., "The black hole mass distribution in the galaxy," The Astrophysical Journal, vol. 725, no. 2, p. 1918, dec 2010. [Online]. Available: https://dx.doi.org/10.1088/0004-637X/725/2/1918

[139] W. M. Farr, N. Sravan et al., "The mass distribution of stellar-mass black holes," The Astrophysical Journal, vol. 741, no. 2, p. 103, oct 2011. [Online]. Available: https://dx.doi.org/10.1088/0004-637X/741/2/103

[140] B. P. Abbott, R. Abbott et al., "Binary black hole population properties inferred from the first and second observing runs of advanced LIGO and advanced virgo," The Astrophysical Journal, vol. 882, no. 2, p. L24, sep 2019. [Online]. Available: https://doi.org/10.3847%2F2041-8213%2Fab3800

[141] F. Özel and P. Freire, "Masses, radii, and the equation of state of neutron stars," Annual Review of Astronomy and Astrophysics, vol. 54, no. 1, pp. 401–440, 2016. [Online]. Available: https://doi.org/10.1146/annurev-astro-081915-023322

[142] P. C. C. Freire, S. M. Ransom et al., "Eight new millisecond pulsars in ngc 6440 and ngc 6441," The Astrophysical Journal, vol. 675, no. 1, p. 670, mar 2008. [Online]. Available: https://dx.doi.org/10.1086/526338

[143] B. Margalit and B. D. Metzger, "Constraining the maximum mass of neutron stars from multi-messenger observations of gw170817," The Astrophysical Journal Letters, vol. 850, no. 2, p. L19, nov 2017. [Online]. Available: https://dx.doi.org/10.3847/2041-8213/aa991c

[144] L. Kreidberg, C. D. Bailyn et al., "Mass measurements of black holes in x-ray transients: Is there a mass gap?" The Astrophysical Journal, vol. 757, no. 1, p. 36, sep 2012.
[Online]. Available: https://dx.doi.org/10.1088/0004-637X/757/1/36

[145] T. B. Littenberg, B. Farr et al., "Neutron stars versus black holes: Probing the mass gap with ligo/virgo," The Astrophysical Journal Letters, vol. 807, no. 2, p. L24, jul 2015.
[Online]. Available: https://dx.doi.org/10.1088/2041-8205/807/2/L24

[146] I. Mandel, C.-J. Haster et al., "Distinguishing types of compact-object binaries using the gravitational-wave signatures of their mergers," Monthly Notices of the Royal Astronomical Society: Letters, vol. 450, no. 1, pp. L85–L89, 04 2015.
[Online]. Available: https://doi.org/10.1093/mnrasl/slv054

[147] E. D. Kovetz, I. Cholis et al., "Black hole mass function from gravitational wave measurements," Phys. Rev. D, vol. 95, p. 103010, May 2017.
[Online]. Available: https://link.aps.org/doi/10.1103/PhysRevD.95.103010

[148] I. Mandel, W. M. Farr et al., "Model-independent inference on compact-binary observations," Monthly Notices of the Royal Astronomical Society, vol. 465, no. 3, pp. 3254–3260, 11 2016.
[Online]. Available: https://doi.org/10.1093/mnras/stw2883

[149] C. L. Fryer, K. Belczynski et al., "Compact remnant mass function: Dependence on the explosion mechanism and metallicity," The Astrophysical Journal, vol. 749, no. 1, p. 91, mar 2012.
[Online]. Available: https://dx.doi.org/10.1088/0004-637X/749/1/91

[150] M. Safarzadeh, A. S. Hamers et al., "Formation and merging of mass gap black holes

in gravitational-wave merger events from wide hierarchical quadruple systems," The Astrophysical Journal, vol. 888, no. 1, p. L3, dec 2019. [Online]. Available: https://doi.org/10.3847%2F2041-8213%2Fab5dc8

[151] A. Heger and S. E. Woosley, "The nucleosynthetic signature of population iii," The Astrophysical Journal, vol. 567, no. 1, p. 532, mar 2002. [Online]. Available: https://dx.doi.org/10.1086/338487

[152] K. Belczynski, A. Heger et al., "The effect of pair-instability mass loss on black-hole mergers," , vol. 594, p. A97, Oct. 2016.

[153] S. E. Woosley, "Pulsational pair-instability supernovae," The Astrophysical Journal, vol. 836, no. 2, p. 244, feb 2017. [Online]. Available: https://doi.org/10.3847/1538-4357/836/2/244

[154] P. Marchant, M. Renzo et al., "Pulsational pair-instability supernovae in very close binaries," The Astrophysical Journal, vol. 882, no. 1, p. 36, aug 2019. [Online]. Available: https://doi.org/10.3847%2F1538-4357%2Fab3426

[155] S. E. Woosley, S. Blinnikov, and A. Heger, "Pulsational pair instability as an explanation for the most luminous supernovae," Nature, vol. 450, no. 7168, pp. 390–392, nov 2007. [Online]. Available: https://doi.org/10.1038%2Fnature06333

[156] W. A. Fowler and F. Hoyle, "Neutrino Processes and Pair Formation in Massive Stars and Supernovae." , vol. 9, p. 201, Dec. 1964.

[157] Z. Barkat, G. Rakavy, and N. Sack, "Dynamics of supernova explosion resulting from pair formation," Phys. Rev. Lett., vol. 18, pp. 379–381, Mar 1967. [Online]. Available: https://link.aps.org/doi/10.1103/PhysRevLett.18.379

[158] G. Rakavy and G. Shaviv, "Instabilities in Highly Evolved Stellar Models,", vol. 148, p. 803, Jun. 1967.

[159] C. L. Rodriguez, S. Chatterjee, and F. A. Rasio, "Binary black hole mergers from globular clusters: Masses, merger rates, and the impact of stellar evolution," Physical Review D, vol. 93, no. 8, Apr 2016.
[Online]. Available: http://dx.doi.org/10.1103/PhysRevD.93.084029

[160] A. Askar, M. Szkudlarek et al., "MOCCA-SURVEY Database - I. Coalescing binary black holes originating from globular clusters,", vol. 464, no. 1, pp. L36–L40, Jan. 2017.

[161] J. Samsing, "Eccentric black hole mergers forming in globular clusters,", vol. 97, no. 10, p. 103014, May 2018.

[162] C. L. Rodriguez, M. Zevin et al., "Black holes: The next generation—repeated mergers in dense star clusters and their gravitational-wave properties," Physical Review D, vol. 100, no. 4, Aug 2019.
[Online]. Available: http://dx.doi.org/10.1103/PhysRevD.100.043027

[163] M. Mapelli, "Astrophysics of stellar black holes," 2018.

[164] M. Arca-Sedda and A. Gualandris, "Gravitational wave sources from inspiralling globular clusters in the Galactic Centre and similar environments," Monthly Notices of the Royal Astronomical Society, vol. 477, no. 4, pp. 4423–4442, 04 2018.
[Online]. Available: https://doi.org/10.1093/mnras/sty922

[165] G. Fragione and B. Kocsis, "Black hole mergers from quadruples," Monthly Notices of the Royal Astronomical Society, vol. 486, no. 4, pp. 4781–4789, 05 2019.
[Online]. Available: https://doi.org/10.1093/mnras/stz1175

[166] F. Antonini and F. A. Rasio, "Merging Black Hole Binaries in Galactic Nuclei: Implications for Advanced-LIGO Detections," , vol. 831, no. 2, p. 187, Nov. 2016.

[167] N. C. Stone, B. D. Metzger, and Z. Haiman, "Assisted inspirals of stellar mass black holes embedded in AGN discs: solving the 'final au problem'," , vol. 464, no. 1, pp. 946–954, Jan. 2017.

[168] B. McKernan, K. S. Ford et al., "Constraining stellar-mass black hole mergers in agn disks detectable with ligo," The Astrophysical Journal, vol. 866, no. 1, p. 66, 2018.

[169] F. Antonini, S. Toonen, and A. S. Hamers, "Binary Black Hole Mergers from Field Triples: Properties, Rates, and the Impact of Stellar Evolution," , vol. 841, no. 2, p. 77, Jun. 2017.

[170] G. Fragione, E. Grishin et al., "Black hole and neutron star mergers in galactic nuclei," Monthly Notices of the Royal Astronomical Society, vol. 488, no. 1, pp. 47–63, 2019.

[171] R. F. Webbink, "Evolution of Helium White Dwarfs in Close Binaries," Monthly Notices of the Royal Astronomical Society, vol. 171, no. 3, pp. 555–568, 06 1975. [Online]. Available: https://doi.org/10.1093/mnras/171.3.555

[172] B. Paczynski, "Common Envelope Binaries," in Structure and Evolution of Close Binary Systems, P. Eggleton, S. Mitton, and J. Whelan, Eds., vol. 73, Jan. 1976, p. 75.

[173] E. P. J. van den Heuvel, "Late Stages of Close Binary Systems," in Structure and Evolution of Close Binary Systems, P. Eggleton, S. Mitton, and J. Whelan, Eds., vol. 73, Jan. 1976, p. 35.

[174] P. Hut, "Tidal evolution in close binary systems." , vol. 99, pp. 126–140, Jun. 1981.

[175] R. F. Webbink, "Double white dwarfs as progenitors of R Coronae Borealis stars and type I supernovae." , vol. 277, pp. 355–360, Feb. 1984.

[176] H. A. Bethe and G. E. Brown, "Evolution of binary compact objects that merge," The Astrophysical Journal, vol. 506, no. 2, p. 780, oct 1998. [Online]. Available: https://dx.doi.org/10.1086/306265

[177] K. Belczynski, V. Kalogera, and T. Bulik, "A comprehensive study of binary compact objects as gravitational wave sources: Evolutionary channels, rates, and physical properties," The Astrophysical Journal, vol. 572, no. 1, p. 407, jun 2002. [Online]. Available: https://dx.doi.org/10.1086/340304

[178] J. R. Hurley, C. A. Tout, and O. R. Pols, "Evolution of binary stars and the effect of tides on binary populations," Monthly Notices of the Royal Astronomical Society, vol. 329, no. 4, pp. 897–928, 02 2002. [Online]. Available: https://doi.org/10.1046/j.1365-8711.2002.05038.x

[179] S. E. de Mink, M. Cantiello et al., "Rotational mixing in close binaries," Proceedings of the International Astronomical Union, vol. 4, no. S252, p. 365–370, 2008.

[180] I. Mandel and S. E. de Mink, "Merging binary black holes formed through chemically homogeneous evolution in short-period stellar binaries," Monthly Notices of the Royal Astronomical Society, vol. 458, no. 3, pp. 2634–2647, 02 2016. [Online]. Available: https://doi.org/10.1093/mnras/stw379

[181] P. Marchant, N. Langer et al., "A new route towards merging massive black holes," Astronomy &amp Astrophysics, vol. 588, p. A50, mar 2016. [Online]. Available: https://doi.org/10.1051%2F0004-6361%2F201628133

[182] S. Stevenson, A. Vigna-Gómez et al., "Formation of the first three gravitational-wave observations through isolated binary evolution," Nature Communications, vol. 8, no. 1, apr 2017. [Online]. Available: https://doi.org/10.1038%2Fncomms14906

[183] N. Giacobbo and M. Mapelli, "The progenitors of compact-object binaries: impact of metallicity, common envelope and natal kicks," Monthly Notices of the Royal Astronomical Society, vol. 480, no. 2, pp. 2011–2030, 07 2018.
[Online]. Available: https://doi.org/10.1093/mnras/sty1999

[184] M. Zevin, S. S. Bavera et al., "One channel to rule them all? constraining the origins of binary black holes using multiple formation pathways," The Astrophysical Journal, vol. 910, no. 2, p. 152, apr 2021.
[Online]. Available: https://dx.doi.org/10.3847/1538-4357/abe40e

[185] J. Kumamoto, M. S. Fujii, and A. Tanikawa, "Gravitational-wave emission from binary black holes formed in open clusters," Monthly Notices of the Royal Astronomical Society, vol. 486, no. 3, pp. 3942–3950, 04 2019.
[Online]. Available: https://doi.org/10.1093/mnras/stz1068

[186] U. N. Di Carlo, M. Mapelli et al., "Binary black holes in young star clusters: the impact of metallicity," Monthly Notices of the Royal Astronomical Society, vol. 498, no. 1, pp. 495–506, 08 2020.
[Online]. Available: https://doi.org/10.1093/mnras/staa2286

[187] A. A. Trani, A. Tanikawa et al., "Spin misalignment of black hole binaries from young star clusters: implications for the origin of gravitational waves events," Monthly Notices of the Royal Astronomical Society, vol. 504, no. 1, pp. 910–919, 04 2021.
[Online]. Available: https://doi.org/10.1093/mnras/stab967

[188] M. A. Sedda, M. Mapelli et al., "Population synthesis of black hole mergers with b-pop: the impact of dynamics, natal spins, and intermediate-mass black holes on the population of gravitational wave sources," 2021.
[Online]. Available: https://arxiv.org/abs/2109.12119

[189] I. Mandel and S. E. de Mink, "Merging binary black holes formed through chemically

homogeneous evolution in short-period stellar binaries," <u>Monthly Notices of the Royal Astronomical Society</u>, vol. 458, no. 3, pp. 2634–2647, 02 2016.
[Online]. Available: https://doi.org/10.1093/mnras/stw379

[190] S. E. de Mink and I. Mandel, "The chemically homogeneous evolutionary channel for binary black hole mergers: rates and properties of gravitational-wave events detectable by advanced LIGO," <u>Monthly Notices of the Royal Astronomical Society</u>, vol. 460, no. 4, pp. 3545–3553, 05 2016.
[Online]. Available: https://doi.org/10.1093/mnras/stw1219

[191] P. Marchant, N. Langer <u>et al.</u>, "A new route towards merging massive black holes," , vol. 588, p. A50, Apr. 2016.

[192] N. Ivanova, S. Justham <u>et al.</u>, "Common envelope evolution: where we stand and how we can move forward," <u>The Astronomy and Astrophysics Review</u>, vol. 21, no. 1, Feb 2013.
[Online]. Available: http://dx.doi.org/10.1007/s00159-013-0059-2

[193] N. Ivanova and S. Chaichenets, "Common envelope: Enthalpy consideration," <u>The Astrophysical Journal</u>, vol. 731, no. 2, p. L36, Mar 2011.
[Online]. Available: http://dx.doi.org/10.1088/2041-8205/731/2/L36

[194] J. D. M. Dewi and T. M. Tauris, "On the energy equation and efficiency parameter of the common envelope evolution," , vol. 360, pp. 1043–1051, Aug. 2000.

[195] X.-J. Xu and X.-D. Li, "On the binding energy parameter of common envelope evolution," <u>The Astrophysical Journal</u>, vol. 716, no. 1, p. 114–121, May 2010.
[Online]. Available: http://dx.doi.org/10.1088/0004-637X/716/1/114

[196] C. Wang, K. Jia, and X.-D. Li, "The binding energy parameter for common envelope evolution," <u>Research in Astronomy and Astrophysics</u>, vol. 16, no. 8, p. 009, Aug 2016.
[Online]. Available: http://dx.doi.org/10.1088/1674-4527/16/8/126

[197] J. Klencki, G. Nelemans et al., "It has to be cool: Supergiant progenitors of binary black hole mergers from common-envelope evolution," Astronomy Astrophysics, vol. 645, p. A54, Jan 2021.
[Online]. Available: http://dx.doi.org/10.1051/0004-6361/202038707

[198] M. U. Kruckow, T. M. Tauris et al., "Common-envelope ejection in massive binary stars," Astronomy Astrophysics, vol. 596, p. A58, Nov 2016.
[Online]. Available: http://dx.doi.org/10.1051/0004-6361/201629420

[199] ——, "Progenitors of gravitational wave mergers: binary evolution with the stellar grid-based code combine," Monthly Notices of the Royal Astronomical Society, vol. 481, no. 2, p. 1908–1949, Aug 2018.
[Online]. Available: http://dx.doi.org/10.1093/mnras/sty2190

[200] M. Dominik, K. Belczynski et al., "Double Compact Objects. I. The Significance of the Common Envelope on Merger Rates," , vol. 759, no. 1, p. 52, Nov. 2012.

[201] N. Mennekens and D. Vanbeveren, "Massive double compact object mergers: gravitational wave sources and r-process element production sites," , vol. 564, p. A134, Apr. 2014.

[202] K. Belczynski, D. E. Holz et al., "The first gravitational-wave source from the isolated evolution of two stars in the 40-100 solar mass range," , vol. 534, no. 7608, pp. 512–515, Jun. 2016.

[203] J. J. Eldridge and E. R. Stanway, "BPASS predictions for binary black hole mergers," , vol. 462, no. 3, pp. 3302–3313, Nov. 2016.

[204] J. Klencki, M. Moe et al., "Impact of inter-correlated initial binary parameters on double black hole and neutron star mergers," , vol. 619, p. A77, Nov. 2018.

[205] M. Mapelli and N. Giacobbo, "The cosmic merger rate of neutron stars and black holes," , vol. 479, no. 4, pp. 4391–4398, Oct. 2018.

[206] M. U. Kruckow, T. M. Tauris et al., "Progenitors of gravitational wave mergers: binary evolution with the stellar grid-based code COMBINE," , vol. 481, no. 2, pp. 1908–1949, Dec. 2018.

[207] K. Breivik, S. Coughlin et al., "COSMIC variance in binary population synthesis," The Astrophysical Journal, vol. 898, no. 1, p. 71, jul 2020. [Online]. Available: https://doi.org/10.3847/1538-4357/ab9d85

[208] B. Paczynski, "Evolution of Cataclysmic Binaries," in Cataclysmic Variables and Low-Mass X-ray Binaries, D. Q. Lamb and J. Patterson, Eds., Jan. 1985, p. 1.

[209] P. P. Eggleton, "From Wide to Close Binaries ?" in The Evolution of Galactic X-Ray Binaries, ser. NATO Advanced Study Institute (ASI) Series C, J. Truemper, W. H. G. Lewin, and W. Brinkmann, Eds., vol. 167, Jan. 1986, p. 87.

[210] F. Meyer and E. Meyer-Hofmeister, "Formation of cataclysmic binaries through common envelope evolution." , vol. 78, pp. 167–176, Sep. 1979.

[211] C. D. Bailyn and J. E. Grindlay, "On the Evolution of Tidal Capture X-Ray Binaries: 4U 2127+12 (M15) to 4U 1820-30 (NGC 6624)," , vol. 316, p. L25, May 1987.

[212] P. P. Eggleton and F. Verbunt, "Triple star evolution and the formation of short-period, low-mass X-ray binaries." , vol. 220, pp. 13P–18, May 1986.

[213] E. P. J. van den Heuvel, "The binary pulsar PSRJ2145-0750: a system originating from a low or intermediate mass X-ray binary with a donor star on the asymptotic giant branch?" , vol. 291, pp. L39–L42, Nov. 1994.

[214] T. Tauris and E. Van Den Heuvel, "Formation and evolution of compact stellar x-ray sources," Compact stellar X-ray sources, vol. 39, pp. 623–665, 2006.

[215] J. Iben, I. and A. V. Tutukov, "Supernovae of type I as end products of the evolution of binaries with components of moderate initial mass." , vol. 54, pp. 335–372, Feb. 1984.

[216] J. Iben, Icko and R. F. Webbink, "On the formation and properties of close binary white dwarfs," in IAU Colloq. 95: Second Conference on Faint Blue Stars, A. G. D. Philip, D. S. Hayes, and J. W. Liebert, Eds., Jan. 1987, pp. 401–412.

[217] R. F. Webbink and J. Iben, Icko, "Tidal interaction and coalescence of close binary white dwarfs." in IAU Colloq. 95: Second Conference on Faint Blue Stars, A. G. D. Philip, D. S. Hayes, and J. W. Liebert, Eds., Jan. 1987, pp. 445–456.

[218] Z. Han, "The formation of double degenerates and related objects," , vol. 296, no. 4, pp. 1019–1040, Jun. 1998.

[219] G. Nelemans, F. Verbunt et al., "Reconstructing the evolution of double helium white dwarfs: envelope loss without spiral-in," , vol. 360, pp. 1011–1018, Aug. 2000.

[220] G. Nelemans, L. R. Yungelson et al., "Population synthesis for double white dwarfs . I. Close detached systems," , vol. 365, pp. 491–507, Jan. 2001.

[221] M. Chruslinska, K. Belczynski et al., "Double neutron stars: merger rates revisited," , vol. 474, no. 3, pp. 2937–2958, Mar. 2018.

[222] A. Vigna-Gómez, S. L. Schrøder et al., "Fallback supernova assembly of heavy binary neutron stars and light black hole–neutron star pairs and the common stellar ancestry of GW190425 and GW200115," The Astrophysical Journal Letters, vol. 920, no. 1, p. L17, oct 2021.
[Online]. Available: https://doi.org/10.3847/2041-8213/ac2903

[223] A. Vigna-Gómez, C. J. Neijssel et al., "On the formation history of Galactic double

neutron stars," <u>Monthly Notices of the Royal Astronomical Society</u>, vol. 481, no. 3, pp. 4009–4029, 09 2018.

[Online]. Available: https://doi.org/10.1093/mnras/sty2463

[224] A. Vigna-Gó mez, M. Wassink <u>et al.</u>, "Stellar response after stripping as a model for common-envelope outcomes," <u>Monthly Notices of the Royal Astronomical Society</u>, vol. 511, no. 2, pp. 2326–2338, jan 2022.

[Online]. Available: https://doi.org/10.1093%2Fmnras%2Fstac237

[225] Roche, "La figure d'une masse fluide soumise à l'attraction d'un point éloigné, part 1," <u>Académie des sciences de Montpellier: Mémoires de la section des sciences</u>, 1849.

[226] ——, "La figure d'une masse fluide soumise à l'attraction d'un point éloigné, part 2," <u>Académie des sciences de Montpellier: Mémoires de la section des sciences</u>, 1850.

[227] ——, "La figure d'une masse fluide soumise à l'attraction d'un point éloigné, part 3," <u>Académie des sciences de Montpellier: Mémoires de la section des sciences</u>, 1851.

[228] ——, "Recherches sur les atmosph'eres des com'ete," <u>Annales de l'Observatoire imperial de Paris</u>, 1859.

[229] T. M. Tauris and E. v. d. Heuvel, "Formation and evolution of compact stellar x-ray sources," 2003.

[Online]. Available: https://arxiv.org/abs/astro-ph/0303456

[230] Z. Kopal, <u>Dynamics of close binary systems</u>. Springer Science & Business Media, 2012, vol. 68.

[231] M. Plavec and P. Kratochvil, "Tables for the Roche model of close binaries," <u>Bulletin of the Astronomical Institutes of Czechoslovakia</u>, vol. 15, p. 165, Jan. 1964.

[232] B. Paczyński, "Evolutionary Processes in Close Binary Systems," , vol. 9, p. 183, Jan. 1971.

[233] P. P. Eggleton, "Aproximations to the radii of Roche lobes." , vol. 268, pp. 368–369, May 1983.

[234] G. E. Soberman, E. S. Phinney, and E. P. J. v. d. Heuvel, "Stability criteria for mass transfer in binary stellar evolution," 1997.
[Online]. Available: https://arxiv.org/abs/astro-ph/9703016

[235] R. F. Webbink, "Stellar evolution and binaries," in Interacting Binary Stars, J. E. Pringle and R. A. Wade, Eds., 1985, p. 39.

[236] G. E. Soberman, E. S. Phinney, and E. P. J. v. d. Heuvel, "Stability criteria for mass transfer in binary stellar evolution," 1997.
[Online]. Available: https://arxiv.org/abs/astro-ph/9703016

[237] S. Negu and S. Tessema, "Mass transfer in binary stellar evolution and its stability," International Journal of Astronomy and Astrophysics, vol. 05, pp. 222–241, 01 2015.

[238] S. N. Shore, Observations and Physical Processes in Binary Stars.   Berlin, Heidelberg: Springer Berlin Heidelberg, 1994, pp. 1–133.
[Online]. Available: https://doi.org/10.1007/3-540-31626-4_1

[239] G. E. Soberman, E. S. Phinney, and E. P. J. van den Heuvel, "Stability criteria for mass transfer in binary stellar evolution." , vol. 327, pp. 620–635, Nov. 1997.

[240] K. Pavlovskii, N. Ivanova et al., "Stability of mass transfer from massive giants: double black hole binary formation and ultraluminous X-ray sources," Monthly Notices of the Royal Astronomical Society, vol. 465, no. 2, pp. 2092–2100, 10 2016.
[Online]. Available: https://doi.org/10.1093/mnras/stw2786

[241] M. S. Hjellming and R. F. Webbink, "Thresholds for Rapid Mass Transfer in Binary System. I. Polytropic Models," , vol. 318, p. 794, Jul. 1987.

[242] T. E. Woods and N. Ivanova, "Can We Trust Models for Adiabatic Mass Loss?" , vol. 739, no. 2, p. L48, Oct. 2011.

[243] N. Ivanova and R. E. Taam, "Thermal timescale mass transfer and the evolution of white dwarf binaries," The Astrophysical Journal, vol. 601, no. 2, pp. 1058–1066, feb 2004.
[Online]. Available: https://doi.org/10.1086/380561

[244] H. Ge, M. S. Hjellming et al., "Adiabatic Mass Loss in Binary Stars. I. Computational Method," , vol. 717, no. 2, pp. 724–738, Jul. 2010.

[245] K. Belczynski, V. Kalogera et al., "Compact object modeling with the startrack population synthesis code," The Astrophysical Journal Supplement Series, vol. 174, no. 1, p. 223, jan 2008.
[Online]. Available: https://dx.doi.org/10.1086/521026

[246] K. Pavlovskii and N. Ivanova, "Mass transfer from giant donors," , vol. 449, no. 4, pp. 4415–4427, Jun. 2015.

[247] G. H. Darwin, "On the Bodily Tides of Viscous and Semi-Elastic Spheroids, and on the Ocean Tides upon a Yielding Nucleus," Philosophical Transactions of the Royal Society of London Series I, vol. 170, pp. 1–35, Jan. 1879.

[248] ——, "The Determination of the Secular Effects of Tidal Friction by a Graphical Method," Proceedings of the Royal Society of London Series I, vol. 29, pp. 168–181, Jan. 1879.

[249] I. Counselman, Charles C., "Outcomes of Tidal Evolution," , vol. 180, pp. 307–316, Feb. 1973.

[250] Z. Kopal, Dynamics of close binary systems, 1978.

127

[251] D. Lai, F. A. Rasio, and S. L. Shapiro, "Hydrodynamic Instability and Coalescence of Close Binary Systems," , vol. 406, p. L63, Apr. 1993.

[252] ——, "Equilibrium, Stability, and Orbital Evolution of Close Binary Systems," , vol. 423, p. 344, Mar. 1994.

[253] ——, "Hydrodynamic Instability and Coalescence of Binary Neutron Stars," , vol. 420, p. 811, Jan. 1994.

[254] P. Hut, "Stability of tidal equilibrium," , vol. 92, no. 1-2, pp. 167–170, Dec. 1980.

[255] M. Vick, M. MacLeod et al., "Tidal dissipation impact on the eccentric onset of common envelope phases in massive binary star systems," Monthly Notices of the Royal Astronomical Society, vol. 503, no. 4, pp. 5569–5582, 03 2021. [Online]. Available: https://doi.org/10.1093/mnras/stab850

[256] J. P. Zahn, "Tidal friction in close binary systems." , vol. 57, pp. 383–394, May 1977.

[257] J. Goodman and S. P. Oh, "Fast tides in slow stars: The efficiency of eddy viscosity," The Astrophysical Journal, vol. 486, no. 1, p. 403, sep 1997. [Online]. Available: https://dx.doi.org/10.1086/304505

[258] G. I. Ogilvie and D. N. C. Lin, "Tidal dissipation in rotating solar-type stars," The Astrophysical Journal, vol. 661, no. 2, p. 1180, jun 2007. [Online]. Available: https://dx.doi.org/10.1086/515435

[259] F. Verbunt and E. S. Phinney, "Tidal circularization and the eccentricity of binaries containing giant stars." , vol. 296, p. 709, Apr. 1995.

[260] J. Goodman and E. S. Dickson, "Dynamical tide in solar-type binaries," The Astrophysical Journal, vol. 507, no. 2, p. 938, nov 1998. [Online]. Available: https://dx.doi.org/10.1086/306348

[261] G. J. Savonije and M. G. Witte, "Tidal interaction of a rotating 1 vec {M_sun} star with a binary companion," , vol. 386, pp. 211–221, Apr. 2002.

[262] M. C. Begelman, "Can a spherically accreting black hole radiate very near the Eddington limit," Monthly Notices of the Royal Astronomical Society, vol. 187, no. 2, pp. 237–251, 06 1979.
[Online]. Available: https://doi.org/10.1093/mnras/187.2.237

[263] J. C. Houck and R. A. Chevalier, "Steady Spherical Hypercritical Accretion onto Neutron Stars," , vol. 376, p. 234, Jul. 1991.

[264] A. R. King and M. C. Begelman, "Radiatively driven outflows and avoidance of common-envelope evolution in close binaries," The Astrophysical Journal, vol. 519, no. 2, p. L169, jun 1999.
[Online]. Available: https://dx.doi.org/10.1086/312126

[265] P. M. Ricker and R. E. Taam, "AN AMR STUDY OF THE COMMON-ENVELOPE PHASE OF BINARY EVOLUTION," The Astrophysical Journal, vol. 746, no. 1, p. 74, jan 2012.
[Online]. Available: https://doi.org/10.1088%2F0004-637x%2F746%2F1%2F74

[266] J.-C. Passy, F. Herwig, and B. Paxton, "The Response of Giant Stars to Dynamical-timescale Mass Loss," , vol. 760, no. 1, p. 90, Nov. 2012.

[267] J. L. A. Nandez and N. Ivanova, "Common envelope events with low-mass giants: understanding the energy budget," , vol. 460, no. 4, pp. 3992–4002, Aug. 2016.

[268] M. MacLeod, A. Antoni et al., "Common Envelope Wind Tunnel: Coefficients of Drag and Accretion in a Simplified Context for Studying Flows around Objects Embedded within Stellar Envelopes," , vol. 838, no. 1, p. 56, Mar. 2017.

[269] T. Fragos, J. J. Andrews et al., "The Complete Evolution of a Neutron-star Binary through a Common Envelope Phase Using 1D Hydrodynamic Simulations," , vol. 883, no. 2, p. L45, Oct. 2019.

[270] A. Frank, B. Balick et al., "Astrophysical Gasdynamics Confronts Reality: The Shaping of Planetary Nebuale," , vol. 404, p. L25, Feb. 1993.

[271] G. Mellema and A. Frank, "Numerical models and our understanding of aspherical planetary nebulae," 1994.
[Online]. Available: https://arxiv.org/abs/astro-ph/9410057

[272] N. Soker and M. Livio, "Disks and jets in planetary nebulae," , vol. 421, p. 219, Jan. 1994.

[273] A. Frank, Z. Chen et al., "Planetary Nebulae Shaped by Common Envelope Evolution," Galaxies, vol. 6, no. 4, p. 113, Oct. 2018.

[274] Y. Zou, A. Frank et al., "Bipolar planetary nebulae from outflow collimation by common envelope evolution," Monthly Notices of the Royal Astronomical Society, vol. 497, no. 3, pp. 2855–2869, jul 2020.
[Online]. Available: https://doi.org/10.1093%2Fmnras%2Fstaa2145

[275] F. A. Rasio and M. Livio, "On the formation and evolution of common envelope systems," The Astrophysical Journal, vol. 471, no. 1, pp. 366–367, nov 1996.
[Online]. Available: https://doi.org/10.1086/177975

[276] M. Livio and N. Soker, "The Common Envelope Phase in the Evolution of Binary Stars," , vol. 329, p. 764, Jun. 1988.

[277] E. L. Sandquist, R. E. Taam et al., "Double Core Evolution. X. Through the Envelope Ejection Phase," , vol. 500, no. 2, pp. 909–922, jun 1998.

[278] J.-C. Passy, O. D. Marco et al., "SIMULATING THE COMMON ENVELOPE PHASE OF a RED GIANT USING SMOOTHED-PARTICLE HYDRODYNAMICS AND UNIFORM-GRID CODES," The Astrophysical Journal, vol. 744, no. 1, p. 52, dec 2011.
[Online]. Available: https://doi.org/10.1088%2F0004-637x%2F744%2F1%2F52

[279] N. Ivanova and J. L. A. Nandez, "Common envelope events with low-mass giants: understanding the transition to the slow spiral-in," Monthly Notices of the Royal Astronomical Society, vol. 462, no. 1, pp. 362–381, jul 2016.
[Online]. Available: https://doi.org/10.1093%2Fmnras%2Fstw1676

[280] S. T. Ohlmann, F. K. Röpke et al., "Constructing stable 3d hydrodynamical models of giant stars," Astronomy &amp Astrophysics, vol. 599, p. A5, feb 2017.
[Online]. Available: https://doi.org/10.1051%2F0004-6361%2F201629692

[281] R. Iaconi, O. De Marco et al., "The effect of binding energy and resolution in simulations of the common envelope binary interaction," Monthly Notices of the Royal Astronomical Society, vol. 477, no. 2, pp. 2349–2365, 03 2018.
[Online]. Available: https://doi.org/10.1093/mnras/sty794

[282] J. L. A. Nandez and N. Ivanova, "Common envelope events with low-mass giants: understanding the energy budget," Monthly Notices of the Royal Astronomical Society, vol. 460, no. 4, pp. 3992–4002, 05 2016.
[Online]. Available: https://doi.org/10.1093/mnras/stw1266

[283] M. de Kool, "Common Envelope Evolution and Double Cores of Planetary Nebulae," , vol. 358, p. 189, Jul. 1990.

[284] P. F. L. Maxted, R. Napiwotzki et al., "Survival of a brown dwarf after engulfment by a red giant star," Nature, vol. 442, no. 7102, pp. 543–545, aug 2006.
[Online]. Available: https://doi.org/10.1038%2Fnature04987

[285] M. Afşar and C. İbanoğlu, "Two-colour photometry of the binary planetary nebula nuclei UU Sagitte and V477 Lyrae: oversized secondaries in post-common-envelope binaries," , vol. 391, no. 2, pp. 802–814, Dec. 2008.

[286] M. Zorotovic, M. R. Schreiber et al., "Post-common-envelope binaries from SDSS. IX: Constraining the common-envelope efficiency," , vol. 520, p. A86, Sep. 2010.

[287] E. L. Sandquist, R. E. Taam et al., "Double core evolution. x. through the envelope ejection phase," The Astrophysical Journal, vol. 500, no. 2, p. 909, jun 1998. [Online]. Available: https://dx.doi.org/10.1086/305778

[288] S. C. Yoon, S. E. Woosley, and N. Langer, "Type Ib/c Supernovae in Binary Systems. I. Evolution and Properties of the Progenitor Stars," , vol. 725, no. 1, pp. 940–954, Dec. 2010.

[289] P. Agrawal, J. Hurley et al., "The fates of massive stars: exploring uncertainties in stellar evolution with metisse," Monthly Notices of the Royal Astronomical Society, vol. 497, no. 4, pp. 4549–4564, aug 2020. [Online]. Available: https://doi.org/10.1093%2Fmnras%2Fstaa2264

[290] L. Grassitelli, N. Langer et al., "Subsonic structure and optically thick winds from Wolf-Rayet stars," , vol. 614, p. A86, Jun. 2018.

[291] L. Grassitelli, N. Langer et al., "Wind-envelope interaction as the origin of the slow cyclic brightness variations of luminous blue variables," Astronomy &amp Astrophysics, vol. 647, p. A99, mar 2021. [Online]. Available: https://doi.org/10.1051%2F0004-6361%2F202038298

[292] B. Paxton, L. Bildsten et al., "MODULES FOR EXPERIMENTS IN STELLAR ASTROPHYSICS (MESA)," The Astrophysical Journal Supplement Series, vol. 192, no. 1, p. 3, dec 2010. [Online]. Available: https://doi.org/10.1088%2F0067-0049%2F192%2F1%2F3

[293] A. S. Jermyn, E. B. Bauer et al., "Modules for experiments in stellar astrophysics (mesa): Time-dependent convection, energy conservation, automatic differentiation, and infrastructure," 2022.

[Online]. Available: https://arxiv.org/abs/2208.03651

[294] K. Yakut and P. P. Eggleton, "Evolution of close binary systems," The Astrophysical Journal, vol. 629, no. 2, p. 1055, aug 2005.

[Online]. Available: https://dx.doi.org/10.1086/431300

[295] J. J. Eldridge, R. G. Izzard, and C. A. Tout, "The effect of massive binaries on stellar populations and supernova progenitors," Monthly Notices of the Royal Astronomical Society, vol. 384, no. 3, pp. 1109–1118, 07 2008.

[Online]. Available: https://doi.org/10.1111/j.1365-2966.2007.12738.x

[296] J. S. W. Claeys, O. R. Pols et al., "Theoretical uncertainties of the type ia supernova rate," Astronomy Astrophysics, vol. 563, p. A83, Mar 2014.

[Online]. Available: http://dx.doi.org/10.1051/0004-6361/201322714

[297] N. Giacobbo, M. Mapelli, and M. Spera, "Merging black hole binaries: The effects of progenitor's metallicity, mass-loss rate and eddington factor," Monthly Notices of the Royal Astronomical Society, vol. 474, 11 2017.

[298] P. Podsiadlowski, "Common-Envelope Evolution and Stellar Mergers," in Evolution of Binary and Multiple Star Systems, ser. Astronomical Society of the Pacific Conference Series, P. Podsiadlowski, S. Rappaport et al., Eds., vol. 229, Jan. 2001, p. 239.

[299] Y. Chen, A. Bressan et al., "New evolutionary tracks of massive stars with PARSEC," in IAU General Assembly, vol. 29, Aug. 2015, p. 2257534.

[300] J. R. Hurley, O. R. Pols, and C. A. Tout, "Comprehensive analytic formulae for stellar evolution as a function of mass and metallicity," Monthly Notices of the Royal Astronomical Society, vol. 315, no. 3, pp. 543–569, jul 2000.

[Online]. Available: https://doi.org/10.1046%2Fj.1365-8711.2000.03426.x

[301] J. R. Hurley, C. A. Tout, and O. R. Pols, "Evolution of binary stars and the effect of tides on binary populations," Monthly Notices of the Royal Astronomical Society, vol. 329, no. 4, pp. 897–928, feb 2002.
[Online]. Available: https://doi.org/10.1046%2Fj.1365-8711.2002.05038.x

[302] N. Giacobbo, M. Mapelli, and M. Spera, "Merging black hole binaries: the effects of progenitor's metallicity, mass-loss rate and Eddington factor," Monthly Notices of the Royal Astronomical Society, vol. 474, no. 3, pp. 2959–2974, 11 2017.
[Online]. Available: https://doi.org/10.1093/mnras/stx2933

[303] J. R. Hurley, O. R. Pols, and C. A. Tout, "Comprehensive analytic formulae for stellar evolution as a function of mass and metallicity," , vol. 315, no. 3, pp. 543–569, Jul. 2000.

[304] J. S. Vink, A. de Koter, and H. J. G. L. M. Lamers, "Mass-loss predictions for O and B stars as a function of metallicity," , vol. 369, pp. 574–588, Apr. 2001.

[305] X.-J. Xu and X.-D. Li, "Erratum: "on the binding energy parameter of common envelope evolution" (2010, apj, 716, 114)," The Astrophysical Journal, vol. 722, no. 2, p. 1985, oct 2010.
[Online]. Available: https://dx.doi.org/10.1088/0004-637X/722/2/1985

[306] X.-J. Xu and X.-D. Li, "On the Binding Energy Parameter λ of Common Envelope Evolution," , vol. 716, no. 1, pp. 114–121, Jun. 2010.

[307] M. Mapelli, N. Giacobbo et al., "The cosmic merger rate of stellar black hole binaries from the Illustris simulation," , vol. 472, no. 2, pp. 2422–2435, Dec. 2017.

[308] N. Giacobbo and M. Mapelli, "Revising Natal Kick Prescriptions in Population Synthesis Simulations," , vol. 891, no. 2, p. 141, Mar. 2020.

134

[309] ——, "The impact of electron-capture supernovae on merging double neutron stars," , vol. 482, no. 2, pp. 2234–2243, Jan. 2019.

[310] ——, "The progenitors of compact-object binaries: impact of metallicity, common envelope and natal kicks," , vol. 480, no. 2, pp. 2011–2030, Oct. 2018.

[311] N. Giacobbo, M. Mapelli, and M. Spera, "Merging black hole binaries: the effects of progenitor's metallicity, mass-loss rate and Eddington factor," , vol. 474, no. 3, pp. 2959–2974, Mar. 2018.

[312] P. P. Eggleton, "The evolution of low mass stars," , vol. 151, p. 351, Jan. 1971.

[313] O. R. Pols, C. A. Tout et al., "Approximate input physics for stellar modelling," , vol. 274, no. 3, pp. 964–974, Jun. 1995.

[314] T. M. Tauris and J. D. M. Dewi, "Research Note On the binding energy parameter of common envelope evolution. Dependency on the definition of the stellar core boundary during spiral-in," , vol. 369, pp. 170–173, Apr. 2001.

[315] T. M. Tauris, "Aspects of mass transfer in X-ray binaries: a model for three classes of binary millisecond pulsars." , vol. 315, pp. 453–462, Nov. 1996.

[316] B. B., "M.Sc. Thesis," Univ. Amsterdam, 1998.

[317] J. R. Hurley, O. R. Pols, and C. A. Tout, "Comprehensive analytic formulae for stellar evolution as a function of mass and metallicity," Monthly Notices of the Royal Astronomical Society, vol. 315, no. 3, pp. 543–569, 07 2000. [Online]. Available: https://doi.org/10.1046/j.1365-8711.2000.03426.x

[318] S. F. Portegies Zwart and F. Verbunt, "Population synthesis of high-mass binaries." , vol. 309, pp. 179–196, May 1996.

[319] E. De Donder and D. Vanbeveren, "The influence of neutron star mergers on the galactic chemical enrichment of r-process elements," New Astronomy, vol. 9, no. 1, pp. 1–16, 2004.

[Online]. Available: https://www.sciencedirect.com/science/article/pii/ S1384107603000708

[320] R. G. Izzard, C. A. Tout et al., "A new synthetic model for asymptotic giant branch stars," Monthly Notices of the Royal Astronomical Society, vol. 350, no. 2, pp. 407–426, 05 2004.

[Online]. Available: https://doi.org/10.1111/j.1365-2966.2004.07446.x

[321] J. W. Barrett, I. Mandel et al., "Exploring the parameter space of compact binary population synthesis," Proceedings of the International Astronomical Union, vol. 12, no. S325, p. 46–50, 2016.

[322] K. Breivik, S. Coughlin et al., "COSMIC Variance in Binary Population Synthesis," , vol. 898, no. 1, p. 71, Jul. 2020.

[323] J. R. Hurley, C. A. Tout, and O. R. Pols, "Evolution of binary stars and the effect of tides on binary populations," , vol. 329, no. 4, pp. 897–928, Feb. 2002.

[324] R. Voss and T. M. Tauris, "Galactic distribution of merging neutron stars and black holes – prospects for short gamma-ray burst progenitors and LIGO/VIRGO," Monthly Notices of the Royal Astronomical Society, vol. 342, no. 4, pp. 1169–1184, 07 2003.

[Online]. Available: https://doi.org/10.1046/j.1365-8711.2003.06616.x

[325] M. U. Kruckow, T. M. Tauris et al., "Progenitors of gravitational wave mergers: binary evolution with the stellar grid-based code ComBinE," Monthly Notices of the Royal Astronomical Society, vol. 481, no. 2, pp. 1908–1949, 08 2018.

[Online]. Available: https://doi.org/10.1093/mnras/sty2190

[326] L. Nelson, "New Population Synthesis Techniques in the Analysis of Interacting Binaries," in Journal of Physics Conference Series, ser. Journal of Physics Conference Series, vol. 341, Feb. 2012, p. 012008.

[327] H.-L. Chen, T. E. Woods et al., "Next generation population synthesis of accreting white dwarfs - I. Hybrid calculations using BSE+MESA," , vol. 445, no. 2, pp. 1912–1923, Dec. 2014.

[328] Y. Shao, X.-D. Li, and Z.-G. Dai, "A Population of Neutron Star Ultraluminous X-Ray Sources with a Helium Star Companion," , vol. 886, no. 2, p. 118, Dec. 2019.

[329] Y. Shao and X.-D. Li, "Population Synthesis of Black Hole Binaries with Compact Star Companions," , vol. 920, no. 2, p. 81, Oct. 2021.

[330] S. S. Bavera, T. Fragos et al., "The impact of mass-transfer physics on the observable properties of field binary black hole populations," , vol. 647, p. A153, Mar. 2021.

[331] J. Román-Garza, S. S. Bavera et al., "The Role of Core-collapse Physics in the Observability of Black Hole Neutron Star Mergers as Multimessenger Sources," , vol. 912, no. 2, p. L23, May 2021.

[332] E. Zapartas, M. Renzo et al., "Revisiting the explodability of single massive star progenitors of stripped-envelope supernovae," , vol. 656, p. L19, Dec. 2021.

[333] T. Fragos, T. Linden et al., "On the formation of ultraluminous x-ray sources with neutron star accretors: The case of m82 x-2," The Astrophysical Journal Letters, vol. 802, no. 1, p. L5, mar 2015.
[Online]. Available: https://dx.doi.org/10.1088/2041-8205/802/1/L5

[334] Y. Shao and X.-D. Li, "A population of ultraluminous x-ray sources with an accreting neutron star," The Astrophysical Journal, vol. 802, no. 2, p. 131, apr 2015.
[Online]. Available: https://dx.doi.org/10.1088/0004-637X/802/2/131

[335] T. Fragos, J. J. Andrews et al., "Posydon: A general-purpose population synthesis code with detailed binary-evolution simulations," 2022.
[Online]. Available: https://arxiv.org/abs/2202.05892

[336] S. S. Bavera, T. Fragos et al., "The impact of mass-transfer physics on the observable properties of field binary black hole populations," Astronomy &amp Astrophysics, vol. 647, p. A153, mar 2021.
[Online]. Available: https://doi.org/10.1051%2F0004-6361%2F202039804

[337] A. Bressan, P. Marigo et al., "PARSEC: stellar tracks and isochrones with the PAdova and TRieste Stellar Evolution Code," Monthly Notices of the Royal Astronomical Society, vol. 427, no. 1, pp. 127–145, 11 2012.
[Online]. Available: https://doi.org/10.1111/j.1365-2966.2012.21948.x

[338] Y. Chen, A. Bressan et al., "parsec evolutionary tracks of massive stars up to 350 M at metallicities 0.0001 Z 0.04," Monthly Notices of the Royal Astronomical Society, vol. 452, no. 1, pp. 1068–1080, 07 2015.
[Online]. Available: https://doi.org/10.1093/mnras/stv1281

[339] M. Mencagli, N. Nazarova, and M. Spera, "ISTEDDAS: a new direct N-Body code to study merging compact-object binaries," in Journal of Physics Conference Series, ser. Journal of Physics Conference Series, vol. 2207, Mar. 2022, p. 012051.